

# THE SUBARU - XMM-NEWTON DEEP SURVEY (SXDS) VIII.: MULTI-WAVELENGTH IDENTIFICATION, OPTICAL/NIR SPECTROSCOPIC PROPERTIES, AND PHOTOMETRIC REDSHIFTS OF X-RAY SOURCES\*

Masayuki AKIYAMA,<sup>1</sup> Yoshihiro UEDA,<sup>2</sup> Mike G. WATSON,<sup>3</sup> Hisanori FURUSAWA,<sup>4</sup> Tadafumi TAKATA,<sup>4</sup> Chris SIMPSON,<sup>5</sup> Tomoki MOROKUMA,<sup>6</sup> Toru YAMADA,<sup>1</sup> Kouji OHTA,<sup>2</sup> Fumihide IWAMURO,<sup>2</sup> Kiyoto YABE,<sup>4</sup> Naoyuki TAMURA,<sup>7</sup> Yuuki MORITANI,<sup>8</sup> Naruhisa TAKATO,<sup>4</sup> Masahiko KIMURA,<sup>9</sup> Toshinori MAIHARA,<sup>2</sup> Gavin DALTON,<sup>10,11</sup> Ian LEWIS,<sup>10</sup> Hanshin LEE,<sup>10,12</sup> Emma CURTIS LAKE,<sup>10,13</sup> Edward MACAULAY,<sup>10,14</sup> Frazer CLARKE,<sup>10</sup> John D. SILVERMAN,<sup>7</sup> Scott CROOM,<sup>15</sup> Masami OUCHI,<sup>16</sup> Hitoshi HANAMI,<sup>17</sup> J.Diaz TELLO,<sup>18</sup> Tomohiro YOSHIKAWA,<sup>19</sup> Naofumi FUJISHIRO,<sup>20</sup> Kazuhiro SEKIGUCHI,<sup>4</sup>

<sup>1</sup>*Astronomical Institute, Tohoku University, Aramaki, Aoba-ku, Sendai, 980-8578, Japan*  
akiyama@astr.tohoku.ac.jp

<sup>2</sup>*Department of Astronomy, Kyoto University, Kitashirakawa-Oiwake-cho, Sakyo-ku, Kyoto, 606-8502, Japan*

<sup>3</sup>*XROA Group, Department of Physics and Astronomy, University of Leicester, Leicester LE1 7RH, UK*

<sup>4</sup>*National Astronomical Observatory of Japan, Mitaka, Tokyo 181-8588, Japan*

<sup>5</sup>*Astrophysics Research Institute, Liverpool John Moores University, ic2 Building, 146 Brownlow Hill, Liverpool L3 5RF, UK*

<sup>6</sup>*Institute of Astronomy, Graduate School of Science, University of Tokyo, 2-21-1, Osawa, Mitaka, Tokyo, 181-0015, Japan*

<sup>7</sup>*Kavli Institute for the Physics and Mathematics of the Universe, The University of Tokyo, Kashiwa, 277-8583, Japan*

<sup>8</sup>*Hiroshima Astrophysical Science Center, Hiroshima University, Higashi-Hiroshima, Hiroshima, 739-8526, Japan*

<sup>9</sup>*Institute of Astronomy and Astrophysics, Academia Sinica, No.1, Sec.4, Roosevelt Rd, Taipei, 10617, Taiwan, R.O.C.*

<sup>10</sup>*Department of Astrophysics, University of Oxford, Keble Road, Oxford, OX1 3RH, UK*

<sup>11</sup>*STFC Rutherford Appleton Laboratory, HSIC, Didcot, Oxfordshire OX11 0QX, UK*

<sup>12</sup>*McDonald Observatory, University of Texas at Austin, 1 University Station C1402, Austin, TX 78712, USA*

<sup>13</sup>*Institute for Astronomy, University of Edinburgh, Royal Observatory, Edinburgh EH9 3HJ, UK*

<sup>14</sup>*School of Mathematics and Physics, University of Queensland, Brisbane, QLD 4072, Australia*

<sup>15</sup>*Sydney Institute for Astronomy, School of Physics, University of Sydney, NSW 2006, Australia*

<sup>16</sup>*Institute for Cosmic Ray Research, University of Tokyo, Kashiwa, Chiba, 277-8582, Japan*

<sup>17</sup>*Physics Section, Faculty of Humanities and Social Sciences, Iwate University, 020-8550, Morioka, Japan*

<sup>18</sup>*IATE, Observatorio Astronomico de Cordoba, Universidad Nacional de Cordoba, Argentina*

<sup>19</sup>*Kyoto-Nijikoubou Co., Ltd., 17-203, Iwakura Minamiosagicho, Sakyo-ku, Kyoto-shi, Kyoto, 606-0003, Japan*

<sup>20</sup>*Koyama Astronomical Observatory, Kyoto Sangyo University, Motoyama, Kamigamo Kita-ku, Kyoto, 603-8047, Japan*

(Received ; accepted )

## Abstract

We report the multi-wavelength identification of the X-ray sources found in the Subaru – *XMM-Newton* Deep Survey (SXDS) using deep imaging data covering the wavelength range between the far-UV to the mid-IR. We select a primary counterpart of each X-ray source by applying the likelihood ratio method to *R*-band, 3.6 $\mu$ m, near-UV, and 24 $\mu$ m source catalogs as well as matching catalogs of AGN candidates selected in 1.4GHz radio and *i'*-band variability surveys. Once candidates of Galactic stars, ultra-luminous X-ray sources in a nearby galaxy, and clusters of galaxies are removed there are 896 AGN candidates in the sample. We conduct spectroscopic observations of the primary counterparts with multi-object spectrographs in the optical and NIR; 65% of the X-ray AGN candidates are spectroscopically-identified. For the remaining X-ray AGN candidates, we evaluate their photometric redshift with photometric data in 15 bands. Utilising the multi-wavelength photometric data of the large sample of X-ray selected AGNs, we evaluate the stellar masses,  $M_*$ , of the host galaxies of the narrow-line AGNs. The distribution of the stellar mass is remarkably constant from  $z = 0.1$  to 4.0. The relation between  $M_*$  and 2–10 keV luminosity can be explained with strong cosmological evolution of the relationship between the black hole mass and  $M_*$ . We also evaluate the scatter of the UV-MIR spectral energy distribution (SED) of the X-ray AGNs as a function of X-ray luminosity and absorption to the nucleus. The scatter is compared with galaxies which have redshift and stellar mass distribution matched with the X-ray AGN. The UV-NIR SEDs of obscured X-ray AGNs are similar to those of the galaxies in the matched sample. In the NIR-MIR range, the median SEDs of X-ray AGNs are redder, but the scatter of the SEDs of the X-ray AGN broadly overlaps that of the galaxies in the matched sample.

**Key words:** galaxies: active — X-rays: galaxies — catalogs — surveys — quasars: general

## 1. Introduction

After the discovery of super-massive black holes (SMBHs) at the center of every massive galaxy in the local Universe (e.g., Kormendy & Richstone 1995), the issue of how these SMBHs formed and evolved over cosmic history has become one of the major unanswered questions in observational cosmology. Luminosities of AGNs reflect the mass accretion rates of their SMBHs, therefore the luminosity function of AGNs and its cosmological evolution reflects the growth history of SMBHs through accretion. Hard X-ray selection is an effective selection method for AGNs, it can detect obscured AGNs without serious bias, except for Compton-thick AGNs, and can efficiently sample AGNs without contamination by a large number of star-forming galaxies. The hard X-ray luminosity function of AGNs and its evolution as a function of redshift have been examined with combining X-ray selected AGN samples with various survey depths and areas (Ueda et al. 2003; Barger et al. 2005; La Franca et al. 2005; Hasinger et al. 2005; Silverman et al. 2008; Aird et al. 2008; Yencho et al. 2009; Ebrero et al. 2009; Aird et al. 2010; Ueda et al. 2014). Based on the cosmological evolution of the hard X-ray luminosity function, the average accretion growth curves of SMBHs are inferred (Marconi et al. 2004; Ueda et al. 2014).

In order to construct a large sample of X-ray-selected AGNs, we have conducted deep multi-wavelength imaging observations covering the FUV to MIR and deep optical and NIR multi-object spectroscopic observations of the X-ray sources found in the Subaru *XMM-Newton* Deep Survey (SXDS) (Sekiguchi et al. 2005). The X-ray images obtained with *XMM-Newton* cover a  $1.3 \text{ deg}^2$  area down to  $1 \times 10^{-15} \text{ erg s}^{-1} \text{ cm}^{-2}$  in the 0.5–2 keV band and  $3 \times 10^{-15} \text{ erg s}^{-1} \text{ cm}^{-2}$  in the 2–10 keV band (Ueda et al. 2008). The  $\log N - \log S$  relation of the X-ray sources has a knee at a hard X-ray flux of  $1 \times 10^{-14} \text{ erg s}^{-1} \text{ cm}^{-2}$  and the contribution to the cosmic X-ray background is maximum in this flux range (Cowie et al. 2002). Several hard X-ray surveys covering  $\sim 1 \text{ deg}^2$  area in this flux range have been conducted (Fiore et al. 2003; Kim et al. 2004; Yang et al. 2004; Chiappetti et al. 2005; Murray et al. 2005; Laird et al. 2009; Elvis et al. 2009; Cappelluti et al. 2009; Civano et al. 2012). Among the X-ray surveys with similar depth and area, SXDS is notable in having deep multi-wavelength data in the wavelength range from far-UV to mid-IR.

In this paper, we describe the X-ray sample in Section 2, and the multi-wavelength imaging data in Section 3. The  $3 \sigma$  detection limits of the imaging data in the  $i'$ -,  $K$ -, and  $3.6 \mu\text{m}$  bands reach 27.4 mag, 25.3 mag, and 24.5 mag in the AB magnitude system, respectively. They are expected to be deep enough to detect counterparts of al-

most all of the X-ray sources at the flux limit: 90% of the X-ray sources found in a wide area *Chandra* survey at a flux limit of  $1 \times 10^{-15} \text{ erg s}^{-1} \text{ cm}^{-2}$  in the 0.5–2.0 keV band have a counterpart brighter than 26.4 mag ( $i'$ -band), 23.6 mag ( $K$ -band), and 22.8 mag ( $3.6 \mu\text{m}$ -band) (Civano et al. 2012). The positional uncertainties of the *XMM-Newton* X-ray sources are larger than those of *Chandra* sources, and they are not small enough to securely identify the faintest optical counterparts (Loaring et al. 2005; Chiappetti et al. 2005). In order to quantitatively select the counterparts, we apply the likelihood ratio method (de Ruiter 1977; Wolstencroft et al. 1986; Sutherland & Saunders 1992). We apply the method not only to the deep optical source catalog but also to the deep  $3.6 \mu\text{m}$ , NUV, and  $24 \mu\text{m}$  source catalogs to improve the reliability of the counterpart selection. The identification procedure with the multi-wavelength source catalogs is described in Section 4.

In order to reveal the nature of the X-ray sources, we have been conducting a large campaign of spectroscopic observations in the NIR as well as in the optical wavelength range. Because obscured AGNs at  $z = 1 - 2$  can be significant contributor to the X-ray source population, NIR spectroscopy is effective in revealing their nature by detecting strong rest-frame optical emission lines. The spectroscopic follow-up observations are described in Section 5. Even with the deep optical and NIR spectroscopic observations, a significant fraction of the X-ray sources are fainter than the spectroscopic limit. In order to overcome the limitation of the spectroscopic identification, photometric redshift estimation with a deep imaging data set covering wide wavelength range is important (Zheng et al. 2004). The multiwavelength photometry and photometric redshift evaluation are described in Section 6. In Section 7, we discuss the X-ray properties and host galaxy stellar mass of the X-ray selected AGNs. Utilising the multi-wavelength photometry, we examine the scatter of the SEDs of the X-ray AGNs, and compare the scatter with that of non-X-ray galaxies with similar redshifts and stellar masses. Throughout the paper, cosmological parameters  $H_0 = 70 \text{ km s}^{-1} \text{ Mpc}^{-1}$ ,  $\Omega_M = 0.3$ , and  $\Omega_\Lambda = 0.7$  are used. The magnitudes are based on AB magnitude system (Oke 1974).

Using the large sample of X-ray selected AGNs, Hiroi et al. (2012) derive the comoving space density and obscured fraction of AGNs at  $3 < z < 5$ . Furthermore, Ueda et al. (2014) examine the cosmological evolution of the X-ray AGN luminosity function including our sample. The black hole mass and Eddington ratio distribution functions of the X-ray selected AGNs at  $z \sim 1.4$  are discussed in Nobuta et al. (2012), using the optical and NIR spectra of the X-ray selected AGNs.

\* Based in part on data collected at Subaru Telescope, which is operated by the National Astronomical Observatory of Japan.

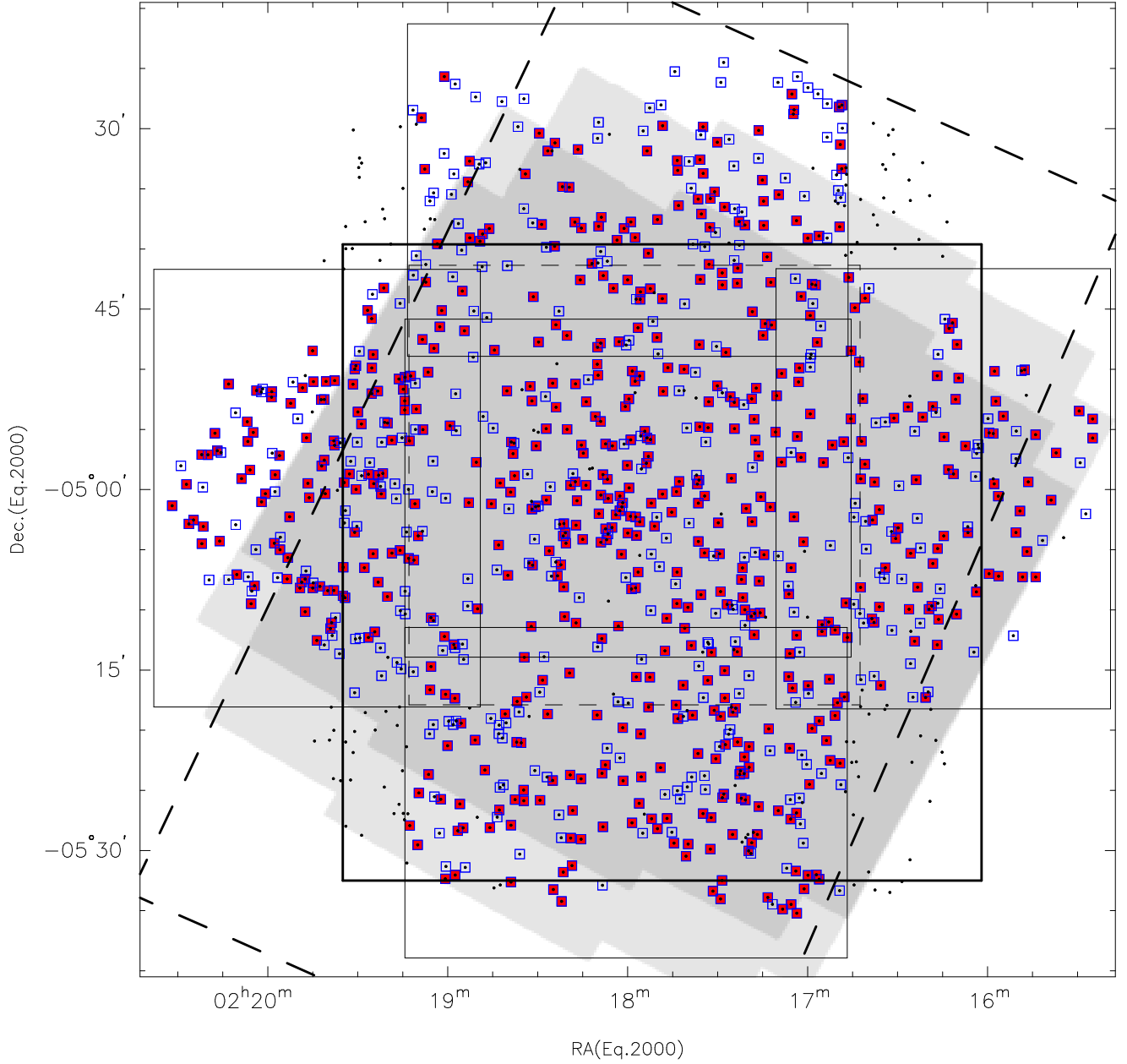


**Fig. 1.** The areas covered by  $u$ -band, optical, NIR, and MIR imaging observations are shown overlaid on a map of the detected X-ray sources from the 7 *XMM-Newton* images (Ueda et al. 2008). The 5 thin solid rectangles indicate the area covered by the deep Suprime-cam imaging observations. The thin dashed line shows the area covered by the deep  $u$ -band observations with the Mosaic-II camera. The thick solid square indicates the region covered by the deep  $J$ -,  $H$ -,  $K$ -band imaging observations of UKIDSS/UDS. The gray region indicates the region covered by SpUDS IRAC observations. The lower (upper) light gray region is only covered by  $3.6\mu\text{m}$  and  $5.8\mu\text{m}$  ( $4.5\mu\text{m}$  and  $8.0\mu\text{m}$ ) observations. The thick dashed line represents the region covered by the SpUDS MIPS observations. The black dots show positions of the X-ray sources with likelihood larger than 7 either in the soft or hard band from Ueda et al. (2008). The blue squares indicate X-ray sources included in the current sample which are covered by the Suprime-cam observations and not affected by halos of very bright stars. Red filled symbols indicate spectroscopically identified sources.

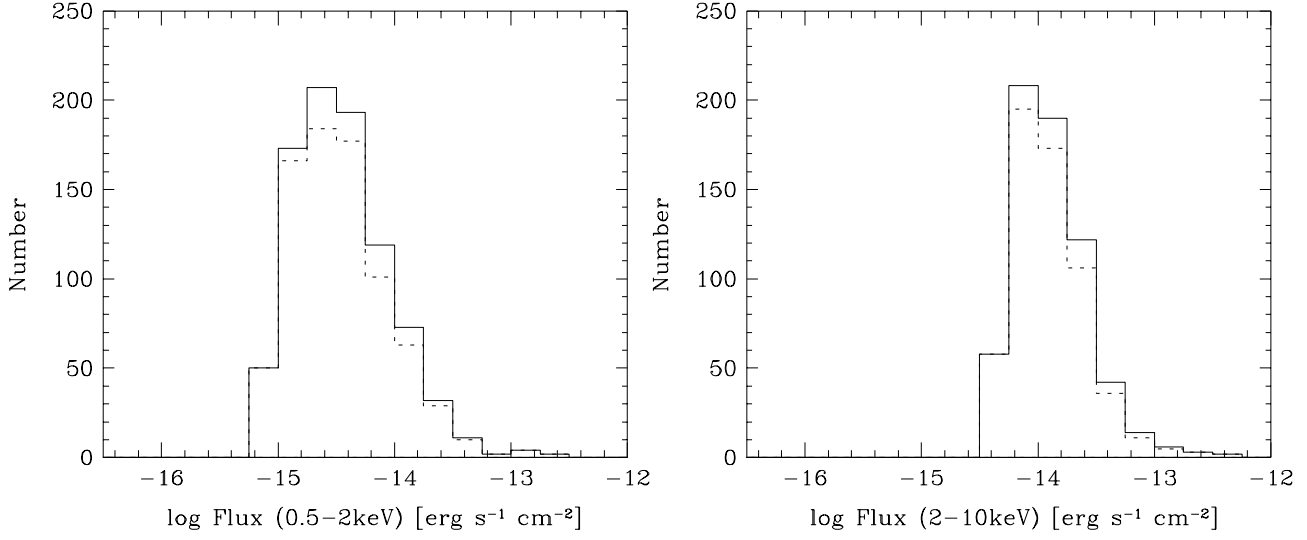


**Fig. 2.** Left) The 0.5–2.0 keV band flux distribution of the X-ray sources in the SXDS. The solid histogram represents the number density of the entire soft-band sample of Ueda et al. (2008), and the dotted histogram shows the number density of the sample considered in this paper. Right) The 2.0–10.0 keV band flux distribution with details as for left panel.

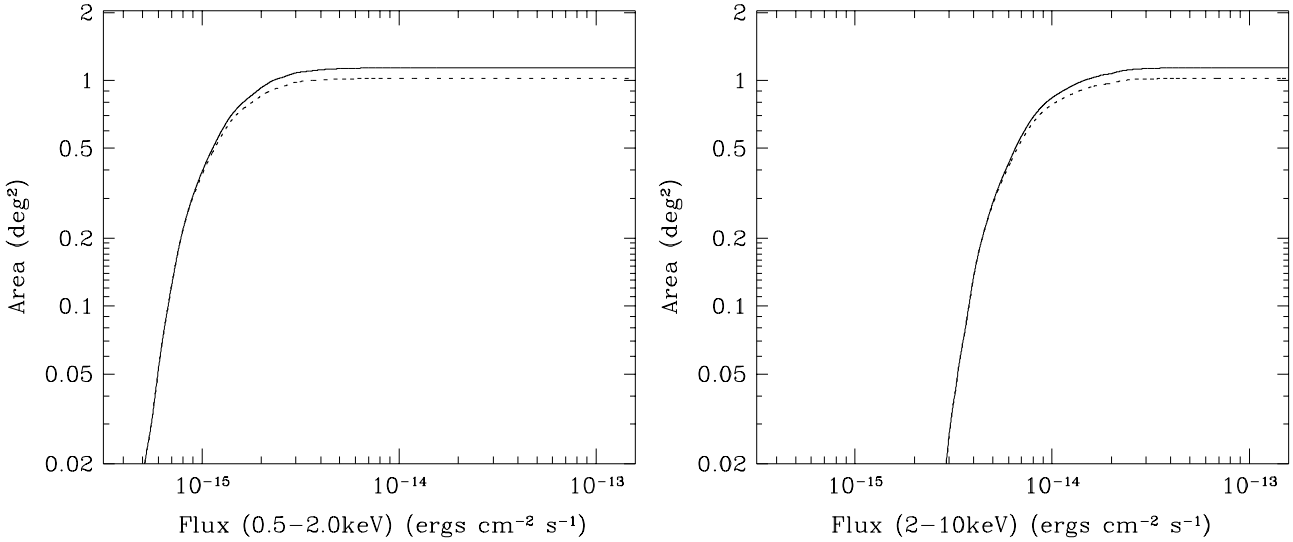


**Fig. 3.** Left) Survey area as a function of 0.5–2.0 keV X-ray flux for the soft-band sample. The solid line represents the survey area of the entire soft-band sample of Ueda et al. (2008), and the dotted line shows the survey area of the sample considered in this paper. The flux is determined by multiplying the soft-band countrate by  $0.167 \times 10^{-11}$  ( $\text{erg s}^{-1} \text{cm}^{-2}$ ) / ( $\text{cts ks}^{-1}$ ) assuming power-law spectrum with  $\Gamma=1.8$ . Right) Survey area for the hard-band sample. The flux is determined by multiplying the hard-band countrate by  $0.838 \times 10^{-11}$  ( $\text{erg s}^{-1} \text{cm}^{-2}$ ) / ( $\text{cts ks}^{-1}$ ) assuming the same power-law.

## 2. X-ray Sample Definition

The SXDS field is centered on  $02^{\text{h}}18^{\text{m}}$  and  $-05^{\circ}00'$ . The field is selected to be observable with 8-10m class optical telescopes in both of the northern and the southern hemispheres. The field was observed with *XMM-Newton* with one central  $30'$  diameter field with a 100ks exposure and six flanking fields with 50ks exposure time each (Ueda et al. 2008). These seven pointings cover a  $1.3 \text{ deg}^2$  field. Details of the observations and data reduction procedures are described in Ueda et al. (2008).

In total, 866 and 645 sources are detected above likelihood of 7 in the 0.5–2 keV (soft) and 2–10 keV (hard) bands, respectively, through source detection utilising a maximum likelihood fit method. The spatial distribution of the sources is shown in Figure 1 (small dots). A likelihood ( $L$ ) of 7 corresponds to the probability of being a random background noise,  $P_{\text{random}}$  of  $9.1 \times 10^{-4}$  ( $L = -\ln P_{\text{random}}$ ). The 0.5–2 keV and 2–10 keV band X-ray flux distributions of the X-ray sources are shown in Figure 2. The 0.5–2 keV (2–10 keV) flux is calculated by multiplying the 0.5–2 keV (2–10 keV) count rate with  $0.167 \text{ (} 0.838 \text{)} \times 10^{-14} [\text{erg s}^{-1} \text{ cm}^{-2}] / [\text{cts ksec}^{-1}]$  (Ueda et al. 2008). These are the conversion factors for a power-law spectrum with  $\Gamma = 1.8$ , which is the typical apparent X-ray spectral slope of a non-obscured AGN.

In this paper, only X-ray sources in the region covered with deep optical imaging data described in the next section are considered. The region is shown as 5 rectangles with thin solid lines. Some of the X-ray sources whose optical images are affected by halo or electron leakage from very bright objects are removed as well. A total of 781 (584) soft (hard)-band X-ray sources with likelihood above 7 are covered. Hereafter these sources are referred as the soft-(hard)-band sample. Considering sources common to both samples, there are 945 unique X-ray sources, we refer the combined sample as the total sample. The flux distributions of the samples are shown with thick histograms in Figure 2. The corresponding survey area for the soft-(hard)-band sample is shown in the left (right) panel of Figure 3. The solid line represents the survey area of the entire sample of Ueda et al. (2008), and the dotted line shows the survey area of the sample considered in this paper.

## 3. Multi-wavelength Imaging Dataset

### 3.1. Deep Optical Imaging Data

Deep optical imaging observation in the field was conducted with the optical wide-field  $34' \times 27'$  mosaic CCD camera, Suprime-Cam, attached to the prime-focus of the 8.2m Subaru Telescope. The observation was conducted as a Subaru observatory project from September 2002 to January 2004. Imaging data in five overlapping FoVs in the  $B$ ,  $V$ ,  $R$ ,  $i'$ , and  $z'$  bands was obtained. The thin solid rectangles in Figure 1 indicate the area covered. The total exposure times for each field range 5.5–5.8h ( $B$ ), 4.9–5.3h ( $V$ ), 3.9–4.1h ( $R$ ), 5.2–10.8h ( $i'$ ), 3.1–5.2h ( $z'$ ). For details of the deep imaging data, see Furusawa et al. (2008). In

these images the FWHM of stellar objects is  $0.''7 - 0.''9$ . We apply a Gaussian convolution to make the resulting PSFs in the 5 bands constant for each region. We use the photometric zero-point provided in Furusawa et al. (2008). The typical  $2\sigma$  detection limits in  $2''$  diameter apertures are determined by measuring the standard deviation of fluxes within a fixed aperture at positions where no object is detected. The limits are 28.7( $B$ ), 28.1( $V$ ), 28.1( $V$ ), 28.0( $i'$ ), and 26.9( $z'$ ) mag. Correcting for the aperture loss for point sources, the typical magnitude limits are 28.1( $B$ ), 27.6( $V$ ), 27.6( $R$ ), 27.6( $i'$ ), and 26.6( $z'$ ) mag for the total magnitudes of point sources. The limiting magnitudes in the aperture and for the total magnitudes are summarised in Table 2. For other bands, we derive the limiting magnitudes for aperture and total magnitudes in the same way.

We use the Suprime-cam  $R$ -band astrometry as the astrometric reference frame in this paper. Astrometric calibration is carried out in the  $R$ -band images using the 2MASS point source catalog. The rms residual of the fitting is typically  $0.''03$ . The multi-wavelength data described below are aligned to the  $R$ -band image using commonly detected stellar objects.

### 3.2. U-band Imaging Data

The entire survey region is covered with the Canada France Hawaii Telescope Legacy Survey (CFHTLS<sup>1</sup>). We use the  $U$ -band data from the CFHTLS archive. The typical  $3.0\sigma$  total-magnitude limit for a point source is 26.11 mag. Part of the survey region, the southern FoV out of the 5 Suprime-cam FoVs, is covered by a deeper  $U$ -band imaging observation with Suprime-cam with 3.7 hours integration. Details of these data are described in Yoshida et al. (2008). The  $3.0\sigma$  limiting total magnitude of a point sources is 26.46 mag. The central  $37' \times 37'$  area of the survey region is also covered by a deep imaging data obtained with the Mosaic-II camera attached to the CTIO Blanco 4m telescope (Diaz-Tello et al. 2013; PI. N.Padilla). In this observation, the Sloan Digital Sky Survey (SDSS)  $u$ -band filter is used. The region covered is shown with a thin dashed line in Figure 1. The total integration time is 10h and the  $3.0\sigma$  limiting total magnitude of a point source is 26.29 mag. Because the filter systems used in the three  $U$ -band images are different, we adjust the Suprime-cam and Mosaic-II magnitudes to the photometric system used in the MegaCam. Using stars in the overlapping regions, we fit the magnitude difference between the Suprime-cam (Mosaic-II) and MegaCam photometry with a linear function of the  $U - B$  color, and apply the function to the Suprime-cam (Mosaic-II) photometry. We check the photometric zero-point of the MegaCam data using the  $B$  and  $R$  photometry from the Suprime-cam data and the  $U - B$  and  $B - R$  color-color diagram of stellar objects. The distribution of the stellar objects on the diagram is consistent with the colors derived with the SEDs of stars from Gunn & Stryker (1983).

<sup>1</sup> See <http://www.cfht.hawaii.edu/Science/CFHTLS>



### 3.3. Shallow Optical and U-band Imaging Data

For bright objects which are saturated in the deep optical images, their optical magnitudes are determined with shallow optical images taken with Wide Field Camera attached to Issac Newton Telescope.  $U$ -,  $G$ -,  $R$ -,  $i$ -,  $z$ -bands data are available. The  $G$ -,  $R$ -,  $i$ -,  $z$  optical magnitudes are adjusted to the Suprime-Cam  $B$ -,  $R$ -,  $i'$ -,  $z'$  system with magnitude offset and its color dependence derived with stars in the overlapping region.

### 3.4. NIR Imaging Data

A large part of the SXDS region is covered by the Ultra Deep Survey of UKIRT Infrared Deep Sky Survey (UKIDSS UDS; Lawrence et al. 2009). The coverage of this survey is shown with the thick solid rectangle in Figure 1. Archival image data from data release 8 (UKIDSS DR8) is used in this paper<sup>2</sup>. The stellar image size is  $0.7''$ . We use the photometric zero-point provided in the data release. The  $3\sigma$  detection limit of the image for a point source is measured to be 25.40, 24.82, 25.30 mag for  $J$ -,  $H$ -, and  $K$  bands, respectively, with a  $2.0''$  diameter aperture photometry and aperture correction for point sources. For X-ray sources outside of the UKIDSS UDS region, we do not have NIR photometric data.

### 3.5. MIR Imaging Data

#### 3.5.1. Spitzer IRAC Data

Almost the entire FoV of the SXDS is covered by the *Spitzer* observation with the Infra-Red Array Camera (IRAC) instrument obtained in the course of the *Spitzer* Wide-area Infra-Red Extragalactic (SWIRE) legacy survey project (Lonsdale et al. 2003; Lonsdale et al. 2004). Seven sources in the total sample are outside of the field covered. We use publicly available mosaiced images of IRAC (DR2 2005-06-03; Surace et al. 2005).

The FWHM of the PSFs in the IRAC images are determined to be 1.9, 2.0, 1.9, and  $2.2''$  by combining images of  $>10$  stars in the FoV, and the corresponding aperture corrections for a  $3.8''$  diameter aperture are 0.33, 0.36, 0.54, and 0.66 mag for  $3.6\mu\text{m}$ ,  $4.5\mu\text{m}$ ,  $5.8\mu\text{m}$ , and  $8.0\mu\text{m}$  bands, respectively (Surace et al. 2005). We determine the photometric zero-points of the mosaiced IRAC images using  $K-3.6\mu\text{m}$ ,  $K-4.5\mu\text{m}$ ,  $K-5.8\mu\text{m}$ , and  $K-8.0\mu\text{m}$  colors of bright blue stars following Lacy et al. (2005); values of 0.04, 0.02, 0.00, and 0.00 mag are used for stars with  $J-K$  colors bluer than 0.3 mag based on a theoretical stellar SED model (Table 5 of Lacy et al. 2005). Near-infrared photometry of stellar objects in the SXDS field is taken from the Two Micron All-Sky Survey Point Source Catalog (2MASS PSC; Skrutskie et al. 2006).  $K$ -band magnitudes in the 2MASS PSC are determined with a profile fitting method. We select blue stars with  $J-K < 0.3$  mag and examine their average  $K-3.6\mu\text{m}$ ,  $K-4.5\mu\text{m}$ ,  $K-5.8\mu\text{m}$ , and  $K-8.0\mu\text{m}$  colors. Photometry in the IRAC bands are determined with a  $3.8''$  diameter aperture with an aperture correction derived from the PSF. We determine the photometric zero-points to match the

expected colors from the theoretical stellar SED model.

The  $3\sigma$  detection limit of the image for point sources is measured to be 22.77, 22.07, 19.97, and 19.91 mag for the  $3.6\mu\text{m}$ ,  $4.5\mu\text{m}$ ,  $5.8\mu\text{m}$ , and  $8.0\mu\text{m}$  bands, respectively, with a  $3.8''$  aperture photometry diameter and assumption for the aperture correction for point sources.

Comparing the coordinates of objects detected in both of the  $R$ -band and  $3.6\mu\text{m}$ -band, we found a  $0.''36$  offset in the right ascension direction between the deep Suprime-Cam  $R$ -band and the IRAC  $3.6\mu\text{m}$ -band images. We shift the IRAC image to match the coordinates of the Suprime-Cam image. After the correction, the difference between the  $R$ -band and  $3.6\mu\text{m}$ -band coordinates is  $0.''4$  r.m.s., which is thought to be dominated by the positional uncertainty of the  $3.6\mu\text{m}$  source.

A significant part of the SXDS region is covered by one of the *Spitzer* legacy programs, *Spitzer* UKIDSS Ultra Deep Survey (SpUDS). IRAC observations cover the region shown in gray in Figure 1. The photometric zero-point of the SpUDS data is adjusted to SWIRE photometry with overlapping objects. The typical  $2.0\sigma$  detection limit for  $3.''8$  aperture is 25.26, 24.83, 22.99, and 23.19 mag and the detection limits for the point source are estimated to be 24.49 ( $3.0\sigma$ ), 24.03 ( $3.0\sigma$ ), 21.69 ( $3.0\sigma$ ), 21.77 ( $4.0\sigma$ ) mag for  $3.6\mu\text{m}$ ,  $4.5\mu\text{m}$ ,  $5.8\mu\text{m}$ , and  $8.0\mu\text{m}$  bands, respectively.

#### 3.5.2. Spitzer MIPS Data

The *Spitzer* observation with the Multiband Imaging Photometer (MIPS) instrument in the SWIRE legacy survey (Lonsdale et al. 2003; Lonsdale et al. 2004) also covers almost the entire area of the SXDS. We use publicly available mosaiced images of MIPS data in  $24\mu\text{m}$  band (DR5 2006-12-23).

The FWHM of PSF of the MIPS image is  $5.''9$ , and aperture correction for a  $6.''0$  diameter aperture is 1.23 mag<sup>3</sup>. We use the photometric zero-point provided in the data release. The  $2\sigma$  detection limit of the data in the aperture is 20.21 mag, and the  $4\sigma$  detection limit for the total magnitude of stellar objects is 18.22mag.

A large part of the SXDS region is also covered by the MIPS observation of SpUDS. The coverage is shown with the thick dashed line in Figure 1. The  $2\sigma$  detection limit in a  $6.''0$  diameter aperture is 22.06 mag, and the  $4\sigma$  detection limit in total magnitude of stellar objects is 20.07mag.

### 3.6. UV Imaging Data

Deep Imaging Survey (DIS) of the Galaxy Evolution Explorer (*GALEX*; Morrissey et al. 2007) covers almost the entire area of the SXDS in the FUV (effective wavelength of  $1516\text{\AA}$ ) and NUV (effective wavelength of  $2267\text{\AA}$ ) bands. We use the reduced data obtained from the *GALEX* archive<sup>4</sup>. The filenames of XMMLSS\_03 (29189s, 30289s), XMMLSS\_04 (27306s, 28561s), XMMLSS\_07 (27440s, 27520s), and XMMLSS\_09 (30606s, 32354s) overlap with the SXDS. The numbers in the parenthesis show

<sup>3</sup> Taken from Multiband Imaging Photometer for *Spitzer* Data Handbook Version 3.2

<sup>4</sup> See <http://galex.stsci.edu/GR6/>

<sup>2</sup> See <http://surveys.roe.ac.uk/wsa>

the total exposure times in FUV and NUV bands, respectively, for each tile.

The FWHM of the reduced images are  $5.''0$  and  $5.''1$  in the FUV and NUV images, respectively. We use the photometric zero-point provided in Morrissey et al. (2007); 18.82mag and 20.08mag for FUV and NUV bands. The aperture corrections for point sources are 0.36 and 0.59 mag for FUV and NUV bands for a  $7.''6$  diameter aperture (Morrissey et al. 2007). The typical point source limiting magnitudes estimated with the  $7.''6$  aperture photometry reach down to 25.52 ( $4\sigma$ ) and 25.15 ( $3\sigma$ ) mag in the FUV and NUV bands, respectively.

#### 4. Multi-wavelength Identification of the X-ray Sources

##### 4.1. Identification with $R$ -band Objects and Its Reliability

For each X-ray source the statistical error in the position estimated through the maximum likelihood fit,  $\sigma_{X_i}$ , is given in Ueda et al. (2008). When we match the X-ray and  $R$ -band sources, we use an uncertainty radius,  $\sigma_{X:Ri}$ , which is determined by the square of the  $\sigma_{X_i}$  and  $1.''1$  added in quadrature. The latter term represents any positional uncertainties other than  $\sigma_{X_i}$ , i.e. any systematic uncertainty in the positions of the  $R$ -band sources and X-ray sources. The term is estimated through the scatter of positional differences of X-ray sources whose  $\sigma_{X_i}$  is less than  $0.''5$  and their candidate  $R$ -band counterparts.

Sample images of three X-ray sources in the  $R$ -band are shown in the second column of Figure 4. Almost all of the X-ray sources have at least a  $R$ -band source in the  $3 \times \sigma_{X:Ri}$  radius above the detection limit of the  $R$ -band images. Some X-ray sources have multiple  $R$ -band sources within their error radii. Upper left panel of Figure 5 shows radial distribution of  $R$ -band sources down to 27.0 mag from the X-ray positions. The dotted line shows the average number density of sources outside of X-ray uncertainty area. The excess sources above the line statistically represent the counterparts of the X-ray sources. The average number density corresponds to the expected number of the contaminating sources. If we consider the region within  $2 \times \sigma_{X:Ri}$  down to  $R = 27.0$  mag, the ratio between the number of excess and contaminating sources is 0.30. It is thus important to select the most probable counterpart for each X-ray source.

At first, we identify the X-ray sources with sources detected in the  $R$ -band. We construct a catalog of  $R$ -band sources by applying SExtractor (Bertin & Arnouts 1996) to the deep Suprime-cam  $R$ -band images. In order to quantitatively select the most probable identification, we utilise the likelihood ratio defined as the probability of an X-ray source  $i$  with X-ray flux  $f_{X_i}$  having a counterpart  $j$  with magnitude  $m_j$  and distance  $r_{ij}$  divided by the probability of it being a chance match (de Ruiter 1977; Wolstencroft et al. 1986; Sutherland & Saunders 1992). The likelihood ratio is calculated as:

$$L_{ij} \equiv \frac{Q(< m_j, f_{X_i}) \exp(-r_{ij}^2 / 2\sigma_{X:Ri}^2)}{2\pi\sigma_{X:Ri}^2 N(< m_j)}.$$

assuming the spatial distribution of the counterparts in the X-ray error circles follows the Gaussian distribution.  $N(< m_j)$  is a cumulative number density of optical objects brighter than  $m_j$ .  $Q(< m_j, f_{X_i})$  is the probability of the  $i$ -th X-ray source has its counterpart brighter than  $m_j$ . If the probability of being a counterpart for the X-ray source exceeds the probability of being a chance match, the likelihood ratio is greater than 1. The number density of optical objects is calculated from the Suprime-Cam  $R$ -band image directly without correction for detection incompleteness. We determine  $Q(< m_j, f_{X_i})$  by examining the distribution of  $\log f_X / f_R$  for the X-ray sources, and assume that the distribution is constant in the SXDS X-ray flux range. We consider  $R$ -band sources within  $5.0 \times \sigma_{X:Ri}$  of each X-ray source.

Firstly, we calculate  $L_{ij}$  with  $Q(< m_j, f_{X_i}) = 1.0$  and select the  $R$ -band object with the highest likelihood ratio for each X-ray source as the initial guess for the  $R$  primary candidate. Based on the  $R$ -band magnitudes of the identified objects, we determine  $Q(< m_j, f_{X_i})$ . The  $\log f_{X_i} / f_{Rj}$  value is calculated with  $\log f_{X_i} / f_{Rj} = \log f_{X_i} + 5.53 + 0.4Rj$  in the AB magnitude system. The half-maximum wavelength range of the  $R$ -band filter response (5950Å–7085Å) of the Suprime-Cam is used in the calculation. We use the 0.5–10 keV flux, which is derived by summing the flux in the 0.5–2 keV and 2–10 keV bands, as the X-ray flux  $f_{X_i}$ . We call the  $R$ -band object with the highest likelihood ratio for a given X-ray source the  $R$  primary candidate for the source.

The reliability of the identification is evaluated as the probability that a  $R$ -band object  $j$  is the counterpart of an X-ray source  $i$ . The reliability is given by

$$R_{ij} = \frac{L_{ij}}{\sum_j L_{ij} + (1 - Q(< m_{\text{limit}}, f_{X_i}))}$$

(Sutherland & Saunders 1992).  $Q(< m_{\text{limit}}, f_{X_i})$  represents the probability of finding an  $R$ -band counterpart above the detection limit  $m_{\text{limit}}$ . We use a value of  $Q(< m_{\text{limit}}, f_{X_i})$  of 0.8 for all X-ray sources for simplicity. The cumulative distribution of the reliability of the  $R$  primary candidate is shown in Figure 6 with thick and thin black solid lines for the soft- and hard-band samples, respectively. A significant fraction of the X-ray sources have low reliability; 30% of the X-ray sources have primary optical counterpart with reliability smaller than 0.6. X-ray sources that have the  $R$  primary candidate with low-reliability have a few  $R$ -band objects with similar  $R$ -band magnitudes and distances from the X-ray position. These are the problematic cases and the fraction of such cases in the total sample is similar to those in *XMM-Newton* survey fields with similar depth (Brusa et al. 2010).

In order to quantitatively examine the reliability of the optical identification process, we conduct Monte-Carlo simulations of the optical identification procedure. We use the large catalog of the optical objects in the fields made with the deep optical imaging. We regard each optical object as an X-ray source and add pseudo X-ray flux

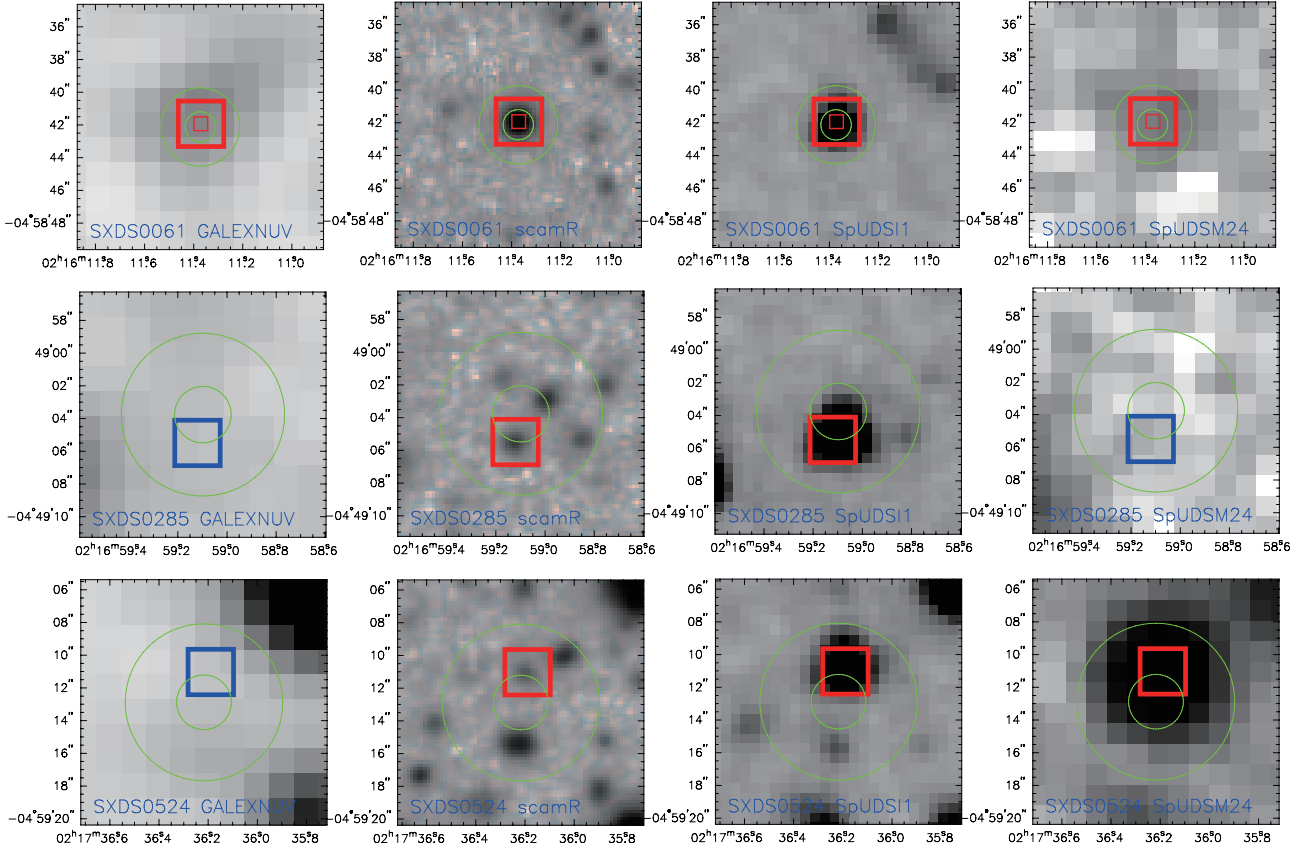


**Fig. 4.** Sample identification images. From left to right, *GALEX* NUV, Suprime-cam *R*-band, *Spitzer* 3.6 $\mu$ m-band, and *Spitzer* 24 $\mu$ m-band images with  $15'' \times 15''$  FoV. Top row for SXDS0061, whose primary candidates in the four band match, middle and bottom rows for SXDS0285 and SXDS0524, respectively, whose primary counterpart is based on the *Spitzer* 3.6 $\mu$ m identification. Green circles indicate the X-ray source position; the inner and outer circles have radii of  $1.0 \times \sigma_{X_i}$  and  $3.0 \times \sigma_{X_i}$ . The position of the primary counterpart is indicated with large open square. The small open square indicates the object selected in a AGN variability search.

information and simulate the X-ray coordinates by adding positional uncertainty to the optical coordinates. We use  $1 \times 10^{-14} \text{ erg s}^{-1} \text{ cm}^{-2}$  in the total band for the X-ray flux. We assume that the positional error follows a Gaussian distribution. We simulated a positional error  $\sigma_{X:Ri}$  of  $0.''0$  to  $3.''0$  with a  $0.''2$  step. We apply the same optical identification process described above to the pseudo-X-ray source catalog. The identification process recovers more than 90% of the counterparts for the pseudo-X-ray sources with  $\sigma_{X:Ri} < 0.''8$ , and the fraction decreases down to 40% for the pseudo-X-ray sources with  $\sigma_{X:Ri} = 2.''0$  and counterparts of  $R = 26.0 \text{ mag}$ .

It is important to evaluate the fraction of correct identifications among the *R*-band primary candidates. For pseudo-X-ray sources with  $\sigma_{X:Ri} < 0.''8$  and primary candidate of  $R < 25.5 \text{ mag}$ , 95% of the primary candidates are the correct identification. On the other hand, only 50% of the primary candidate with  $R \sim 25.0 \text{ mag}$  are correct for pseudo-X-ray sources with  $\sigma_{X:Ri} \sim 2.''0 - 3.''0$ . The results also show that even among the optical identifications with a bright optical counterpart,  $R \sim 20 \text{ mag}$ , there can be non-negligible fraction of incorrect identifications.

Based on the simulations, we can estimate the probability of mis-identification for each X-ray source with  $\sigma_{X:Ri}$

and the *R*-band magnitude of the primary candidate. Summing the probability of the mis-identification for all of the X-ray sources, we calculate the expected number of mis-identification to be 102 among the 945 sources in the total sample. The identification only with the *R*-band information is clearly affected by mis-identification.

#### 4.2. Identification with 3.6 $\mu$ m Objects and Its Reliability

Most of the expected mis-identifications are thought to be associated with X-ray sources with large  $\sigma_{X_i}$  and faint optical counterparts. Because optically-faint X-ray sources have on-average a red optical-MIR color (Yan et al. 2003; Koekemoer et al. 2004; Mignoli et al. 2004); identification in the MIR-band can be more reliable (Brusa et al. 2010; Civano et al. 2012). Upper middle and upper right panels of Figure 5 show the radial distribution of 3.6 $\mu$ m sources from the centers of the X-ray sources. For the uncertainty radius,  $\sigma_{X:3.6\mu mi}$ , we use root sum squared of the  $\sigma_{X_i}$  and  $1.''1$ . The latter term is derived same way for the *R*-band sources. If we take the ratio between the numbers of excess and contaminating sources within  $2 \times \sigma_{X:3.6i}$ , the ratios are 2.2 and 0.9 at the depth of the SWIRE and SpUDS coverages, respectively. The ratios are higher than the ratio in the *R*-band, and it is



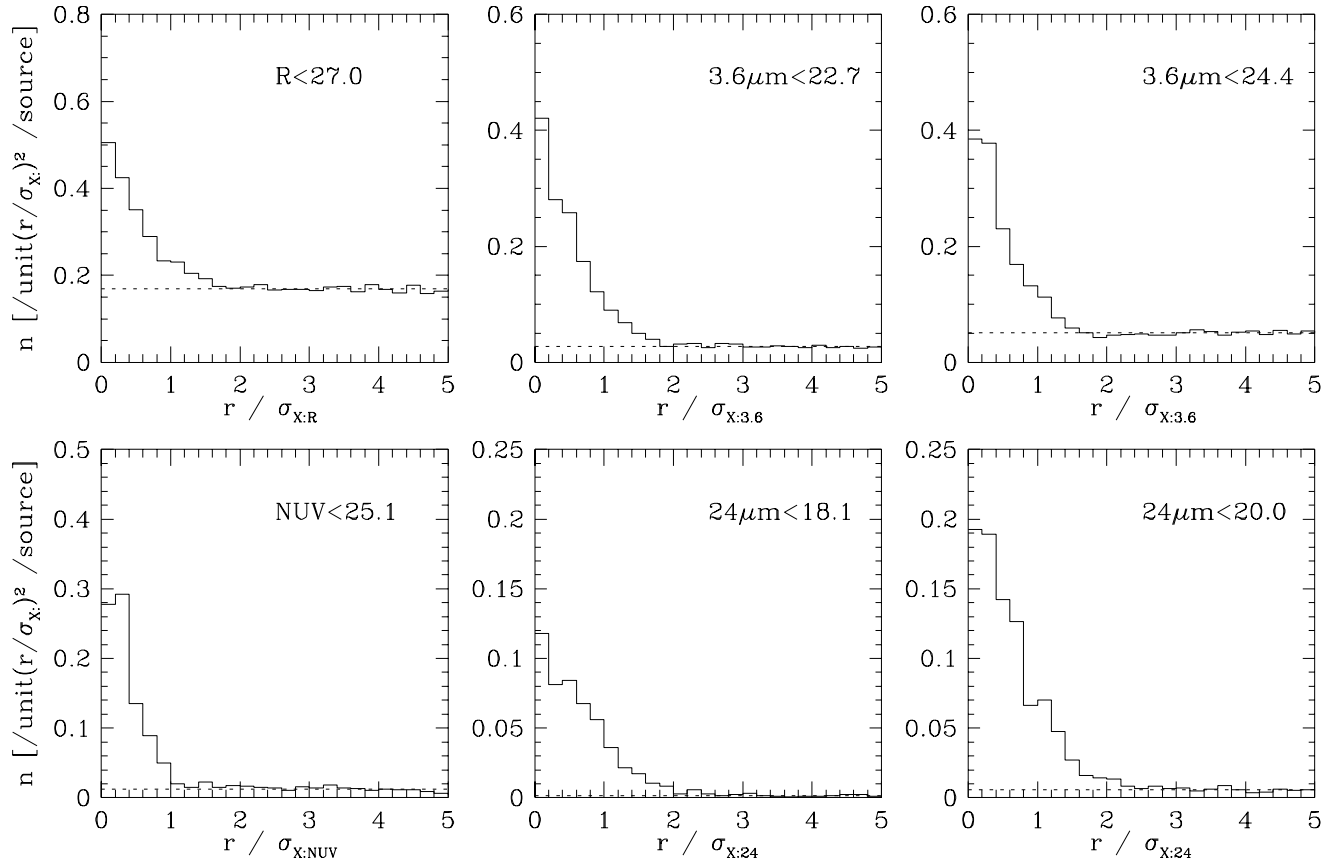


**Fig. 5.** Radial distribution of sources from the centers of the X-ray sources. Radial distance is normalized by the uncertainty radius, which is a X-ray positional uncertainty convolved with a positional uncertainty in each band. Number per unit area is divided by the number of X-ray sources covered in each dataset. Dotted lines indicate the average source density outside of X-ray uncertainty area determined at  $3.5 - 4.0\sigma_{X:\text{band}}$ . Upper left)  $R$ -band sources down to  $R = 27.0\text{mag}$ , upper middle)  $3.6\mu\text{m}$  sources down to  $22.7\text{mag}$  determined with SWIRE coverage, upper right)  $3.6\mu\text{m}$  sources down to  $24.4\text{mag}$  determined with SpUDS coverage, lower left) NUV source down to  $25.1\text{mag}$ , lower middle)  $24\mu\text{m}$  sources down to  $18.1\text{mag}$  determined with SWIRE coverage, and lower right)  $24\mu\text{m}$  sources down to  $20.0\text{mag}$  determined with SpUDS coverage.

expected that more reliable identification can be made in the  $3.6\mu\text{m}$ -band. Feruglio et al. (2008) really show that  $3.6\mu\text{m}$  identification provides a better counterpart assignment than optical only identification for *XMM-Newton* X-ray sources. They checked the  $R$  and  $3.6\mu\text{m}$  identifications of *XMM-Newton* X-ray sources with the source positions measured with *Chandra*, and found 20% and 4% different identifications from *Chandra* for the  $R$  and  $3.6\mu\text{m}$  primary candidates, respectively.

In order to improve the reliability of the identification, we apply the  $3.6\mu\text{m}$  identification utilising the SWIRE and SpUDS  $3.6\mu\text{m}$  images. First, we construct a  $3.6\mu\text{m}$  object catalog applying SExtractor (Bertin & Arnouts 1996) to the  $3.6\mu\text{m}$  images with detection criteria of 3 connected pixels above  $2\sigma$  of the background. We use MAG\_AUTO as the  $3.6\mu\text{m}$  magnitude. Then, we identify the X-ray sources with the  $3.6\mu\text{m}$  objects in the same way for the  $R$ -band objects using  $L_{ij}$  and  $R_{ij}$  determined with the  $3.6\mu\text{m}$  object list. We consider  $3.6\mu\text{m}$  sources within  $5 \times \sigma_{X:3.6\mu\text{mi}}$  of each X-ray source. The number count of the  $3.6\mu\text{m}$  objects are derived from the source number density in the  $3.6\mu\text{m}$  source catalog. We select  $3.6\mu\text{m}$  pri-

mary candidates with  $Q(< m_{3.6\mu\text{mj}}, f_{Xi}) = 1.0$ , then we derive  $Q(< m_{3.6\mu\text{mj}}, f_{Xi})$  with the  $3.6\mu\text{m}$  magnitudes of the primary candidates. Finally, we conduct the  $3.6\mu\text{m}$  identification with the derived  $Q(< m_{3.6\mu\text{mj}}, f_{Xi})$ .

The distribution of the reliability of the  $3.6\mu\text{m}$  primary candidate is shown in Figure 6 with the red dotted lines. The fraction of the high reliability identifications among the  $3.6\mu\text{m}$  identifications is higher than that among the  $R$ -band identifications: 80% of the sources have a primary candidate with  $R_{ij} > 0.8$ . We evaluate the expected number of mis-identifications among the  $3.6\mu\text{m}$  primary candidates using a Monte Carlo simulation as for the  $R$ -band identification. The mis-identification rate for all of the X-ray sources is 44 among the 945 X-ray sources. The fraction of expected mis-identifications is consistent with that reported in Feruglio et al. (2008). The expected number of mis-identifications is significantly reduced from that of the  $R$ -band identification.

The PSF size of the  $3.6\mu\text{m}$ -band IRAC image is larger than that of the  $R$ -band image, but as can be seen in Figure 4, sufficiently small to pinpoint which is more reliable counterpart among the multiple  $R$ -band sources that

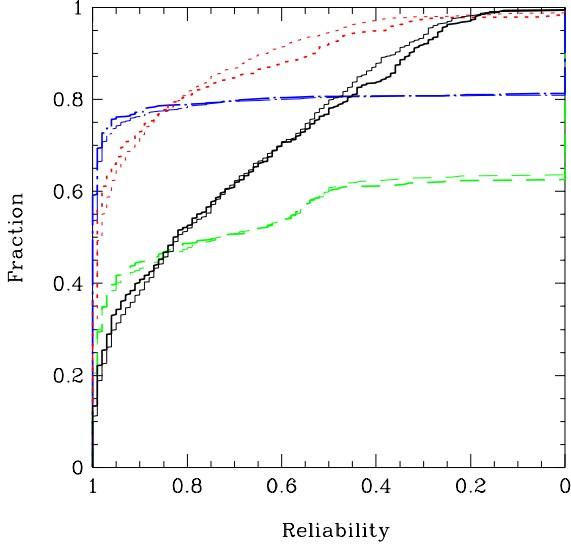


**Fig. 6.** Distribution of reliability  $R_{ij}$  for the primary candidate identified in each band. Black solid curves are for the  $R$ -band identification. Red dotted lines are for the  $3.6\mu\text{m}$  identification. Blue dot-dashed lines are for  $24\mu\text{m}$  identification. Green dashed lines are for NUV identification. The thick (thin) lines are for the hard-band (soft-band) sample.

are in the X-ray uncertainty area. We use  $3.6\mu\text{m}$  identification to pinpoint the optical counterpart, and we refer the position of the selected optical counterpart as the coordinate of the counterpart.

Similar to the  $3.6\mu\text{m}$  identification, identifications in the  $K$ -band can be effective in selecting optically-faint and red counterparts. Additionally the PSF size of the UKIDSS UDS  $K$ -band image is significantly smaller than that of the IRAC  $3.6\mu\text{m}$  image, therefore it is possible that true counterparts that are blended with contaminating sources in the  $3.6\mu\text{m}$  image can be resolved in the  $K$ -band image. Using the UKIDSS UDS  $K$ -band image, we check the difference of the  $K$ -band identifications from those in the  $R$  and  $3.6\mu\text{m}$  bands. The  $K$ -band identifications basically follow the  $R$  and  $3.6\mu\text{m}$  identifications; among 762 X-ray sources covered in the  $K$ -band image, 636 and 650 sources have  $K$ -band primary candidate consistent with primary candidate in the  $R$  and  $3.6\mu\text{m}$  identifications, respectively. If we remove  $K$ -band primary candidate which are located far outside of the X-ray error circle, there are 11  $K$ -band primary candidates that are different from both of the  $R$ -band and  $3.6\mu\text{m}$  identifications. All of the 11  $K$ -band primary candidates have reliability lower than 0.5, i.e. there are other  $K$ -band source with similar likelihood, and the identifications are marginal. Considering the similarity to the  $R$  and  $3.6\mu\text{m}$  identifications and the limited coverage of the  $K$ -band image, we do not refer the  $K$ -band identifications in the final selection of the primary counterparts.

#### 4.3. Primary Counterpart Selected with Multi-wavelength Identification

Utilising the multi-wavelength dataset of the SXDS, we can further improve the reliability of the identification.

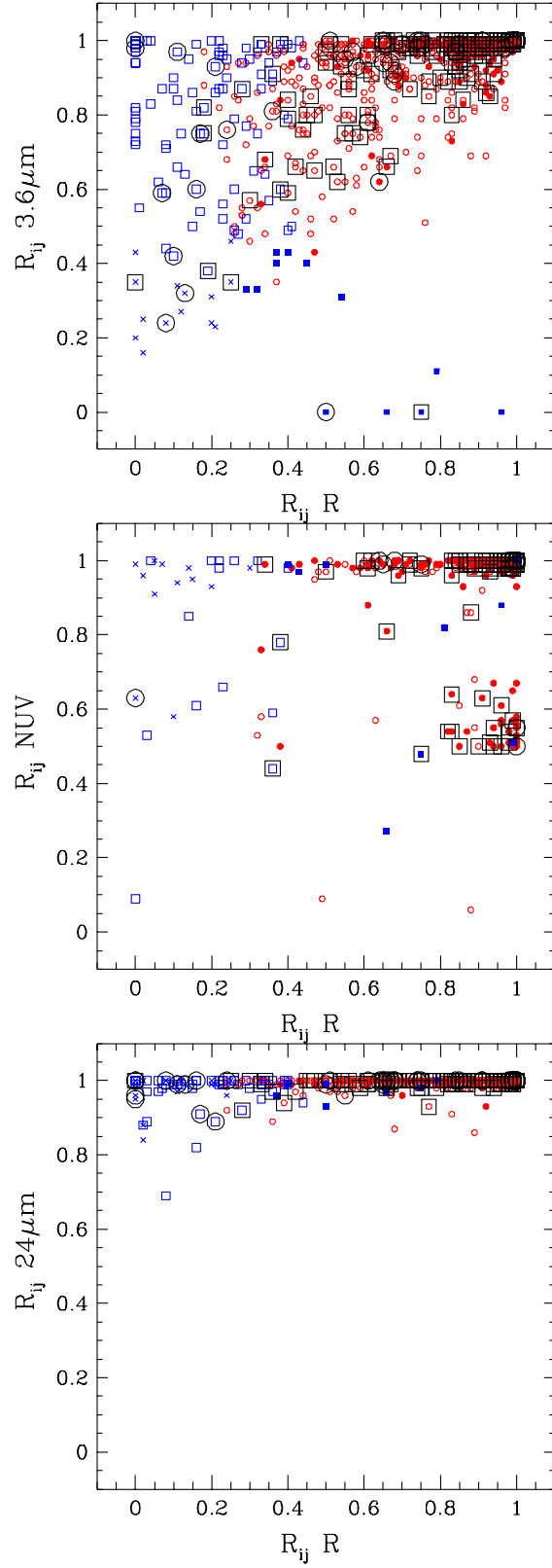


**Fig. 7.** The reliability  $R_{ij}$  determined in the  $3.6\mu\text{m}$  (top), NUV (middle), and  $24\mu\text{m}$  (bottom) bands identification vs.  $R$ -band identification. Red filled circles represent objects where all 4 identifications are the same. Red open circles have matched identifications in the  $R$  and  $3.6\mu\text{m}$  bands. Blue filled squares and blue open squares are identified either in  $R$  or  $3.6\mu\text{m}$  bands. Blue crosses are identified in the NUV or  $24\mu\text{m}$  bands. Black open squares and black open circles indicate objects matched with radio and variability AGN candidates, respectively.

Luminous blue broad-line AGNs at low to intermediate redshifts are reliably identified with strong NUV emission. On the other hand, obscured narrow-line AGNs show strong  $24\mu\text{m}$  emission. In the bottom panels of Figure 5, radial distributions of NUV and  $24\mu\text{m}$  sources are shown. The  $1\sigma$  uncertainty radius,  $\sigma_{X:\text{NUV}i}$  and  $\sigma_{X:24\mu\text{m}i}$ , are calculated with root sum of squares of  $\sigma_{X_i}$  and the additional term associated with the systematic X-ray source and NUV or  $24\mu\text{m}$  position uncertainty. We use  $2.''3$  and  $1.''4$  as the latter term for NUV and  $24\mu\text{m}$  identifications, respectively. In the same way for  $R$  and  $3.6\mu\text{m}$ -bands, if we consider within  $2 \times \sigma_{X:\text{NUV}i}$  or  $2 \times \sigma_{X:24\mu\text{m}i}$ , the ratio between the number of excess and contaminating sources are 2.5, 22.0, and 8.3 for NUV down to 25.1 mag,  $24\mu\text{m}$  down to 18.1 mag (SWIRE depth) and  $24\mu\text{m}$  down to 20.0 mag (SpUDS depth), respectively. Thus most of the associated  $24\mu\text{m}$  sources are expected to be counterparts of the X-ray sources. Some contaminations are expected for NUV sources, see discussions on the distributions of reliability below. Therefore, we utilise NUV and  $24\mu\text{m}$  identifications as well as the  $R$  and  $3.6\mu\text{m}$  identifications to determine the primary counterpart of each X-ray source. We refer a primary object selected in each identification as the primary candidate, and the best candidate in the combined identifications as the primary counterpart.

We perform NUV and  $24\mu\text{m}$  identifications in the same way as for the  $R$  and  $3.6\mu\text{m}$  identifications. First, we construct object catalogs from the NUV and  $24\mu\text{m}$  images with SExtractor. We use the NUV and  $24\mu\text{m}$  magnitude determined in  $7.''6$  and  $6.''0$  diameter apertures with aperture corrections of 0.59 and 1.23 mag determined with average PSF, respectively. The number densities of NUV and  $24\mu\text{m}$  sources are directly derived from the source list made by applying SExtractor to the SXDS dataset. For the NUV and  $24\mu\text{m}$  identifications, we do not consider  $Q(< m_j, f_{X_i})$  and set  $Q(< m_j, f_{X_i}) = 1.0$  for simplicity. We calculate  $R_{ij}$  in the same way for  $R$  and  $3.6\mu\text{m}$  identification. As shown in Figure 4, the PSF sizes of the NUV and  $24\mu\text{m}$ -band images are significantly larger than that of the  $R$ -band images. The PSF sizes are still sufficiently small to pinpoint one  $R$ -band counterpart in most of the cases. We apply eye-ball check for the  $R$ -band images of the NUV and  $24\mu\text{m}$  sources. Same for  $3.6\mu\text{m}$  identification, even if we use NUV or  $24\mu\text{m}$  identification, we refer the position of the selected optical counterpart as the co-ordinate of the counterpart.

The distribution of the  $R_{ij}$  of NUV and  $24\mu\text{m}$  identifications are shown with green dashed and blue dot-dashed lines, respectively, in Figure 6. The NUV identification is good for blue luminous broad-line AGNs, and higher reliability identification can be achieved than  $R$  identification for more than 40% of the X-ray sources. However, another 40% of the sources have multiple NUV sources with similar magnitude in the uncertainty area giving a reliability less than 0.5. In the  $24\mu\text{m}$  band we achieve highly reliable identification,  $R_{ij} > 0.8$ , for 80% of the sources. For the rest of the X-ray sources, the  $24\mu\text{m}$  data is not deep enough to detect the counterparts of the X-ray sources and the fraction is saturated at 80%. The higher reliability of

the NUV and  $24\mu\text{m}$  identifications can partly be caused by the blending effect due to the large PSF size in the two bands. The counterparts of the X-ray sources are bright in the NUV and  $24\mu\text{m}$  bands, and fainter NUV or  $24\mu\text{m}$  band sources that are contaminating and are located at the X-ray source position by chance can be hidden due to blending with the brighter true counterpart. Such effect of blending is discussed for  $3.6\mu\text{m}$  sources in Cardamone et al. (2008).

Additionally, candidates of AGNs are selected in radio and variability surveys in SXDS, and we utilise this information in the final identification. A large part ( $0.8 \text{ deg}^2$ ) of the SXDS field is covered by the Very Large Array (VLA) radio survey observation at 1.4GHz down to  $100\mu\text{Jy}$  (Simpson et al. 2006; Simpson et al. 2012). In total, 505 radio sources are detected, and 480 sources are within the X-ray coverage region. Among the 945 X-ray sources in the total sample, 789 of them are covered in the  $100\mu\text{Jy}$  sample. If we consider  $1\sigma$  positional matching uncertainty,  $\sigma_{X:\text{radio}i}$  with the root sum of squares of  $\sigma_{X_i}$  and  $1.''0$ , there are 62 radio sources associated with the X-ray sources within  $4.0 \times \sigma_{X:\text{radio}i}$ . Most of the broad-line AGNs detected in the radio survey are also detected in X-ray; among 25 broad-line AGNs detected in the VLA survey (Simpson et al. 2012), 21 of them are in the X-ray survey region, and 17 of them are associated with X-ray sources. Three radio broad-line AGNs without X-ray detection are fainter than  $i'=23.5$  mag, and are likely to be below the X-ray detection limit. The remaining radio broad-line AGN without X-ray detection are located in a gap of the X-ray detectors, and the AGN can be missed due to bad sensitivity in the region.

Variable AGN candidates are selected with  $i'$ -band Suprime-cam imaging data (Morokuma et al. 2008a; Morokuma et al. 2008b). There are 936 variable objects detected down to magnitude of the varying component of  $i'_{\text{vari}} = 25.5$  in the overlapping region with the X-ray images (Morokuma et al. 2008b), and 193 of them are matched with X-ray sources.

Finally the primary counterpart is determined utilising all of the  $R$ ,  $3.6\mu\text{m}$ ,  $24\mu\text{m}$ , and NUV identifications. Radio and variability AGN candidates are also considered during the selection of the primary counterpart.

Among the 945 X-ray sources, 213 sources have matched primary candidate considering all 4 identifications, and we select this object as the primary counterpart. 404 X-ray sources have only one object which have likelihood ratio larger than 1 either in the 4 identifications within the X-ray uncertainty area, and we select the object as the primary counterpart. For the remaining X-ray sources, there are more than 2 objects with  $L_{ij} > 1$  within the X-ray uncertainty area. We multiply the likelihood ratios of the 4 identifications for each source, and if there is an object with a likelihood ratio product larger than 1000, we select this object as the primary counterpart. There are 112 X-ray sources that meet the criteria. Of the remaining 183 X-ray sources, 90 X-ray sources have a primary candidate selected both in the  $R$  and  $3.6\mu\text{m}$  identifications. Among them, we select 77 of them as the primary coun-

terpart. For 13 X-ray sources, there is another primary candidate selected at  $24\mu\text{m}$  or in the NUV, and the candidate is selected as the primary counterpart. The other 93 X-ray sources have different primary candidates in the  $R$  and  $3.6\mu\text{m}$  identifications. For such source, we determine the primary counterpart comparing the likelihood ratios in the 4 identifications. We select 52, 24, 20, and 6 primary candidates with the  $3.6\mu\text{m}$ ,  $R$ ,  $24\mu\text{m}$ , and NUV identifications, respectively.

The distribution of the reliability of the primary counterparts in the  $R$ ,  $3.6\mu\text{m}$ ,  $24\mu\text{m}$ , and NUV identifications are shown in Figure 7. Almost all of the primary counterparts have high reliability in one of the 4 identifications. The list of the primary counterparts is shown in Table 3. In the list, the X-ray identification number (column 1), X-ray RA and Dec. position (column 2 and 3), X-ray  $1\sigma$  uncertainty radius,  $\sigma_{X_i}$  (column 4), and likelihood in the 0.5–2 keV and 2–10 keV bands (column 5 and 6) are shown. Columns 7 to 10 provide the information from the multi-wavelength identification process in the  $R$  (7), NUV (8),  $3.6\mu\text{m}$  (9), and  $24\mu\text{m}$  (10) bands. Flag 1 means the primary counterpart is the primary candidate in the band, flag  $-1$  means the counterpart is the primary candidate but the likelihood is less than 1.0, and flag 0 means the counterpart is not the primary candidate in the band. Column 11 and 12 show the matching with the 1.4GHz radio source and variability AGN candidates. The RA and Dec. of the primary counterpart is given in columns 13 and 14. The multi-wavelength images of the X-ray sources are available on-line<sup>5</sup>.

#### 4.4. Candidates of Clusters of Galaxies

The identifications discussed above assume the X-ray source is a single object. This is not the case for clusters of galaxies, which are non-negligible population among extra-galactic X-ray sources. Some of the identifications with low-reliability can be caused by the multiple galaxies associated with an X-ray source that is associated with a cluster of galaxies.

Finoguenov et al. (2010) constructed catalogs of groups and clusters of galaxies in the SXDS field through a wavelet detection of extended X-ray emission for the *XMM-Newton* imaging dataset. They cross-match their candidates with the extended sources in Ueda et al. (2008), and 14 sources in Ueda et al. (2008) are matched. Among them, we regard 10 extended X-ray sources as candidate of clusters of galaxies as listed in Table 4. Among the remaining 4 sources, we regard 3 sources as candidates of AGNs. SXDS0051 is cross-identified with SXDF47XGG at  $z = 0.348$ , but SXDS0051 is significantly detected in the 2.0–10 keV band and the observed 0.5–2 keV and 2–4.5 keV hardness ratio, HR2, is relatively large ( $-0.50$ ). Thus we regard the X-ray source as an AGN candidate. SXDS0396 is cross-identified with SXDF64XGG at  $z = 1.030$ , but SXDS0396 is significantly detected in the 2.0–10 keV band and HR2 ( $-0.36$ ) implies a power-law with photon index of 1.6. Therefore,

we regard the X-ray source as an AGN candidate. The source is also close to SXDS0386. SXDS0934 is cross-identified with SXDF06XGG at  $z = 0.451$ , but the primary optical counterpart is identified with a broad-line AGN at  $z = 1.669$ , therefore we regard the AGN as the X-ray source. SXDS0784 matched with SXDF07XGG has a detection likelihood less than 7 in both of the soft and hard X-ray bands, and it is not included in the total sample.

We also found 4 additional candidates of clusters of galaxies with an excess of objects with similar  $B - z'$  and  $z' - K$  colors within  $r = 15''$  from the X-ray source position. These are also listed in Table 4. The median photometric redshift of objects within  $r = 30''$  from the X-ray position is used as the photometric redshift for the candidates.

In the table, the X-ray source ID (Column 1), HR2 (2), spectroscopic redshift (3), and photometric redshift (4) are summarised.

#### 4.5. Candidates of ULXs

Four X-ray sources, SXDS0416, SXDS0390, SXDS0404, and SXDS0402, are associated with a bright nearby galaxy KUG 0214–057 at  $z = 0.018$  (Watson et al. 2005). They are strong ultra-luminous X-ray sources (ULXs) candidates.

### 5. Spectroscopic Identification

#### 5.1. Optical Spectroscopic Observations

##### 5.1.1. FOCAS/Subaru Observation in Selected Fields

We conducted a spectroscopic campaign observation with a multi-slit optical spectrograph, FOCAS on the Subaru telescope from January 2001 to November 2005. We targeted the primary counterparts with the highest priority, and in addition we observed secondary counterparts if possible. We put the slits at the positions of the primary counterparts determined in the optical images, even for primary counterparts selected by the identifications in the  $3.6\mu\text{m}$ ,  $24\mu\text{m}$ , or NUV band. The situation is the same for following spectroscopic observations. The FoV of the instrument is a  $6'$  diameter circle. In total 50 fields were observed. About three quarters of the fields were selected to cover as many as X-ray sources as possible. The remaining fields were chosen to cover as many as  $z \sim 1$  red sequence galaxies as possible (Yamada et al. 2005) and to cover a candidate  $z = 5.7$  cluster of galaxies found by narrow-band surveys (Ouchi et al. 2005; Ouchi et al. 2008). In such fields, X-ray sources are observed as a filler targets for the masks.

In the observations, we use a 150R grating with SY47 order-cut filter to cover 4700Å to 9400Å. A slit width of  $0''.8$  is used and the resulting spectral resolution is 20Å. Hereafter, we use the spectral resolution measured with night sky emission lines obtained simultaneously with the target spectrum. The spectral resolution for the target can be higher because the slit illumination by a stellar object can be more concentrated than the smooth illumination by night sky emission. In later observations, we

<sup>5</sup> See [http://www.astr.tohoku.ac.jp/~akiyama/SXDS/post\\_stamp.html](http://www.astr.tohoku.ac.jp/~akiyama/SXDS/post_stamp.html)



use 300B grating with order-cut filter SY47 or without the filter. With the order-cut filter the spectral coverage is 4700Å to 9200Å. Without the filter the spectral coverage in the blue extends down to 3800Å, but 2nd order light can contaminate wavelength range above 7600Å. A slit width of 0."8 is used and the resulting spectral resolution is 13Å. The central coordinate, observing mode, and the exposure time of each field are summarised in Table 5. During the observation, a few additional objects were observed in long-slit mode with 300B grating with SY47 order-cut filter.

The data are reduced with a script based on IRAF. The procedure follows usual analysis of long-slit observations. The bias counts are subtracted using the overscan area of the CCD, and a flat-fielding correction is applied with a dome flat frame taken after the observation. Wavelength calibration is performed using a ThAr lamp spectrum. We did not dither the object position along the slit during the observation, and the sky subtraction is performed by using the sky spectra obtained on either side of an object. The flux calibration of the reduced spectra is carried out utilising the spectra of spectroscopic standard stars taken with a 2."0-width slit. Feige 110 and G191B2B are used as the standard stars. The standard stars are obtained with and without SY47 order-cut filter, in order to evaluate the contamination of the 2nd order light at the red end of the wavelength coverage. The sensitivity curve for each night is determined with the standard stars. Furthermore, we adjust the normalization of the spectra of the targets using their photometric data. After the sensitivity correction, we also applied correction for atmospheric absorption features, A-band and B-band, using the absorption profile of the bands derived with a bright object in the same mask.

#### 5.1.2. 2dF/AAT Observation for Bright Optical Counterparts

Spectroscopic follow-up observations for bright optical counterparts with  $R < 21.0$  mag were obtained with the 2dF 400 multi-fibre optical spectrograph on Anglo-Australian 3.9m Telescope on 3-6 Nov. 2002 in director's discretionary time. The integration time ranges from 6 min for the brightest objects to 3 hours for the faintest objects. The 2dF has 2 spectrographs, each spectrograph covers 200 fibres. We used a 270R grating with wavelength range of 4400-9100Å for the first spectrograph, and 316R grating with wavelength range of 4700-8500Å for the second spectrograph. The spectral resolutions are 14 and 12Å and the spectral samplings are 4.8 and 4.1Å pixel<sup>-1</sup> for the former and latter spectrographs. We observed a relatively bright star in each fibre configuration in order to correct wavelength dependence of the sensitivity. The data are reduced in the standard way for the 2dF data using the *2dfdr* software.

#### 5.1.3. Additional Spectroscopic Observations for Faint Optical Counterparts

Some of the radio and X-ray sources in the SXDS field were observed with the Visible Multi-Object Spectrograph (VIMOS) on the Very Large Telescope (VLT) (P074.A-0333; Simpson et al. 2012). The MR-Orange grating and the GG475 order-cut filter were used and a spectral res-

olution of 10Å in the wavelength range between 4800 Å and 10,000 Å is achieved. 27 slit masks were prepared to cover ~80% of the radio and X-ray sources in the SXDS. ~75% of the 27 masks were observed with one 2700-s and two 1350-s exposures.

Additionally, two FoVs of VIMOS were observed in the course of spectroscopic observations of extended Ly $\alpha$  emitters by Saito et al. (2008) (P074.A-0524). The HR-Orange grism and the GG435 order-cut filter were used. The wavelength range between 5000 and 6800Å was covered with 2.8Å resolution.

A deep spectroscopic survey for  $K$ -band selected galaxies in the UKIDSS UDS region was conducted with the VLT VIMOS and VLT Focal Reducer and low dispersion Spectrograph 2 (FORS2) instruments in the UDSz ESO Large Programme (180.A-0776, PI:Almaini; Bradshaw et al. 2013; McLure et al. 2013). In the VIMOS observations, the LR-Blue and LR-Red grisms were used for each mask and wavelength range between 3700-9500Å was covered. A spectral resolution of 35Å was achieved at 7000Å. The FORS2 observations were conducted with a 300I grism covering 6000-10000Å and with spectral resolution of 12Å.

In the course of the optical spectroscopic survey of Lyman Alpha Emitters and Lyman Break Galaxies in the SXDS field, the primary counterparts of the X-ray sources were observed as filler objects in the masks. A multi-object spectroscopic observation with the DEep Imaging Multi-Object Spectrograph (DEIMOS) instrument attached to the Keck II telescope was also carried out (Ouchi et al. 2009). The observations used the 830G grating and the GG495 filter. The 5700-9500Å wavelength range was covered with a spectral resolution of 2.6Å.

Further spectroscopic survey observations were made with the Inamori-Magellan Areal Camera and Spectrograph (IMACS) on the Magellan 6.5m Baade telescope (Ouchi et al. 2009). In the IMACS observations, the F/2 camera with 27.4 diameter FoV and 300 lines mm<sup>-1</sup> grism with central wavelength of either 6700Å or 8000Å were used. Wavelength ranges of from 4700Å to 8000Å (from 6200Å to 9600Å) were covered with 7Å (6Å) resolution and 1.34Å pixel<sup>-1</sup> (1.25Å pixel<sup>-1</sup>) by the former (latter) setup.

X-ray sources are also observed as filler targets during spectroscopic observations of the Balmer-break galaxies in the field with IMACS on Magellan Baade telescope (PI. N.Padilla; Diaz-Tello et al. 2013). In the observation, the F/2 camera with 27.4 diameter FoV and 200 lines mm<sup>-1</sup> grism with central wavelength of 6600Å was used. The wavelength range from 4500Å to 9000Å is covered with 10Å spectral resolution and 2.0Å pixel<sup>-1</sup> sampling.

Some QSO candidates identified with the KX selection technique were spectroscopically observed with the AAOmega spectrograph on the AAT 3.9m telescope and X-ray AGNs are also observed as filler targets (Smail et al 2008). The 580V and 385R gratings were used in the dual-beam spectrograph of AAOmega and the wavelength range from 3700Å to 8600Å was covered simultaneously. Spectral resolution is 5.0Å with spectral sampling of 3.4Å pixel<sup>-1</sup>.

### 5.2. NIR Spectroscopic Observations with FMOS

In addition to the optical spectroscopic observations, we conducted intensive NIR spectroscopic observations with the Fiber Multi Object Spectrograph (FMOS) on the Subaru telescope (Kimura et al. 2010). This instrument can observe up to 200 objects simultaneously over a 30' diameter FoV in the cross-beam switching mode with two spectrographs, IRS1 and IRS2. The fibers have an aperture of 1.''2 diameter on the sky. The spectrographs cover the wavelength range between 9000Å and 18000Å with spectral resolution of  $R \sim 800$  at  $\lambda \sim 1.55\mu\text{m}$  in the low-resolution mode. A total of 851 sources were observed in observations of 22 FoVs with this setup during guaranteed, engineering and open-use (S11B-098 Silverman et al. and S11B-048 Yabe et al.) time observations. The central coordinate, observation period, integration time, and observing mode of each FoV are summarised in Table 6.

The NIR spectra are reduced with the pipeline data reduction software, FIBRE-pac (Iwamuro et al. 2012). The resulting one-dimensional spectra are corrected for atmospheric absorption and sensitivity dependence on wavelength using relatively faint F-G type stars observed simultaneously with the targets.

### 5.3. Spectroscopic Identification Summary

The primary counterparts of 31 X-ray sources with a bright stellar object show optical spectra consistent with Galactic stars. We identify them as Galactic stars. The ID number and HR2 of the X-ray sources are given in Table 7. Almost all of them have a small HR2 value, which is consistent with the thermal X-ray emission from Galactic stars. Hereafter, we exclude X-ray sources that are selected as candidates of clusters of galaxies (Section 4.4), ULXs (Section 4.5), and Galactic stars, and refer to the remaining X-ray sources as AGN candidates. There are 896 AGN candidates in the total sample as summarised in Table 1.

Among the primary counterparts of the 896 AGN candidates, 597 counterparts are observed in the optical spectroscopic observations discussed above, as is summarised in Table 1. As a first step, we determine the redshift of each object by examining its optical spectrum and fitting Gaussian profiles to the observed emission and absorption lines.

A large fraction of objects show multiple features. If a narrow emission line is detected, we determine the redshift with that line. For example, if [O II]λ3727 emission line is detected, we determine the redshift of the object with that emission line. For low-redshift objects, the optical spectrum covers the Hα and Hβ wavelength range and shows strong [O III]λ5007 emission line. We determine their redshifts with the [O III]λ5007 line. For high-redshift objects, optical spectrum covers the rest-frame wavelength range below Mg IIλ2800 emission line. If that emission line is detected, it is used to determine the redshifts, otherwise, C III]λ1909 or C IVλ1550 emission lines are used. For objects only showing absorption lines, we determine their redshift with the Ca II HK doublet absorp-

tion lines at 3969Å and 3934Å, if these absorption lines are detected.

We regard a permitted emission line with velocity width larger than 1000 km s<sup>-1</sup> (after deconvolving the instrumental profile) as a broad-emission line. This threshold is narrower than the typical criteria for broad-line AGNs (1500 or 2000 km s<sup>-1</sup>). We set the threshold considering the distribution of the FWHM of the broad-line AGNs in the local Universe (Hao et al. 2005; Stern & Laor 2012). Although the threshold is narrower, most of the broad emission lines are broader than 1500 km s<sup>-1</sup> and the distribution of the FWHM of the broad-emission lines, especially the lack of the broad-emission lines below 1500 km s<sup>-1</sup>, is similar to that of optically-selected broad-line AGNs in the SDSS as discussed in Nobuta et al. (2012).

Some objects only show one either broad or narrow emission line in the observed optical wavelength range. For such objects, we identify most of the single narrow-emission lines with [O II]λ3727, considering the absence of any other emission line. If the identification is not conclusive due to the narrow wavelength coverage of a spectrum, we identify the single narrow-emission line, utilising the photometric redshift described in the next section. For objects with one prominent broad emission line, we mostly identify it with Mg IIλ2800, consistent with the absence of another broad emission line in the observed wavelength range. The identifications with a single broad-emission line in the optical are checked with the NIR spectra covering rest-frame optical wavelength range.

Intensive spectroscopic observations in the NIR wavelength range cover 851 of the total X-ray sources as summarised in Table 1. Spectroscopic identification in the NIR spectra is conducted in the same manner as for the optical spectra. In the NIR spectra, if one narrow or broad emission line is detected, almost all of them are identified with the Hα emission line. We identify some single narrow-emission lines with [O III]λ5007, considering the photometric redshift. In such cases, [O III]λ4959 is presumed to be weaker than the detection limit. Among the objects that are observed but not identified in the optical spectroscopy, 23 objects are identified with NIR spectroscopic observations with FMOS. They are AGNs at  $z \sim 0.9 - 2.5$ , and 15 of them are narrow-line AGNs, which are mostly identified through their strong Hα or [O III]λ5007 lines.

Objects that show broad-emission in at least one of the observed permitted emission lines are referred with "broad-line" AGN, hereafter. It needs to be noted that the criteria is not homogeneous and depends on the rest-frame wavelength coverage of the optical and NIR spectroscopic observations. For example, some objects are identified as "broad-line" AGN with one prominent broad Hα emission line, but the same objects can be identified as "narrow-line" AGN, if spectra covering Hα line are not available. Furthermore, an object with broad Hα emission lines can be type 1, 1.5, 1.8 or 1.9 Seyferts. On the other hand, objects without broad-emission lines are referred with "narrow-line" AGNs. Considering the X-ray luminosity distribution of the sample, their X-ray emis-

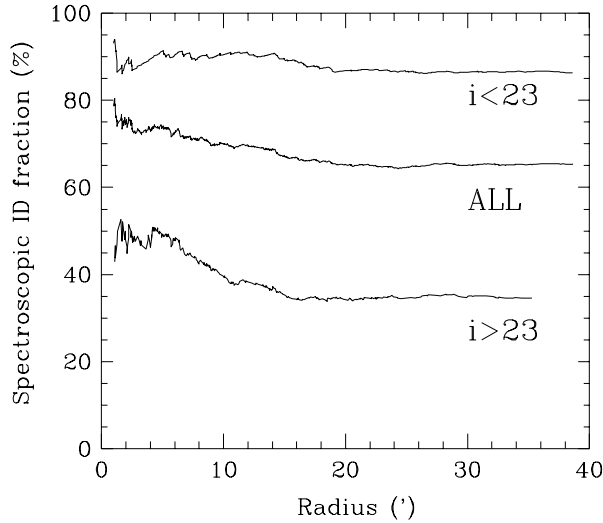


**Fig. 8.** Spectroscopic identification rate of the AGN candidates as a function of radius from the center of the survey field. From top to bottom, the lines are for X-ray sources with primary counterparts brighter than  $i' = 23$  mag, for all X-ray sources, and for X-ray sources with  $i' > 23$  mag.

sion is thought to be dominated by the AGN component, and we ignore contributions to X-ray sources from star-forming galaxies in the AGN candidates.

Utilising the optical and NIR spectra, 586 out of the 896 AGN candidates (65%) are spectroscopically identified. The fraction of spectroscopically identified objects in the entire AGN candidate sample is shown in Figure 8 as a function of radius from the center of the survey field. If we limit the sample to primary counterparts brighter than  $i' = 23$  mag, the identification rate reaches 86%. The spectroscopic identification of each AGN candidate is summarised in Table 10. Column 22 shows the spectroscopic redshift, and column 23 describes the classification. BLA and NLA represent broad-line and narrow-line AGNs, respectively. NID indicates the object is observed in the optical but can not be identified with the optical spectrum. NSP indicates the object is not observed in the optical. NID and NSP do not refer the availability of NIR spectrum.

## 6. Multi-wavelength Photometry and Photometric Redshift Determination

### 6.1. Multi-wavelength Photometry

For X-ray sources without spectroscopic identification, we determine their photometric redshifts. In order to determine photometric redshifts reliably, we conduct multi-wavelength photometry of each primary counterpart paying careful attention to the difference in the PSF size and shape.

In the photometry, the  $i'$ -band image taken with Suprime-cam is used as the reference frame for the object detection. SExtractor is used with a detection threshold of 3 connected pixels above  $2.0 \sigma$ . The aperture magnitude determined with a variable elliptical aperture

(MAG\_AUTO) is used as the  $i'$ -band total magnitude of an object. We use PHOT\_AUTOPARAMS of (2.5, 3.5) to determine the variable elliptical aperture. With the parameters, 94% of total flux will be covered within the variable elliptical aperture (Bertin & Arnouts 1996). Using the  $i'$ -band detected catalog, optical colors of the object are measured in  $2''.0$  diameter aperture using the multi-image mode of SExtractor. The total magnitude in each optical band is determined with a fixed aperture color and the aperture correction determined in the  $i'$ -band, i.e. the difference between  $i'$ -band MAG\_AUTO and  $i'$ -band MAG\_APP.

For photometry in wavelengths other than the optical bands, we measure a fixed aperture color between a selected band and  $i'$ -band using the PSF-matched  $i'$ -band image whose PSF is matched to the image in the selected band. The fixed aperture color is converted into the total magnitude in the selected band using the difference between the  $i'$ -band MAG\_AUTO in the original  $i'$ -band image and the aperture magnitude measured in the PSF-matched image. We try to conserve the fixed aperture color, and assume the light profile in the selected band follows that in the  $i'$ -band. The details are described as follows.

At first we subtracted the background component of each image using the object detection software, SExtractor. The background is determined locally with median filtering in a  $48''$  box. For very bright and extended objects with sizes larger than  $30''$ , i.e. nearby galaxies, the background removal subtracts the extended halo component, thus the photometry is not reliable for such objects. Background-subtracted images are magnified and aligned to Suprime-cam  $i'$ -band imaging data. Coordinate conversions are determined with positions of common bright stars using the **geomap** command in IRAF with a 2nd order polynomial and the images are registered with the **gregister** command. Fluxes of objects in the original images are conserved.

The PSF size of the Suprime-cam  $i'$ -band image is the smallest amongst the multi-wavelength data. We make the PSF-matched  $i'$ -band images by convolving with a kernel which represents the PSF difference between the  $i'$ -band and a given band. The determination of the kernel and the convolution is performed with the **psfmatch** command in IRAF.

After matching the PSF size and shape, we measure colors of objects with the multi-image mode of SExtractor. Colors in the  $i'$ -band and a given band are measured from the images in the band and the PSF-matched  $i'$ -band at the position in the original  $i'$ -band image. The total magnitude in the band is derived from the aperture photometry and the aperture correction derived from the difference between the MAG\_AUTO in the original  $i'$ -band image and the MAG\_APP in the PSF-matched  $i'$ -band image. Different aperture diameters are used for different datasets;  $7''.6$  diameter for GALEX FUV and NUV,  $2''.0$  diameter for  $U$ -band images, and UKIDSS  $J$ ,  $H$ , and  $K$ -bands,  $3''.8$  diameter for the IRAC images.

The uncertainties in the photometric measurement are



determined as the  $1\sigma$  uncertainty of the flux measurement in the aperture magnitude assuming a background limited regime. For bright objects, the systematic uncertainty dominates the measurement uncertainty, and constant values, 0.01-0.05 mag depending on wavelength, are added to represent such systematic uncertainties.

In order to obtain photometric data for primary counterparts that are not detected in the  $i'$ -band selected catalog, we also construct  $B$ -,  $R$ -,  $V$ -,  $z'$ - and  $3.6\mu\text{m}$  band selected catalogs using the images in each band as the reference frame. We apply the same procedures as for the  $i'$ -band selected catalog.

The results of the multi-wavelength photometry are summarised in Table 8, 9, and 10. The total magnitude and associated error for each band are given. An error of 99.99 indicates the associated magnitude is an upper limit. A total magnitude of 99.99 indicates the object is not covered in the imaging data of that band. The values in the tables are corrected for Galactic extinction. The applied corrections are summarised in Table 2.

In the photometric redshift determination, we consider the stellarity of the primary counterpart. The stellarity is determined in the deep  $i'$ -band image. For objects brighter than  $i' = 20.0\text{mag}$ , the CLS\_STAR parameter from SExtractor is used. An object with CLS\_STAR larger than 0.90 is classified as stellar. For fainter objects, we use the FWHM in the  $i'$ -band image to define stellar objects. If the  $i'$ -band FWHM is smaller than  $0''.9$ , an object is classified as stellar. For bright objects with saturation in their peak, the stellarity measurements are not reliable. In such cases we check the optical images by eye, and assign the corrected stellarity in the catalog. The resulting stellarity is also listed in Column 21 of Table 10.

## 6.2. Photometric Redshift Determination with Galaxy and QSO SED templates

The photometric redshift of each primary counterpart is determined with the hyperz code (Bolzonella et al. 2000), which determines photometric redshifts via template fitting with  $\chi^2$  minimization of the multi-wavelength photometry ranging from  $1500\text{\AA}$  to  $8.0\mu\text{m}$ . We use two sets of templates, one represents galaxy SEDs and the other one represents QSO SEDs.

For each object, we determine photometric redshifts from the galaxy and QSO templates separately. For the galaxy templates, we use the spectral evolutionary models of Bruzual & Charlot (1993) with Miller & Scalo Initial Mass Function (IMF) (Miller & Scalo 1979) and evolving metallicity. It needs to be noted that we assume a Salpeter IMF (Salpeter 1955) in the determination of stellar mass of host galaxies of narrow-line AGNs in Section 7.2 in order to compare with results in literature. The difference in the estimated photometric redshift caused by the difference in the applied IMF is expected to be negligible. In the hyperz code, Burst, constant, and  $\tau$  models with  $\tau = 1\text{Gyr}$  to  $30\text{Gyr}$  are available. The dust extinction curve of star-forming galaxies (Calzetti et al. 2000) is utilised with  $A_V = 0.0\text{mag}$  to  $A_V = 2.5\text{mag}$  in step of  $\delta A_V = 0.5$ .

The galaxy templates only represent the stellar continuum component, and neither the excess emission of an AGN hot dust component nor PAH emission are included, although such emission can affect the rest-frame wavelength range above  $2\mu\text{m}$ . Instead of including such a component in addition to the galaxy SED model, we increase the IRAC photometric errors to compensate.

For QSO templates, we construct our own QSO template by combining average UV-optical average SEDs from SDSS and NIR-MIR SEDs of QSOs from Infrared Space Observatory (*ISO*) observations. We use average QSO SEDs in Richards et al. (2003) in the wavelength range between  $1200\text{\AA}$  and  $7000\text{\AA}$ . A total of 6 average QSO SEDs are constructed depending on the UV-optical color. We extend the SED to the shorter wavelength range by extrapolating the continuum component in the above range with a power-law. In the longer wavelength range above  $1\mu\text{m}$ , we used three QSO IR SEDs from Leipski et al. (2005). The SEDs are constructed from the *ISO* observations of broad-line QSOs. By adjusting the normalization, we connect the six optical and the three IR SEDs smoothly and make 18 QSO templates covering UV to MIR wavelength range. Because the observed slopes in the UV-optical and IR wavelength ranges are independent, we consider SEDs with blue UV-optical SED and red IR SED, and vice versa. The templates are compared with the observed SEDs of spectroscopically-identified broad-line AGNs in Figure 9. All of the SEDs are normalized at  $1\mu\text{m}$  in the rest-frame. The red and blue dots represents SEDs of X-ray AGNs with absorption characterised by a hydrogen column density,  $N_{\text{H}}$ , larger than and smaller than  $10^{22}\text{ cm}^{-2}$ , respectively. The derivation of  $N_{\text{H}}$  is described in Section 7.1. The templates enclose the entire range of SEDs of broad-line AGNs, although some AGNs with  $\log N_{\text{H}} > 22.0$  show redder SED in the UV to optical wavelength range. Their SEDs are similar to the galaxy SEDs (see Section 7.3). The templates also cover the variety of the SEDs observed in the X-ray-selected broad-line AGNs in the COSMOS survey (Elvis et al. 2012).

In the template fitting, two additional constraints are applied in addition to the  $\chi^2$  minimization. The first one is that an object with stellar morphology in the  $i'$ -band image is assumed to be at  $z > 0.8$ . In the left panel of Figure 10, the  $i'$ -band magnitudes of the spectroscopically-identified objects are shown as a function of redshift. Stellar objects are shown with asterisks and crosses in this figure. Out of 261 stellar objects, 209 are spectroscopically identified. A total of 182 and 27 of them are identified with broad-line and narrow-line AGNs at  $z > 0.8$ , respectively. Stellar broad-line AGNs show bright nuclei and their observed optical light is dominated by the nuclear component with stellar morphology. It should be noted that this constraint is only applicable to the X-ray samples with similar depth and area to SXDS. As shown in Section 7.1, in the limited area of the SXDS, there is a correlation between redshifts and luminosities, therefore luminous ( $\log L_{2-10\text{keV}} > 44$ ) broad-line AGNs, i.e. QSOs, whose optical morphologies are dominated by the nuclear component, statistically appear only



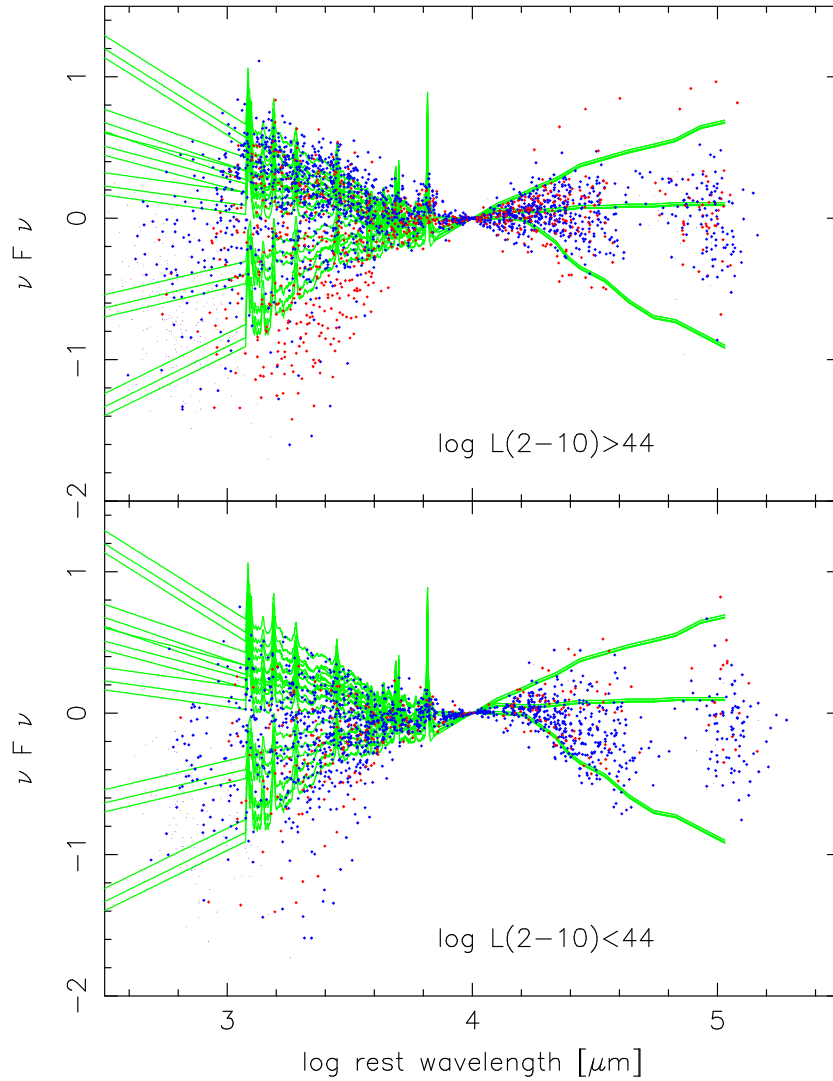


**Fig. 9.** Template SEDs for QSOs (green solid lines) compared with UV to MIR SEDs of spectroscopically-identified broad-line AGNs. Blue and red symbols represent broad-line AGNs with X-ray absorption smaller and larger than  $\log N_{\text{H}} = 22.0$ , respectively. Small dots indicate upper limits.

above  $z > 0.8$ . Such correlation is a typical of flux-limited surveys. Less-luminous broad-line AGNs are found at lower-redshifts and they show extended morphologies due to their host galaxies. Stellar narrow-line AGNs are not resolved possibly due to the fact that they are at high redshifts.

An additional consideration is the absolute magnitude range of the galaxy and QSO templates. Taking into account the absolute magnitude ranges of spectroscopically identified AGNs, we limit the  $z$ -band absolute magnitude range of the galaxy (QSO) template to lie between  $M_z = -20.0$  and  $-25.0$  mag ( $M_z = -22.0$  and  $-26.5$  mag). In Section 7.3, it will be shown that the rest-frame optical to NIR continuum of narrow-line AGNs are dominated by stellar continuum of their host galaxies. Moreover, the range of the estimated stellar mass of the host galaxies of spectroscopically-identified narrow-line AGNs is limited (see Section 7.2). Such limited mass range of X-ray AGN

host galaxies has already been reported (e.g. Yamada et al. 2009). The absolute magnitude range of galaxy template corresponds to the stellar mass range of  $10^{10} \sim 10^{12} M_{\odot}$  with the galaxy SED templates used in Section 7.2. We introduce the faint limit of the QSO absolute magnitude range, because the host galaxy component will dominate the total magnitudes if nuclear component is fainter than the limit. These consideration is necessary to reduce the number of outliers in photometric redshift estimation.

Once we determine photometric redshifts with both of the QSO and galaxy templates for each AGNs, we compare the minimum  $\chi^2_{\nu}$  with QSO templates,  $\chi^2_{\nu \text{ QSO}}$ , and that with galaxy templates,  $\chi^2_{\nu \text{ GAL}}$ , to chose the best photometric redshift for each AGNs. In the left panel of Figure 11,  $\chi^2_{\nu \text{ QSO}}$  and  $\chi^2_{\nu \text{ GAL}}$  are compared for spectroscopically-identified AGNs. The redshift is not fixed to their spectroscopic redshift during the fitting process, in order to include the effect of redshift uncer-

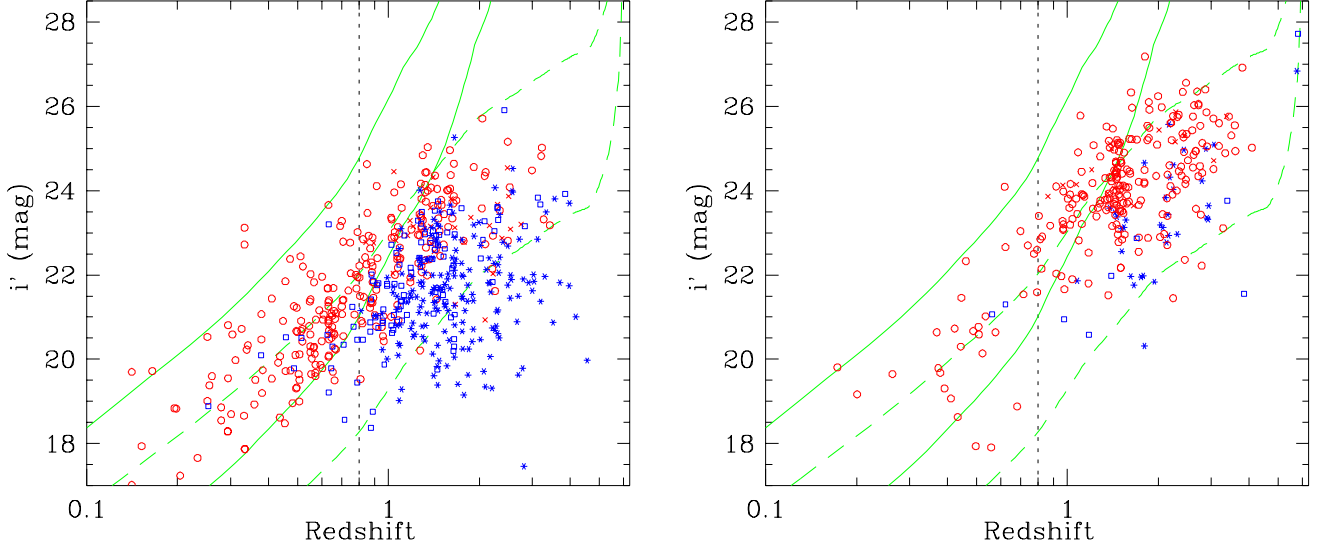


**Fig. 10.** Left) Stellarity distribution of spectroscopically identified AGNs plotted on the redshift vs.  $i'$ -band magnitude plane. Blue asterisks and red crosses represent AGNs with stellar morphology in the  $i'$ -band image. Blue (square and asterisk) and red (circle and cross) symbols show broad-line and narrow-line AGNs, respectively. The vertical dotted line marks  $z = 0.8$ . The green lines indicate the redshift evolution of the  $i'$ -band magnitude for a 10Gyr-old (solid) and 2Gyr-old (dashed) single burst stellar population with stellar mass of  $\log M_* = 10.5$  (upper) and  $\log M_* = 12.0$  (lower). Right) Same for AGNs without spectroscopic identification. In this panel, AGNs are classified photometrically as described in Section 6.2.

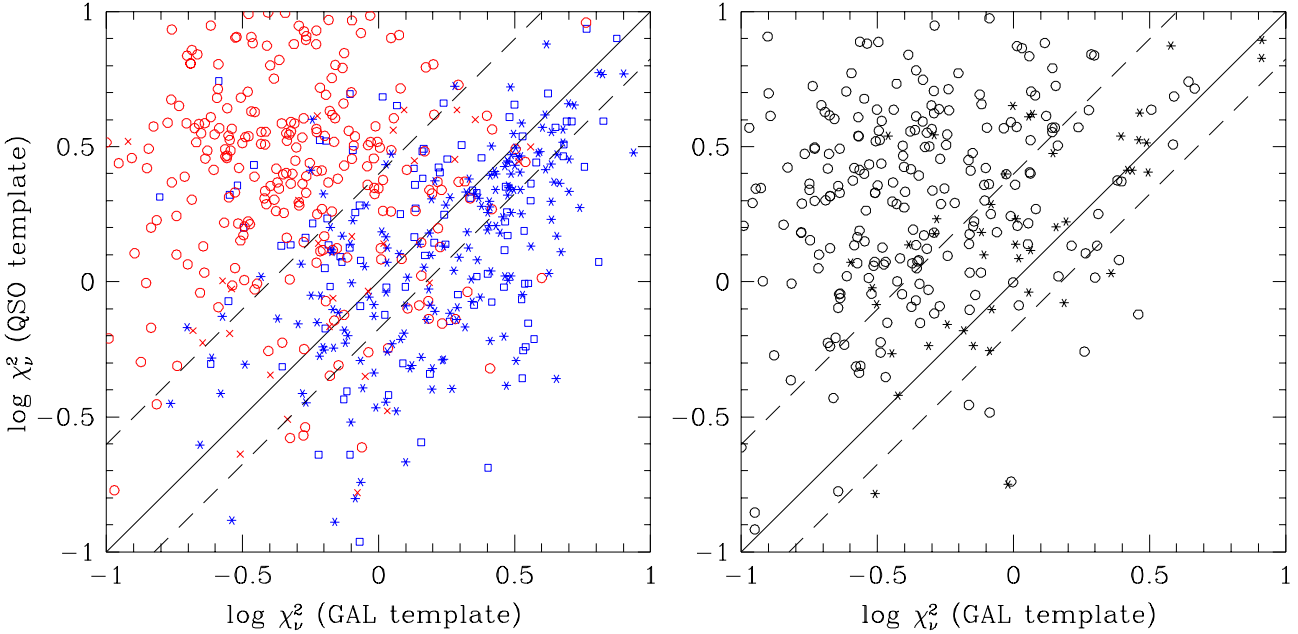


**Fig. 11.** Left) Reduced  $\chi^2$  values of fitting results with QSO- and galaxy-templates for the spectroscopically-identified sample. Blue (square and asterisk) and red (circle and cross) symbols represent broad-line and narrow-line AGNs. Asterisks and crosses are for stellar objects. In order to evaluate the uncertainties in the type determination due to the photometric redshift uncertainties, the redshift is NOT fixed to the spectroscopic redshift during the fitting process. Right) same figure for objects without spectroscopic identification. Circles and asterisks represent non-stellar and stellar objects. In both panels, the solid line shows the equal  $\chi^2_\nu$  line and the upper and lower dashed lines represent the type determination criteria for stellar and non-stellar objects, respectively.

tainty. Narrow-line AGNs (red circles and crosses) on average better fitted with galaxy templates, and broad-line AGNs (blue squares and asterisks) on average better fitted with QSO templates. Crosses and asterisks represent AGNs with stellar morphology. Because the number of the galaxy templates is larger than that of the QSO templates and the average  $\chi^2_\nu$  value for extended narrow-line AGNs with the galaxy templates is smaller than that for stellar broad-line AGNs with QSO-templates, we do not chose the best photometric redshift just by comparing  $\chi^2_{\nu \text{ QSO}}$  and  $\chi^2_{\nu \text{ GAL}}$ , but consider the stellarity as well as the  $\chi^2_\nu$  values. Considering the distribution in the panel, we regard the QSO templates as better if  $\chi^2_{\nu \text{ QSO}}$  is smaller than  $2.5 \times \chi^2_{\nu \text{ GAL}}$  for stellar objects. On the contrary, for extended objects, we regard the GAL-template is better if  $\chi^2_{\nu \text{ GAL}}$  is smaller than  $1.5 \times \chi^2_{\nu \text{ QSO}}$ . These selection criteria are shown with the dashed line in Figure 11.

Based on the comparison, we constrain not only their redshifts but also their AGN types. We classify an object whose photometric redshift is determined with the galaxy (QSO) templates as narrow-line (broad-line) AGN, hereafter. We can examine the reliability of the photometric classification with the template fitting results for the AGNs with spectroscopic classification. As described above, we do not fix their redshifts with spectroscopic redshifts during the fitting process. Among the 302 narrow-line (284 broad-line) AGNs with spectroscopic identification, 267 (206) of them are correctly classified as a narrow-line (broad-line) AGN in the photometric classification. Because less luminous broad-line AGNs have extended morphology, a fraction of them are fitted better with the galaxy templates and photometrically classified as narrow-line AGNs. Their optical continuum can be dominated by the host galaxy component, see Section 7.3. Those mis-classifications lower the rate of correct classification for the broad-line AGNs. If we concentrate on the 180 broad-line AGNs with stellar morphology, 170 are correctly classified as a broad-line AGN in the photometric classification.

The derived photometric redshifts and classification are summarised in Columns 24 and 25 of Table 10, respectively. Column 26 describes flags for the photometric redshift determination: flag=1 means the reduced  $\chi^2$  is larger than 10, flag=2 means photometric redshift is determined with unreliable photometric data for a bright and extended galaxy, and flag=3 means photometric redshift is determined with less than four bands. The number of X-ray AGNs with each flag are summarised in Table 1.

### 6.3. Photometric Redshift Results

The reliability of the photometric redshifts is examined by comparing them with the spectroscopic values. The comparison of the photometric and spectroscopic redshifts of spectroscopically-identified AGNs is shown in Figure 12. We separate the sample into 4 categories using the stellarity and the best-fit template. The difference between the spectroscopic and photometric redshifts is defined as  $dz \equiv (z_{\text{phot}} - z_{\text{spec}})$ , and the bottom part

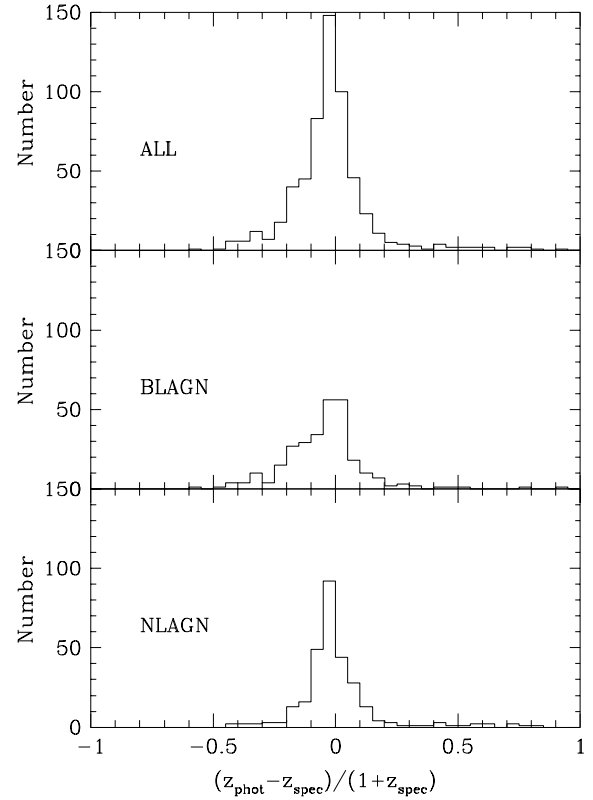


**Fig. 13.** Distribution of  $dz/(1+z_{\text{spec}})$  for all AGNs (top panel), broad-line AGNs (middle), and narrow-line AGNs (bottom).

of the panels show  $dz/(1+z_{\text{spec}})$ . Photometric redshifts for objects that are fitted better with galaxy templates have a small scatter (shown in left panels), but the scatter is larger for objects fitted better with QSO templates (shown in right panels). The distribution of  $dz/(1+z_{\text{spec}})$  is shown in Figure 13. There is no systematic difference between the spectroscopic and photometric redshifts; the median of  $dz/(1+z_{\text{spec}})$  is  $-0.026$  for all the AGNs in the total sample, and  $-0.038$  and  $-0.022$  for broad-line and narrow-line AGNs, respectively. The scatter of the difference is examined with the normalized median absolute deviation (NMAD;  $\sigma_z$ ) following Brammer et al. (2008),

$$\sigma_{\text{NMAD}} = 1.48 \times \text{median} \left( \left| \frac{dz - \text{median}(dz)}{1 + z_{\text{spec}}} \right| \right).$$

$\sigma_{\text{NMAD}}$  corresponds to the standard deviation of a Gaussian distribution, and is less sensitive to the outliers than the usual definition of the standard deviation (Brammer et al. 2008). For the total sample,  $\sigma_{\text{NMAD}}$  is 0.098, which is larger than that of the photometric redshift estimations for X-ray-selected AGNs with medium band filters (Salvato et al. 2009; Cardamone et al. 2010; Luo et al. 2010). For example, Luo et al. (2010) reports  $\sigma_{\text{NMAD}}$  of 0.059 for a blind test sample. Because we do not train the photometric redshift code with SEDs obtained in the spectroscopic redshift sample, our  $\sigma_{\text{NMAD}}$  should be compared with their blind test results. The larger  $\sigma_{\text{NMAD}}$

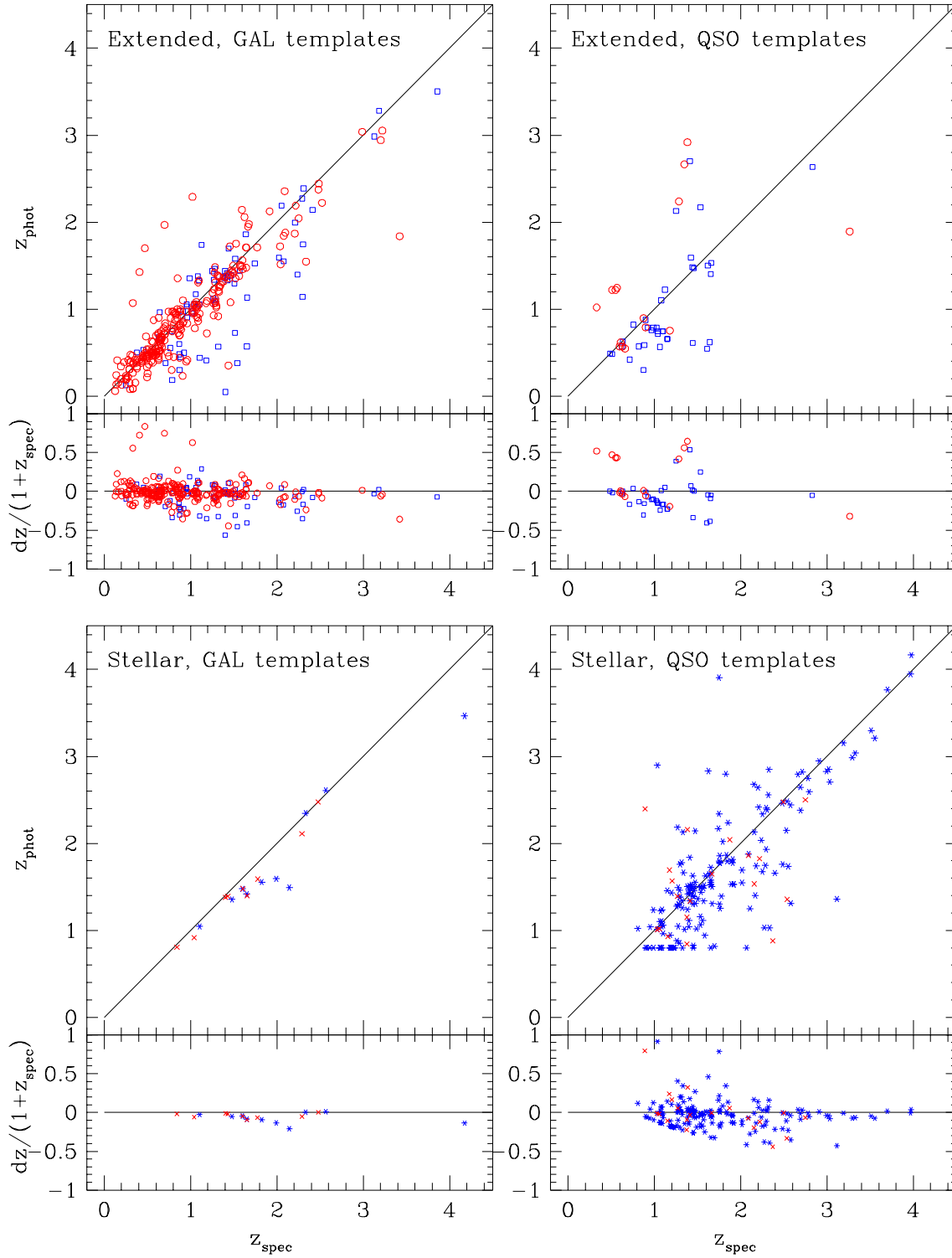


**Fig. 12.** Spectroscopic redshift vs. photometric redshift for objects with spectroscopic identification. Blue squares and crosses and red circles and asterisks represent broad-line and narrow-line AGNs. Top panels show the results for extended objects (squares and circles) and left (right) panel is for objects fitted better with GAL (QSO) template. Bottom panels are same as the upper panels for stellar objects (crosses and asterisks). The upper part of each panel shows spectroscopic redshift vs. photometric redshift and bottom part is  $dz/(1+z_{\text{spec}})$  as a function of  $z_{\text{spec}}$ .



can be explained by the lack of the photometric data with medium band filters. The  $\sigma_{\text{NMAD}}$  for broad-line AGNs (0.109) is larger than that for narrow-line AGNs (0.072), as expected from Figure 13. This is because there is no strong feature in the SEDs of the broad-line AGNs except for the break below  $\text{Ly}\alpha$ . Since the break can only be covered by deep optical observations for AGNs at  $z > 3$ , the discrepancy between  $z_{\text{spec}}$  and  $z_{\text{phot}}$  is smaller for AGNs at  $z > 3$ .

Photometric redshift determination is crucial to understand the nature of the X-ray-selected AGNs. The redshift distribution of the AGN sample is summarised in Figure 14. For narrow-line AGNs, the redshift distribution of spectroscopically-identified objects is different from that of objects without spectroscopic identification: they are located at higher redshifts on average. As shown in the right panel of Figure 10, among the 310 primary candidates without spectroscopic identification, 258 objects have extended morphology. Photometric redshift estimation suggests that they are narrow-line AGNs at  $z \geq 1$ . The green lines in the figure indicate the redshift evolution of the  $i'$ -band magnitude of 10Gyr (solid) and 2Gyr (dashed) single burst stellar population with stellar mass of  $\log M_* = 10.5$  (upper) and  $\log M_* = 12.0$  (lower). The  $i'$ -band magnitudes of most of the spectroscopically-identified narrow-line AGNs are enclosed within the green lines, and the  $i'$ -band magnitudes of narrow-line AGNs with photometric redshifts are also enclosed within the lines.

The photometric redshift results suggest that there are 45 broad-line AGN candidates that have not been spectroscopically identified, and 86% of the broad-line AGNs are thought to be spectroscopically identified. Among broad-line AGN candidates without spectroscopic identification, 7 objects have a photometric redshift above 3, where photometric redshift estimation is reliable even for broad-line AGNs.

## 7. Discussion

### 7.1. X-ray Luminosity and Absorption

In order to examine the physical properties of the X-ray AGNs, at first, we evaluate the intrinsic 2–10 keV luminosity,  $L_{2-10\text{keV}}$  ( $\text{erg s}^{-1}$ ), and the column density of photo-electric absorption to the nucleus,  $N_{\text{H}}$  ( $\text{cm}^{-2}$ ), of each AGN. In order to evaluate  $L_{2-10\text{keV}}$ , it is necessary to correct for the effect of photo-electric absorption using the  $N_{\text{H}}$  value. The number of X-ray photons of each AGN in the current sample is not sufficient to evaluate  $N_{\text{H}}$  for individual AGN accurately with spectral fitting. Thus we estimate  $N_{\text{H}}$  of each AGN from its HR2 value. It needs to be noted that the relation between the HR2 and  $N_{\text{H}}$  is non-linear (Ueda et al. 2008), and the uncertainty associated with  $N_{\text{H}}$  can be large, especially around HR2 of  $\pm 1$ . Furthermore, the relation varies with redshift: at higher redshifts  $N_{\text{H}}$  is steeper function of HR2, and thus the uncertainty is larger than the AGNs at low redshifts with same uncertainty of HR2. Due to these limitations, a statistical analysis, like that applied in Hiroi et

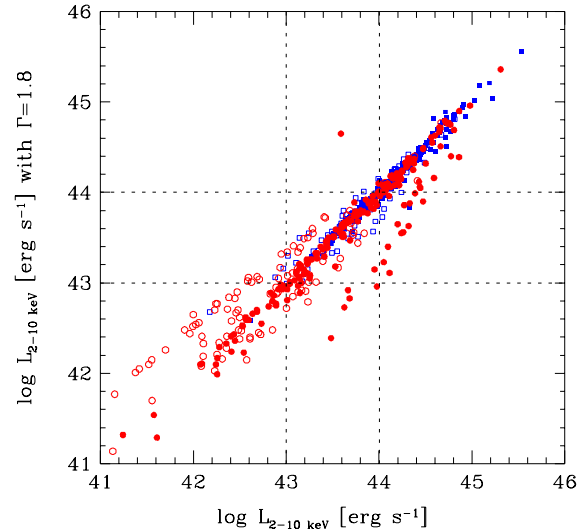


**Fig. 15.** Best-estimated  $L_{2-10\text{keV}}$  vs.  $L_{2-10\text{keV}}$  estimated simply assuming a power-law with  $\Gamma = 1.8$ . Blue squares and red circles represent broad-line and narrow-line AGNs, respectively. Open symbols represent objects that are not detected in the 2–10 keV band and  $L_{2-10\text{keV}}$  is estimated from the 0.5–2 keV count rate.

al. (2012) and Ueda et al. (2008), is necessary to derive the distribution function of  $N_{\text{H}}$  and the hard X-ray luminosity function. Therefore, in this paper, we use  $L_{2-10\text{keV}}$  and  $N_{\text{H}}$  to evaluate average properties of a population of AGNs (Section 7.2) and to construct statistical sample of AGNs sub-divided by their X-ray properties (Section 7.3).

In order to estimate  $N_{\text{H}}$  from HR2, we assume an intrinsic shape of the X-ray spectrum of AGNs following Ueda et al. (2003). The intrinsic X-ray spectrum of AGNs is modeled by a combination of a power-law component with high-energy cut off  $E^{-\Gamma} \times \exp(-E/E_c)$  and a reflection component. A photon index  $\Gamma$  of 1.9 and cutoff energy  $E_c$  of 300 keV are assumed. We calculate the reflection component with the “pexrav” (Magdziarz & Zdziarski 1995) model in the XSPEC package applying a solid angle of  $2\pi$ , an inclination angle of  $\cos i = 0.5$ , and solar abundance of all elements. The strength of the reflection component is about 10% of the direct component just below 7.1 keV. For the assumed intrinsic X-ray spectrum, we ignore any scattered light component and the luminosity dependence of the strength of the reflection component for simplicity. We only consider  $\log N_{\text{H}}$  up to 24.0. For Compton-thick AGNs whose X-ray spectrum is affected by a scattered component,  $N_{\text{H}}$  can be underestimated due to the soft X-ray spectrum of that component. However, the number of such AGNs should be small in the X-ray flux range covered by the current sample (Ueda et al. 2014). If HR2 is smaller than that expected for  $\Gamma = 1.9$ , we determine the corresponding photon index by assuming no absorption. If an object is only detected in the soft-band, we assign  $\Gamma = 1.9$  and we neglect their  $\log N_{\text{H}}$ . For objects only detected in the hard-band, we assign  $\log N_{\text{H}} = 24.0$  and  $\Gamma = 1.9$ .

$L_{2-10\text{keV}}$  is derived from the observed 2–10 keV count-

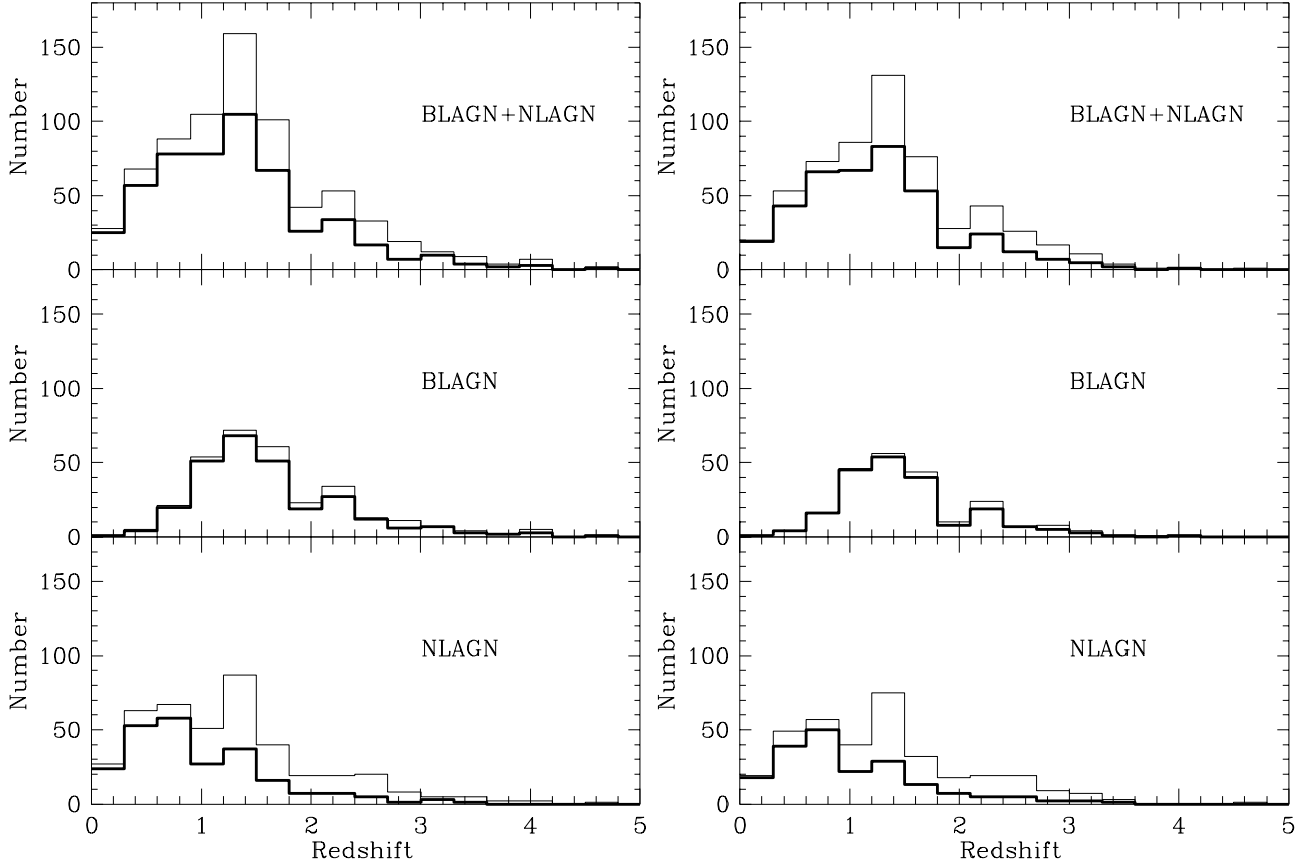


**Fig. 14.** Redshift distributions of the AGNs in the soft-band (hard-band) sample in the left (right) row. The thin solid histogram indicates the redshift distribution of spectroscopic plus photometric redshift samples, the thick solid histogram shows spectroscopic samples only. Shown from top to bottom are the redshift distributions of all X-ray sources, broad-line AGNs, and narrow-line AGNs.

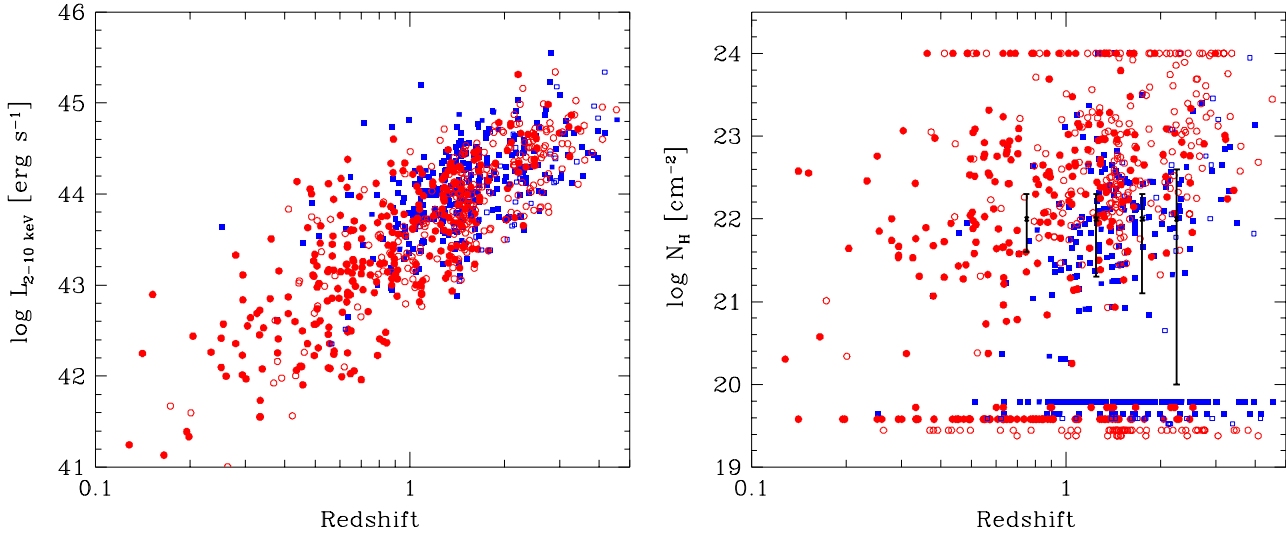


**Fig. 16.** Left) Redshift vs. luminosity of the broad-line (blue squares) and narrow-line AGNs (red circles). Open symbols represent objects with photometric redshift. Right) Redshift vs.  $\log N_{\text{H}}$  ( $\text{cm}^{-2}$ ). Same symbols as in the left panel.  $\log N_{\text{H}}$  is derived from the HR2 value. AGNs only detected in the soft-(hard-)band are plotted below  $\log N_{\text{H}} = 20.0$  (above  $\log N_{\text{H}} = 24.0$ ) with arbitrary shift for clarity. Error bars at  $\log N_{\text{H}} = 22.0$  represent medians of uncertainties for objects with  $\log N_{\text{H}} = 21.5 - 22.5$  at  $z = 0.5 - 1.0$ ,  $1.0 - 1.5$ ,  $1.5 - 2.0$ , and  $2.0 - 2.5$ .

rate assuming the intrinsic spectrum discussed above and correcting for the effect of the photo-electric absorption with the best estimated  $N_{\text{H}}$ . For objects only detected in the 0.5–2 keV band, the count-rate in that band is used instead of the 2–10 keV count-rate to derive  $L_{2-10\text{keV}}$ . The best-estimated  $L_{2-10\text{keV}}$  are compared with  $L_{2-10\text{keV}}$  estimated simply assuming typical apparent power-law spectra of non-absorbed AGNs with  $\Gamma = 1.8$  in Figure 15. We use the count-rate in the 2–10 keV band in the estimation, but for objects only detected in the 0.5–2 keV band, we use the count-rate in the 0.5–2 keV band and show them with open symbols. Because the observed 2–10 keV energy range covers higher energy range in the object rest-frame, for most of the X-ray sources, the amounts of absorption correction are not large. Therefore, the statistical conclusions derived using the best-estimated  $L_{2-10\text{keV}}$  in later sections do not significantly change even if we use the  $L_{2-10\text{keV}}$  derived simply with  $\Gamma = 1.8$ .

The best-estimated  $L_{2-10\text{keV}}$  and  $N_{\text{H}}$  are shown as a function of redshift in the left and right panels of Figure 16. In the right panel, we show the uncertainties of  $\log N_{\text{H}}$  for objects with  $\log N_{\text{H}} = 22.0$ . The uncertainties are determined by medians of uncertainties for objects with  $\log N_{\text{H}} = 21.5 - 22.5$  at  $z = 0.5 - 1.0$ ,  $1.0 - 1.5$ ,  $1.5 - 2.0$ , and  $2.0 - 2.5$ . Uncertainty of each object is determined with the uncertainty of HR2.

The SXDS AGN sample covers wide range of the hard X-ray luminosity, from  $10^{42}$  to  $10^{46}$  erg  $\text{s}^{-1}$ , and encloses the knee of the hard X-ray luminosity function at  $z = 0.4 - 4.0$  ( $\log L_{2-10\text{keV}} \sim 44$  at  $z \leq 1.0$  and  $\log L_{2-10\text{keV}} \sim 44.6$  at  $z \geq 2.0$ ; Ueda et al. 2014). There is an apparent relation between the redshift and luminosity due to the flux limit of the sample.

The distribution of  $N_{\text{H}}$  is broadly consistent with the optical classification on the basis of the existence of broad-emission lines or by SED modeling: broad-line AGNs have smaller  $N_{\text{H}}$  on average. In the redshift range below 0.6, almost all of the AGNs with  $\log N_{\text{H}} < 22$  lack broad-emission lines. For these AGNs, it is likely that the broad-emission line component may be diluted by the host galaxy component. In Table 11, columns 2 and 3 show the redshift and HR2 values assumed to derive the best-estimated  $\log N_{\text{H}}$ ,  $\Gamma$ , and  $\log L_{2-10\text{keV}}$ . Derived values are shown in columns 4-6. — in the column 4 means  $\log N_{\text{H}}$  is not given because HR2 is smaller than expected for a power-law of  $\Gamma=1.9$  or the object is only detected in the soft-band.

## 7.2. Stellar Mass of Narrow-line AGNs and $M_*$ - $L_X$ Relation

We derive the stellar mass of host galaxies of narrow-line AGNs,  $M_*$ , by assuming that their UV to NIR SEDs are dominated by the host galaxy component. The similarity of the SEDs of narrow-line AGNs to those of non X-ray galaxies (e.g. Kiuchi et al. 2009) supports this assumption. The similarity will be discussed further in Section 7.3. We apply SED template fitting with a fixed redshift which is determined either spectroscopically or photometrically, and we use larger number of SED templates than those used in the photometric redshift estimation in or-

der to cover the variety of the SEDs of galaxies accurately. Furthermore, the effect of hot dust component above  $1\mu\text{m}$  wavelength range is considered in the templates as described below.

We construct the SED templates using PEGASE.2 stellar population synthesis code (Fioc & Rocca-Volmerange 1997). A Salpeter IMF with mass range of  $0.1-120 M_{\odot}$  is assumed. SED templates with burst and continuous star formation histories are constructed with a simple exponentially declining star formation rate proportional to  $\exp(-t/\tau)$ .  $t$  represents the age of the stellar system and  $\tau$  represents the decay time scale of the star formation. We use  $\tau$  of 0.5Gyr and 2.0Gyr for burst and continuous models. We use ages of 1.0, 2.0, 2.5, 3.0, 3.5, 4.0, 4.5, 5.0, 6.0, 8.0, and 10.0 Gyrs for the burst model and 0.5, 1.0, 2.0, 3.0, 4.0, 5.0, 6.0, 8.0, and 10.0 Gyrs for the continuous model. We considered three metallicities, 0.5, 1.0, and 2.0 times the solar metallicity. We apply reddening with the Calzetti extinction curve (Calzetti et al. 2000) and consider color excess  $E(B - V)$  with 0.1 mag steps up to 0.9 mag. In addition to the simple exponentially declining and continuous models, we construct templates by combining the two models with a stellar mass ratio of 0.0, 1.0, and 50.0, representing the mixture of the bulge and disk systems of galaxies. In the wavelength range above  $1\mu\text{m}$ , a significant fraction of narrow-line AGNs show an excess compared to the galaxy templates due to hot dust component. In order to reproduce the excess, we construct galaxy templates with an additional power-law component representing the excess above  $1\mu\text{m}$ . Figure 17 shows samples of the SED fitting results for narrow-line AGNs at  $z \sim 1$  in order of the strength of the excess component from the top-left panel with no excess to the bottom-right panel with the strongest excess. The excess components with various strength can be seen above observed wavelength of  $2\mu\text{m}$  are well reproduced with the best-fit templates.

Furthermore, for galaxies at  $z < 0.6$ , the  $8.0\mu\text{m}$  photometry is affected by the  $8\mu\text{m}$  PAH feature, which is not included in the galaxy templates. We do not use  $8.0\mu\text{m}$  photometry for galaxies at  $z < 0.6$ . We do not consider the constraints on the absolute magnitude in the fitting.

The resulting stellar masses of host galaxies of narrow-line AGNs are shown in Figure 18. Although the SXDS sample covers a wide range in luminosity and redshift, the estimated  $M_*$  values are remarkably constant. If we divide the sample into 3 redshift bins with  $0.1 < z < 1.0$  (low),  $1.0 < z < 2.0$  (mid), and  $2.0 < z$  (high), the median  $M_*$  increases by 0.18 dex from the low to the high redshift bins, although the median  $L_{2-10\text{keV}}$  increases by 1.4 dex. The distributions of the  $M_*$  in the 3 redshift bins are compared with each other in Figure 19. The probabilities that a pair of distributions is drawn from the same sample are examined with the Kolmogorov-Smirnov test, and they are 1.0%, 4.7%, and 28% with the low-mid, low-high, and mid-high redshift samples. The mass range of the host galaxies is broadly consistent with those for various X-ray selected samples of narrow-line (e.g., Akiyama 2005; Alonso-Herrero et al. 2008; Kiuchi et al. 2009; Brusa et

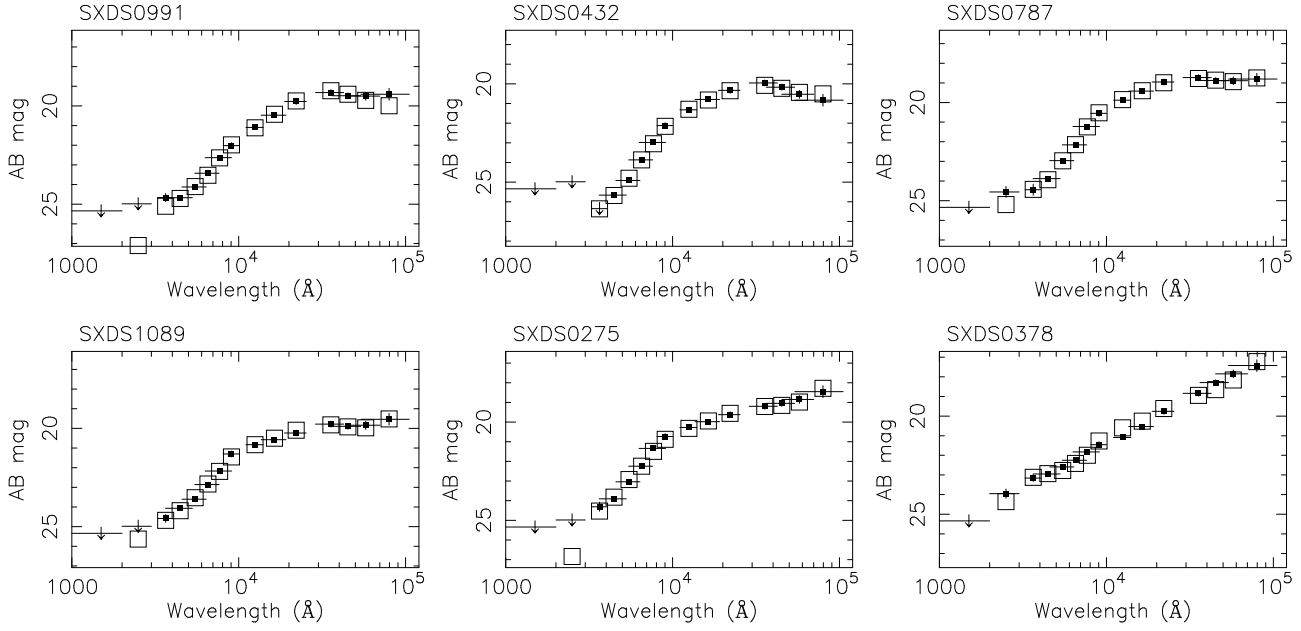


**Fig. 17.** Sample SED fitting results for narrow-line AGNs at  $z \sim 1$  in order of the strength of excess component above  $1 \mu\text{m}$  from top-left to bottom-right panels. Filled squares indicate observed magnitudes at each observed wavelength and arrows show upper limits. Open squares represent magnitudes of the best-fit SED model.

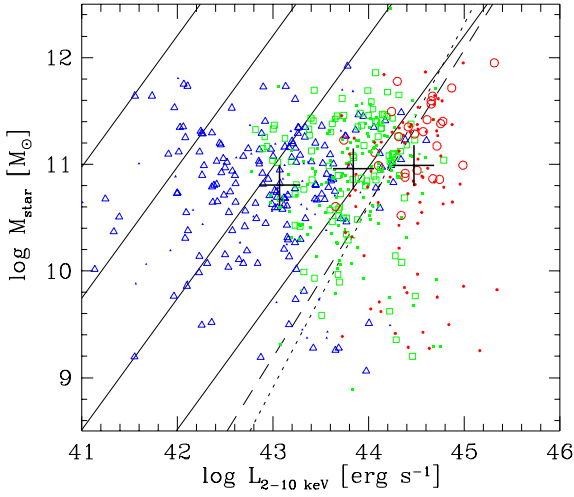


**Fig. 18.** Estimated stellar mass vs 2–10 keV luminosity for narrow-line AGNs. Symbols are coded with redshift; blue triangles are for  $z = 0.1 - 1.0$ , green squares are for  $z = 1.0 - 2.0$ , and red circles are for  $z > 2.0$ . Spectroscopically identified narrow-line AGNs are plotted with large open symbols, and photometric narrow-line AGN candidates are plotted with small filled symbols. Photometric candidates with phot- $z$  flags of 0 or 1 are plotted. Big crosses indicate the median values in the three redshift ranges. Solid lines indicate the stellar mass and 2–10 keV luminosity relation assuming the  $M_{\text{BH}}-M_*$  relation from Bennert et al. (2011) and bolometric correction of Marconi et al. (2004). From bottom to top, an Eddington ratio of 1, 0.1, 0.01, and 0.001 are assumed. Dotted and dashed lines indicate the relations derived with the  $M_{\text{BH}}-M_{*,\text{bulge}}$  relations of Sani et al. (2011) and Marconi & Hunt (2003), respectively, for an Eddington ratio of 1.

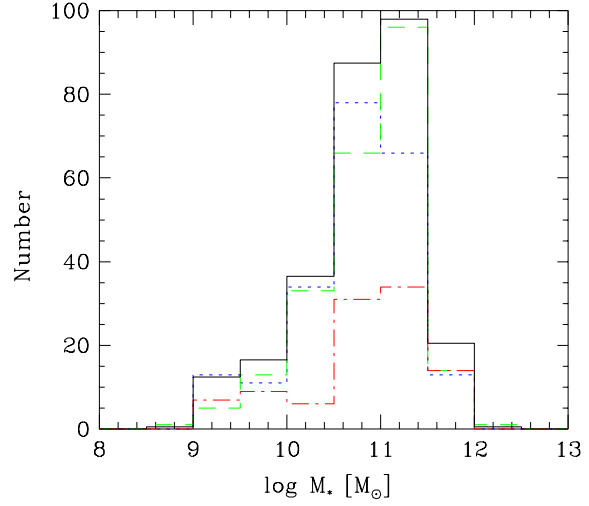


**Fig. 19.** Distribution of  $M_*$  for narrow-line AGNs. The solid histogram is for the entire sample, and blue dotted, green dashed, and red dot-dashed histograms represent the distribution of  $0.1 < z < 1.0$ ,  $1.0 < z < 2.0$ , and  $2.0 < z$  narrow-line AGNs, respectively. The numbers for the entire sample are divided by 2 for clarity.

al. 2009; Yamada et al. 2009; Xue et al. 2010; Mainieri et al. 2011; Rosario et al. 2013) and broad-line AGNs (e.g., Jahnke et al. 2009; Merloni et al. 2010; Bongiorno et al. 2014) at redshifts up to 4. It needs to be noted that we consider the absolute magnitude range of the galaxy template in the photometric redshift determination. The absolute magnitude range can affect the distribution of  $M_*$  of narrow-line AGNs without spectroscopic redshifts, however, only 15 out of the 259 narrow-line AGNs with-



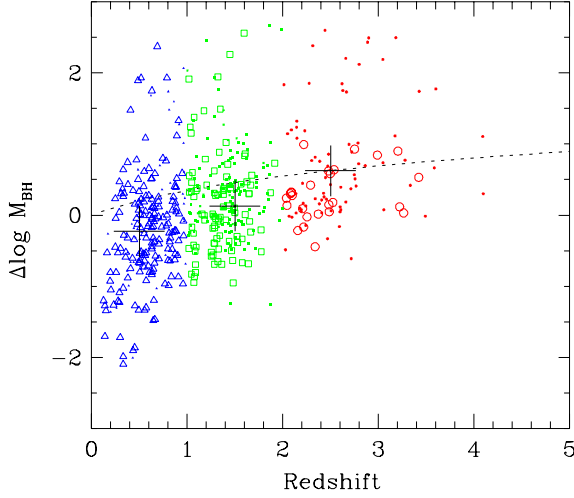


**Fig. 20.** Difference between  $M_{\text{BH}}$  derived from  $L_{2-10\text{keV}}$  and  $\lambda_{\text{Edd}}-L_{\text{bol}}$  relation (Nobuta et al. 2012) and  $M_{\text{BH}}$  derived from  $M_*$  and local  $M_{\text{BH}}-M_*$  relation (Bennert et al. 2011). Symbols are coded with redshift; blue triangles are for  $z = 0.1 - 1.0$ , green squares are for  $z = 1.0 - 2.0$ , and red circles are for  $z > 2.0$ . Spectroscopically identified narrow-line AGNs are plotted with large open symbols, and photometric narrow-line AGN candidates are plotted with small filled symbols. Photometric candidates with phot- $z$  flags of 0 or 1 are plotted. Big crosses indicate the median values in the three redshift ranges. Dotted line indicate the redshift dependence of the difference with cosmological evolution of the  $M_{\text{BH}}-M_*$  relation with  $(1+z)^{1.15}$  (Bennert et al. 2011).

out spectroscopic redshifts are significantly affected by the faint limit of the range and have absolute magnitude close to the limit. Some narrow-line AGNs have  $M_*$  less than  $10^{10} M_{\odot}$ . Their stellar mass estimation would be affected by scattered nuclear light in the UV. Such contamination with a blue continuum possibly makes the SED appear similar to a younger stellar population with a smaller mass-to-light ratio, and the estimated stellar mass can thus appear smaller even with the rest-frame NIR photometry constraints.

The solid lines in Figure 18 indicate the relationship between the stellar mass and X-ray luminosity if we assume the local black hole and host-galaxy stellar mass,  $M_{\text{BH}}-M_*$ , relation from Bennert et al. (2011) and the AGN bolometric correction for 2–10 keV X-ray luminosity from Marconi et al. (2004). The lines from bottom to top correspond to an Eddington ratio of 1, 0.1, 0.01, and 0.001. Bennert et al. (2011) derive the relationship for broad-line AGNs following Häring & Rix (2004) with a Chabrier IMF (Chabrier 2002). We convert their relation to that with the Salpeter IMF, considering that  $M_*$  is 0.255 dex heavier with the Salpeter IMF. We also plot the  $M_*$  and  $L_{2-10\text{keV}}$  relation based on the black hole and bulge stellar mass,  $M_{\text{BH}}-M_{*,\text{bulge}}$ , relations from Sani et al. (2011) and Marconi & Hunt (2003) with dotted and dashed lines, respectively. They are consistent with the relation derived with  $M_{\text{BH}}-M_*$  relation of Bennert et al. (2011) around  $M_* = 10^{12} M_{\odot}$ , and they show steeper dependence on  $L_{2-10\text{keV}}$  than the relation. The difference

below  $M_* = 10^{12} M_{\odot}$  can be explained with the difference between  $M_*$  and  $M_{*,\text{bulge}}$ . The constant  $M_*$  of narrow-line AGNs with wide luminosity and redshift ranges implies higher  $\lambda_{\text{Edd}}$  in the higher redshift bins; significant fraction of narrow-line AGNs at  $z > 2$  possibly have  $L_{2-10\text{keV}}$  close to or above the Eddington limit.

On the other hand, the distribution of narrow-line AGNs on the  $M_*-L_{2-10\text{keV}}$  plane can be explained with the cosmological evolution of the  $M_{\text{BH}}-M_*$  relationship with higher  $M_{\text{BH}}/M_*$  at higher redshifts (e.g., McLure et al. 2006; Peng et al. 2006; Decarli et al. 2010; Bennert et al. 2011; Schramm & Silverman 2013), and  $\lambda_{\text{Edd}}$  for the narrow-line AGNs at high-redshifts may be overestimated. Assuming that the  $\lambda_{\text{Edd}}$  and  $L_{\text{bol}}$  relation that is derived with broad-line AGNs at  $0.5 < z < 2.3$  in the same SXDS X-ray sample (Eq.(16) of Nobuta et al. (2012)) is applicable to the narrow-line AGNs, we estimate  $M_{\text{BH},L}$  of the narrow-line AGNs from  $L_{2-10\text{keV}}$  and the bolometric correction of Marconi et al. (2004). Figure 20 shows the difference between the estimated  $M_{\text{BH},L}$  and the  $M_{\text{BH},M_*}$ , which is calculated from  $M_*$  and the local  $M_{\text{BH}}-M_*$  relationship from Bennert et al. (2011). The difference implies the cosmological evolution of the  $M_{\text{BH}}-M_*$  relationship with larger  $M_{\text{BH}}$  compared to  $M_*$  at higher redshifts can explain the observed distribution on the  $M_*-L_{2-10\text{keV}}$  plane: the  $0.1 < z < 1.0$  narrow-line AGNs have  $-0.23$  dex smaller  $M_{\text{BH}}$  than that expected from  $M_*$ , and the  $z > 2.0$  narrow-line AGNs have  $0.63$  dex larger  $M_{\text{BH}}$ . If we simply fit the distribution, cosmological evolution of  $M_{\text{BH}}-M_*$  relationship with  $(1+z)^{2.6}$  is required. If we take at face value, the derived cosmological evolution of  $M_{\text{BH}}-M_*$  relation is stronger than that in Bennert et al. (2011) shown with dotted line in the figure. In order to derive the cosmological evolution of  $M_{\text{BH}}-M_*$  relationship reliably, we need to consider the bias associated with the luminosity-limited sample (Schulze & Wisotzki 2014). Such detailed analysis is beyond the scope of this paper, and will be discussed somewhere else.

### 7.3. SEDs of X-ray Selected AGNs

Utilising the multi-wavelength photometric data of the large sample of X-ray selected AGNs, we examine the scatter of their UV-MIR SEDs as a function of  $L_{2-10\text{keV}}$  and  $N_{\text{H}}$ , and compare the range of the scatter with that of galaxies without X-ray AGN activity. We choose galaxies which have the same mass and redshift distributions as the X-ray AGNs. Because X-ray AGNs only appear among massive galaxies, it is important to compare the properties of AGNs with those of galaxies without X-ray AGN activity in the same mass range (Silverman et al. 2009; Xue et al. 2010).

We construct a sample of galaxies without X-ray AGN activity in the overlapping region of the deep Suprimecam optical and UDS NIR imaging data. As a first step the photometric redshift is determined with the FUV to MIR photometric data for each object in the same way as for the X-ray AGNs as described in Section 6. We do not apply a QSO template to the galaxies and do not consider the constraints on the absolute magnitude.

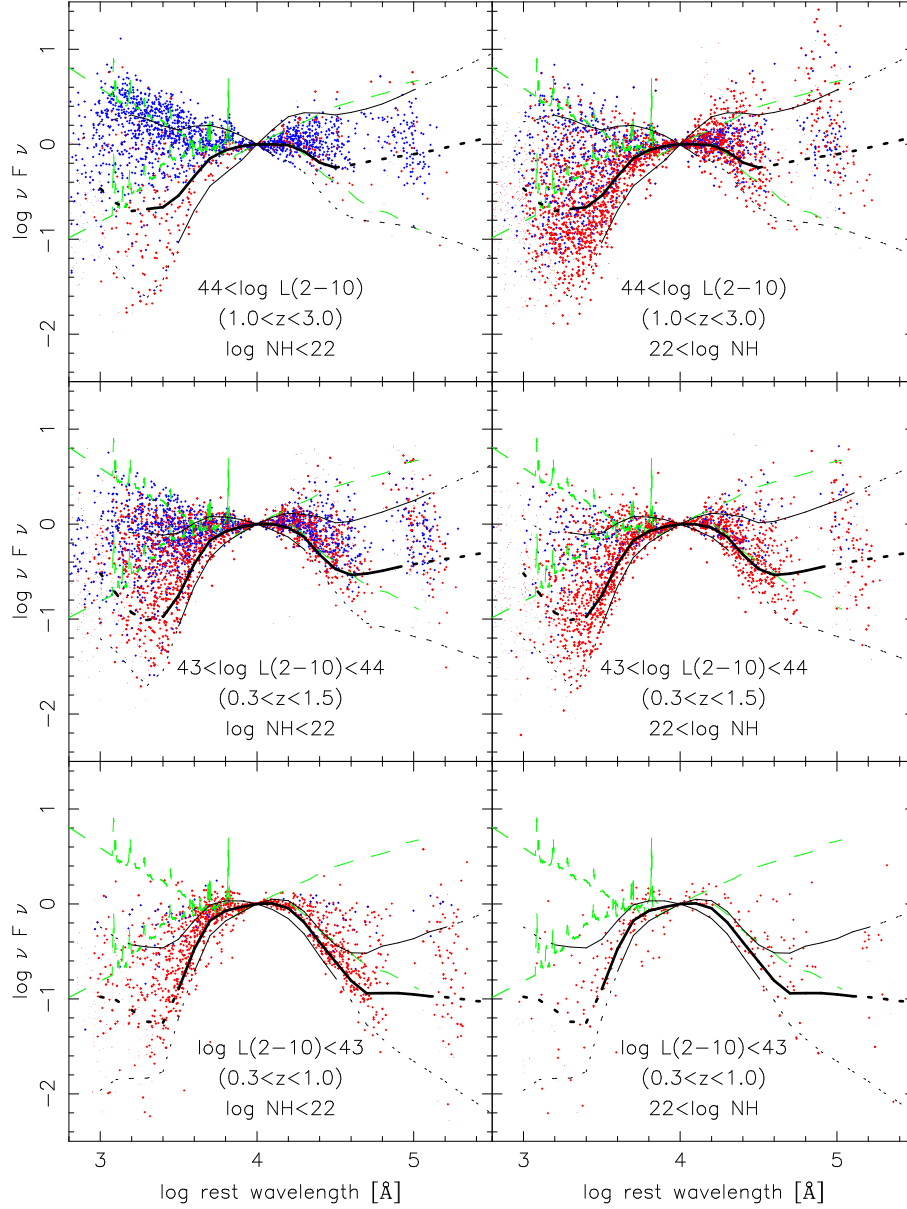


**Fig. 21.** Rest-frame UV to MIR SEDs of X-ray AGNs. All SEDs are normalized at  $1\mu\text{m}$  in the rest-frame. Broad-line and narrow-line AGNs are plotted with blue and red symbols, respectively. Small dots indicate upper limits. The thick black solid and dotted lines represent the median (50%-ile) SED of galaxies in the matched sample for each luminosity bin. Dotted parts represent upper limits, i.e. less than 50% of the galaxies are detected in the wavelength range. Thin black solid and dotted lines show the 10%-ile (upper) and 90%-ile (lower) SED of the galaxies, and dotted lines represent upper limits. Green dashed lines indicate the range of the template QSO SEDs used in the photometric redshift determination. The X-ray AGN sample is subdivided by X-ray luminosity and  $\log N_{\text{H}}$ ; from top to bottom, panels for AGNs with  $44.0 < \log L_{2-10\text{keV}}$ ,  $43.0 < \log L_{2-10\text{keV}} < 44.0$ , and  $\log L_{2-10\text{keV}} < 43.0$ , and from left to right,  $\log N_{\text{H}} < 22.0$  and  $22.0 < \log N_{\text{H}}$ . The typical redshift range of each AGN sample is indicated in parentheses.

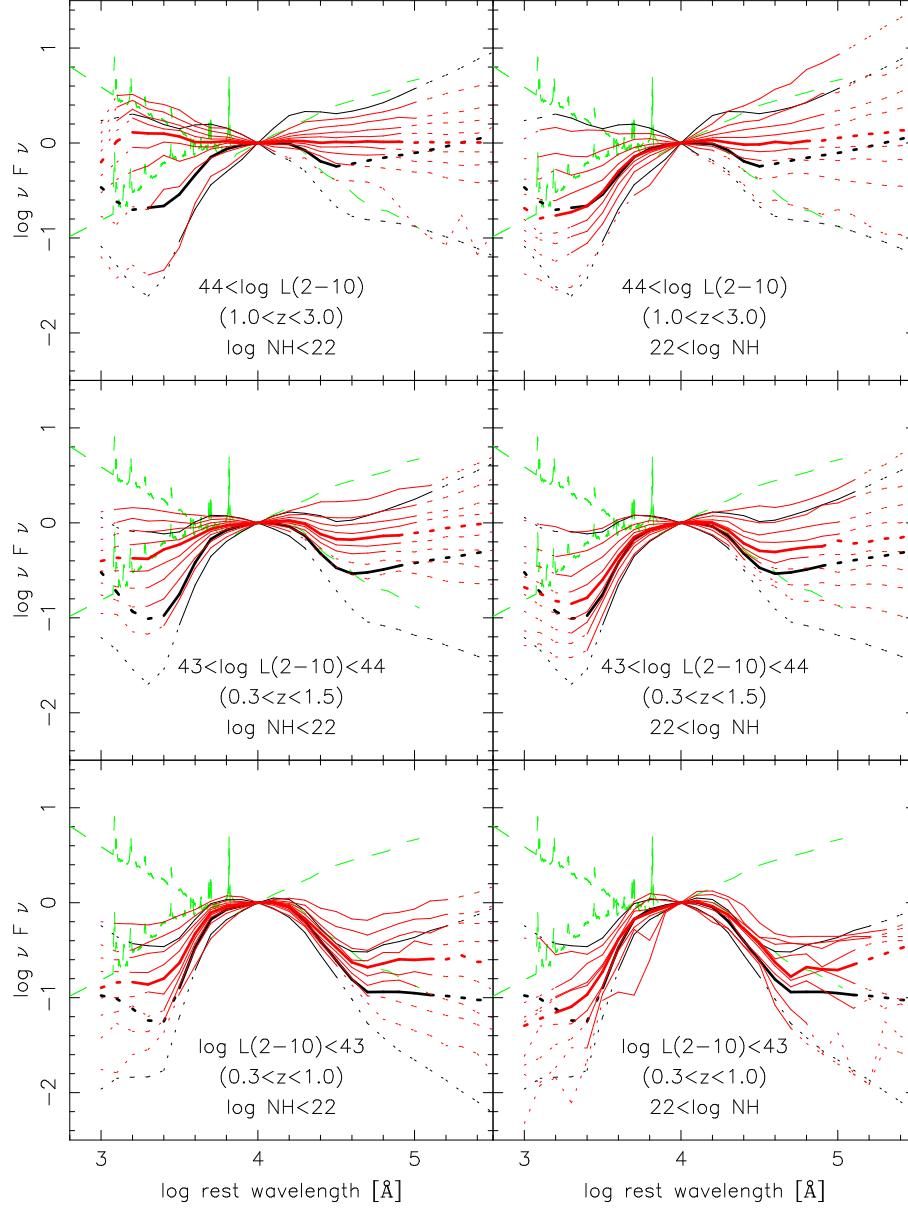


**Fig. 22.** Rest-frame UV to MIR percentile SEDs of X-ray AGNs (red lines). All SEDs are normalized at  $1\mu\text{m}$  in the rest-frame. From top to bottom, 10%-ile to 90%-ile SEDs are shown with 10% interval. Thick solid and dotted lines indicate the median (50%-ile) SED. Dotted lines represent upper limits. The thick black solid and dotted lines represent median SEDs of the galaxies in the matched sample for each luminosity bin. The thin black solid and dotted lines show 10%-ile and 90%-ile SEDs. Dotted parts indicate upper limits. Green dashed lines indicate the range of the template QSO SEDs used in the photometric redshift determination. The X-ray AGN sample is subdivided in the same way as in Figure 21.

Once photometric redshifts are determined, we evaluate the stellar masses of the galaxies applying the model described in Section 7.2. In order to construct the sample of galaxies without X-ray activity, we select galaxies that have similar stellar mass and redshift distribution of the X-ray AGNs. For each X-ray AGN, we select galaxies without X-ray detection within  $dz = \pm 0.2$  of the redshift of the AGN. We assume broad-line AGNs follow the same host galaxy stellar mass distribution shown in Figure 19. Within the redshift range, we randomly select 14 galaxies for each AGN following the mass distribution of 1 in the range  $9.5 < \log M_* < 10.0$ , 2 in the range  $10.0 < \log M_* < 10.5$ , 5 in the range  $10.5 < \log M_* < 11.0$ , 5 in the range  $11.0 < \log M_* < 11.5$ , and 1 in the range  $11.5 < \log M_* < 12.0$ . The mass distribution roughly reproduces that of the total sample of the narrow-line AGNs. In the redshift range between 1.0 and 2.0, there are 12248 ( $9.5 < \log M_* < 10.0$ ), 9140 ( $10.0 < \log M_* < 10.5$ ), 5899 ( $10.5 < \log M_* < 11.0$ ), 2557 ( $11.0 < \log M_* < 11.5$ ), and 310 ( $11.5 < \log M_* < 12.0$ ) galaxies that are not detected in X-ray in the mass range shown in the parenthesis. We allow overlap in the selection, and a galaxy can be selected multiple times. We refer to this sample of galaxies as the matched sample, hereafter.

The SEDs of X-ray AGNs are shown with dots in Figure 21. From top to bottom, the sample is subdivided by X-ray luminosity:  $44.0 < \log L_{2-10\text{keV}}$ ,  $43.0 < \log L_{2-10\text{keV}} < 44.0$ , and  $\log L_{2-10\text{keV}} < 43.0$ , and from left to right, the sample is subdivided by X-ray absorption to the nucleus:  $\log N_{\text{H}} < 22.0$  and  $22.0 < \log N_{\text{H}}$ . Blue and red symbols represent broad- and narrow-line AGNs, respectively. All of the SEDs are normalized at  $1\mu\text{m}$ , and each photometric point is located at its rest-frame effective wavelength. It is clear that the luminous and less-absorbed AGNs show SEDs within the range of the SEDs of the optically-selected QSOs (green dashed lines).

Less-luminous or absorbed AGNs show redder UV-optical SEDs, which are similar to those of galaxies in the matched sample. The thick black solid and dotted lines in the figure show the median (50%-ile) value of the  $1\mu\text{m}$ -normalized SEDs of the galaxies in the matched sample. We construct the matched sample for each luminosity bin. In order to determine the median value at each wavelength, we linearly interpolate the photometric data points of each galaxy in the  $\log \nu F_\nu - \log \lambda$  plane. In the percentile calculation, we include photometric data points which are upper limits. In the wavelength range where less than 50% of galaxies in the sample are detected, the derived median value is an upper limit, and we plot this with the dotted line. The thin black solid and dotted lines represent 10%-ile and 90%-ile from top to bottom at each wavelength range.

In order to quantitatively compare the range of the SEDs, we also construct the percentile SEDs of X-ray AGNs and show them in Figure 22. The SED of each AGN is interpolated in the same way as for the galaxies, and is normalized at  $1.0\mu\text{m}$ . At each wavelength we derive from brightest 10%-ile to 90%-ile SEDs with 10% interval. If the fraction of detected objects at a certain wavelength

is less than the corresponding percentile, we regard the percentile SED as an upper limit and plot the SED with dotted lines.

At wavelengths below  $1\mu\text{m}$  where the SEDs of broad-line AGNs are dominated by a blue power-law component, most of the broad-line AGNs have bluer SEDs than the galaxies in the matched sample, especially in the upper-left highest luminosity and lowest absorption bin: 80% of the X-ray AGNs have bluer SEDs than the median SED of the galaxies in the matched sample. The almost constant median SED of the most luminous less-absorbed AGNs is consistent with the median pre-host subtraction SEDs of broad-line AGNs derived with the COSMOS dataset (Elvis et al. 2012; Hao et al. 2014). If we compare 90%-ile range of Elvis et al. (2012), the upper envelope is consistent, but the current sample has larger scatter in the lower envelope due to the inclusion of narrow-line AGNs. The SEDs of X-ray AGNs become redder with lower luminosity or higher  $N_{\text{H}}$ . In the lowest luminosity bin, even with the low  $N_{\text{H}}$ , the median SED of the AGNs is similar to that of galaxies in the matched sample. As can be seen in Figure 21, almost all of them are narrow-line AGNs, and they do not show strong broad-emission lines in their observed spectra.

The median SEDs of the absorbed ( $\log N_{\text{H}} > 22.0$ ) X-ray AGNs have similar SEDs to those of the galaxies in the matched sample. For example, the rest-frame  $U - V$  color of the median SED of AGNs with  $\log N_{\text{H}} > 22.0$  and  $43.0 < \log L_{2-10\text{keV}} < 44.0$  is only 0.05 mag bluer than the galaxies in the matched sample. The similarity of the  $U - V$  colors of the AGN host galaxies and the galaxies in the matched sample is consistent with the results obtained in the *Chandra* Deep Fields (Xue et al. 2010), and does not support the distribution of AGN host galaxies in a distinct region of color-magnitude space (e.g., Nandra et al. 2007).

In the wavelength range above  $1\mu\text{m}$ , the SEDs of the AGNs are thought to be dominated by  $\leq 1,000\text{K}$  hot thermal emission from a dusty torus, and are roughly constant on the  $\nu L_\nu$  plane. On the other hand, the SEDs of galaxies without X-ray AGN activity are dominated by the stellar continuum, which shows a  $1.6\mu\text{m}$  bump and continuous decrease at longer wavelengths. PAH  $8\mu\text{m}$  and cold-dust emissions from star-forming regions contribute in the wavelength range longward of  $5\mu\text{m}$ . As can be seen in Figure 21, AGNs with  $44 < \log L_{2-10\text{keV}}$  are distributed around a constant SED above  $1\mu\text{m}$  for both the  $\log N_{\text{H}} < 22.0$  and  $> 22.0$  samples, and the SEDs are consistent with the observed range of broad-line AGNs shown with green dashed lines. For AGNs with lower luminosity, the contribution from the hot dust component decreases and the SEDs are bluer and closer to those of galaxies peaked at around  $1.6\mu\text{m}$ .

The galaxies in the matched sample do not show an excess component above  $1\mu\text{m}$  in the lowest luminosity bin, which samples galaxies in the low redshift range, shown in the bottom panels. On the contrary in the highest luminosity bin, which samples galaxies in the higher redshift range, shown in the top panels, the median SED of



the galaxies in the matched sample show a constant SED in this wavelength range. As a result, even though in the middle and high luminosity ranges more than 70-80% of X-ray AGNs show excess component compared to the median SED of the galaxies in the matched sample, the 10%-ile SEDs of X-ray AGNs are similar to those of the galaxies in the matched sample.

Several AGN selection methods based on the detection of hot thermal emission by multi-band photometric data are proposed with the *Spitzer* (Lacy et al. 2004; Ivison et al. 2004; Stern et al. 2005; Donley et al. 2007; Daddi et al. 2007; Fiore et al. 2008; Donley et al. 2012), *AKARI* (Takagi et al. 2010; Hanami et al. 2012), and *Wide-field Infrared Survey Explorer (WISE)* (Mateos et al. 2012) dataset. The similarity of the SEDs of AGNs with  $\log L_{2-10\text{keV}} > 43$  to those of the galaxies in the matched sample suggests that AGN selection based on detecting  $> 1.6\mu\text{m}$  excess emission above the stellar continuum can be contaminated by galaxies without X-ray AGN activity at  $z > 1$  (e.g. Georgakakis et al. 2010; Alexander et al. 2011; Donley et al. 2012). It needs to be noted that the SEDs above rest-frame  $3\mu\text{m}$  in the current study are based on broad-band photometry only at 8 and  $24\mu\text{m}$ , and detailed continuum structure can be missed.

The constant SEDs of galaxies without X-ray AGN activity at  $z > 1$  can be caused by high star-formation activity associated with massive galaxies whose star-formation activity is strongly affected by dust. The cosmological evolution of the  $M_*$  - star-formation rate relation suggests galaxies with  $\log M_* = 10.5$  at  $z = 1.0$  and  $z = 2.0$  have 7 and 24 times higher star-formation rate than those at  $z = 0.0$  on average (Elbaz et al. 2011). Furthermore, star-formation activity in massive galaxies is strongly affected by dust (Pannella et al. 2014). Donley et al. (2007) show SEDs of IR-excess galaxies can be reproduced with a SED of local star-forming galaxy with additional reddening with  $A_V = 0.8$  mag. A larger contribution from thermal dust emission than for local massive galaxies can explain the constant SEDs of the non-X-ray galaxies at  $z > 1$  (Georgakakis et al. 2010). Such evolution of SEDs of galaxies may affect the discussion of MIR SEDs of torus components of the broad-line AGNs (Lusso et al. 2013).

## 8. Summary

We report the multi-wavelength identification of the X-ray sources found in the SXDS field using deep imaging data covering the wavelength range between Far-UV to Mid-IR. Among the 1045 X-ray sources detected in the 7 FoVs of *XMM-Newton* (Ueda et al. 2008), we consider 945 X-ray sources that are detected above likelihood 7 in either of the soft- or hard-band and covered by the deep Suprime-cam imaging observations. We select a primary counterpart for each X-ray source applying the likelihood ratio method to *R*-band,  $3.6\mu\text{m}$ , Near-UV, and  $24\mu\text{m}$  source catalogs. We also consider the matching catalogs with AGN candidates selected in 1.4GHz radio and *i'*-band variability surveys.

Once candidates of Galactic stars, ULXs in a nearby

galaxy, and clusters of galaxies are removed there are 896 AGN candidates in the sample. We conduct spectroscopic observations of 596 and 851 primary counterparts in the optical and NIR wavelengths, respectively, and spectroscopically identify 65%, 597, of the total sample. For the remaining X-ray AGN candidates, we evaluate their photometric redshift with photometric data in 15 bands. In the photometric redshift determination, we apply SED templates of QSOs and galaxies separately to each primary counterpart, and select the best-fit photometric redshift considering the *i'*-band stellarity.

Utilising the multi-wavelength photometric data of the large sample of X-ray selected AGNs, we examine  $M_*$  of the host galaxies of the narrow-line AGNs. The median  $M_*$  in the three redshift bins,  $0.1 < z < 1.0$ ,  $1.0 < z < 2.0$ , and  $2.0 < z$ , only increases 0.18 dex from the low to the high redshift bins, although the median  $L_{2-10\text{keV}}$  increases 1.4 dex in the redshift range. If we consider the  $M_{\text{BH}}-M_*$  relation in the local Universe, the constant  $M_*$  implies higher  $\lambda_{\text{Edd}}$  for luminous AGNs at high redshifts. On the other hand, if we assume the  $\lambda_{\text{Edd}}$  and  $L_{\text{bol}}$  relation derived for broad-line AGNs, we can estimate  $M_{\text{BH}}$  of the narrow-line AGNs. The constant  $M_*$  can also be explained with strong redshift evolution of  $M_{\text{BH}}-M_*$  relation from that determined in the local Universe.

Finally, the scatter of the rest-frame UV-MIR SEDs of X-ray AGNs is examined as a function of  $L_{2-10\text{keV}}$  and  $N_{\text{H}}$ . The scatter is compared with the scatter of the SEDs of the galaxies without X-ray detection. The comparison sample of galaxies are selected to have redshift and  $M_*$  distributions matched to the X-ray AGNs. The UV-NIR SEDs of X-ray AGNs with  $\log N_{\text{H}} > 22.0$  are remarkably similar to those of the galaxies in the matched sample. In the NIR-MIR wavelength range, the median SEDs of X-ray AGNs are redder than those of the galaxies in the matched sample, and luminous AGNs show constant median SED in the wavelength range, suggesting the existence of the hot dust component. However, the scatter of the SEDs of the luminous X-ray AGNs broadly overlap with that of the galaxies in the matched sample. The galaxies in the matched sample of the luminous AGNs also show a more constant SED than the galaxies in the matched sample of the less-luminous AGNs, which are at lower redshifts than the luminous AGNs on average. A higher star-formation rate in massive galaxies at  $z = 1 - 3$  can explain the constant SED of the galaxies in the matched sample. Due to the similarity of the SEDs of X-ray AGNs to those of the galaxies in the matched sample, it is expected that AGN selection criteria looking for excess in the NIR-MIR wavelength range can be significantly contaminated by non-AGN galaxies.

**Table 1.** X-ray source content of the sample

	N <sub>total</sub>	N <sub>soft</sub>	N <sub>hard</sub>	COMMENT
X-ray sources	1045	866	645	Listed in Ueda et al. (2008)
X-ray sample	945	781	584	within deep Suprime-cam image coverage
Covered by 1.4GHz radio survey	789	655	497	Covered in Simpson et al. (2006)
Clusters of galaxies candidates	14	14	1	See Table 4
Galactic star candidates	31	30	4	See Table 7
ULX candidates	4	4	3	See Section 4.5
AGN candidates	896	733	576	
Observation summary for the 896 AGN candidates				
Optical spec. observed	597	523	399	
NIR spec. observed	851	704	548	
Spec. identified	586	514	397	
Photz flag=1	1	1	0	
Photz flag=2	10	10	7	
Photz flag=3	12	6	7	

**Table 2.** Multiwavelength dataset

Obs./Inst.	Band	Aperture (mag) (3)	Detection Limits Total (mag) (4)	Correction (mag) (5)	NOTE (6)
(1)	(2)	(3)	(4)	(5)	(6)
<i>GALEX</i>	FUV	26.64	25.52(4 $\sigma$ ,0.36)	0.18	Deep Imaging Survey
<i>GALEX</i>	NUV	26.18	25.15(3 $\sigma$ ,0.59)	0.17	Deep Imaging Survey
Subaru/Suprime	<i>U</i>	27.39	26.46(3 $\sigma$ ,0.49)	0.11	South FoV only
CTIO/Mosaic-II	<i>U</i>	26.86	26.29(3 $\sigma$ ,0.13)	0.11	
CFHT/Mega-cam	<i>U</i>	26.65	26.11(3 $\sigma$ ,0.10)	0.11	CFHTLS wide
INT/WFCam	<i>U</i>			0.11	Only used for bright objects
Subaru/Suprime	<i>B</i>	28.50-28.83	27.91-28.24(3 $\sigma$ ,0.15)	0.09	
INT/WFCam	<i>G</i>				Only used for bright objects
Subaru/Suprime	<i>V</i>	28.09-28.22	27.55-27.68(3 $\sigma$ ,0.10)	0.07	
Subaru/Suprime	<i>R</i>	27.95-28.18	27.38-27.61(3 $\sigma$ ,0.13)	0.07	
INT/WFCam	<i>R</i>				Only used for bright objects.
Subaru/Suprime	<i>i'</i>	27.91-28.10	27.30-27.49(3 $\sigma$ ,0.17)	0.06	
INT/WFCam	<i>i'</i>				Only used for bright objects.
Subaru/Suprime	<i>z'</i>	26.83-27.08	26.25-26.50(3 $\sigma$ ,0.14)	0.04	
INT/WFCam	<i>z'</i>				Only used for bright objects.
UKIRT/WFCAM	<i>J</i>	26.06	25.40(3 $\sigma$ ,0.22)	0.02	UKIDSS/UDS-DR8
UKIRT/WFCAM	<i>H</i>	25.48	24.82(3 $\sigma$ ,0.22)	0.02	UKIDSS/UDS-DR8
UKIRT/WFCAM	<i>K</i>	25.96	25.30(3 $\sigma$ ,0.22)	0.01	UKIDSS/UDS-DR8
<i>Spitzer</i> /IRAC	3.6 $\mu$ m	23.54	22.77(3 $\sigma$ ,0.33)	0.01	SWIRE
<i>Spitzer</i> /IRAC	3.6 $\mu$ m	25.26	24.49(3 $\sigma$ ,0.33)	0.01	SpUDS
<i>Spitzer</i> /IRAC	4.5 $\mu$ m	22.87	22.07(3 $\sigma$ ,0.36)	0.00	SWIRE
<i>Spitzer</i> /IRAC	4.5 $\mu$ m	24.83	24.03(3 $\sigma$ ,0.36)	0.00	SpUDS
<i>Spitzer</i> /IRAC	5.8 $\mu$ m	21.27	19.97(4 $\sigma$ ,0.54)	0.00	SWIRE
<i>Spitzer</i> /IRAC	5.8 $\mu$ m	22.99	21.69(4 $\sigma$ ,0.54)	0.00	SpUDS
<i>Spitzer</i> /IRAC	8.0 $\mu$ m	21.17	19.91(4 $\sigma$ ,0.66)	0.00	SWIRE
<i>Spitzer</i> /IRAC	8.0 $\mu$ m	23.19	21.77(4 $\sigma$ ,0.66)	0.00	SpUDS
<i>Spitzer</i> /MIPS	24 $\mu$ m	20.21	18.22(4 $\sigma$ ,1.23)	0.00	SWIRE
<i>Spitzer</i> /MIPS	24 $\mu$ m	22.06	20.07(4 $\sigma$ ,1.23)	0.00	SpUDS

Notes. Column (3) is 2  $\sigma$  aperture magnitude limit measured in a fixed aperture. The diameters of the apertures are 7''6 for *GALEX* FUV and NUV images, 2''0 for U-band, optical, and NIR images, 3''8 for IRAC images, and 6''0 for MIPS images. Column (4) gives the 3 $\sigma$  limits for the total magnitudes, for *GALEX* FUV and for *Spitzer* MIPS data the 4 $\sigma$  magnitude limits. They are determined from the aperture magnitude limit and the aperture correction for stellar objects. These upper limits are used in the photometric redshift determination and in Table 8. Applied aperture corrections are shown in the right side in the parenthesis. Column (5) is the correction for Galactic extinction.

**Table 3.** Identification of the X-ray sources

ID	X-ray		ERR (")	ML2	ML34	Primary Flag				Matching		Counterpart	
	RA	Dec.				O	U	I	M	R	V	RA	Dec.
(1)	(2)	(3)	(4)	(5)	(6)	(7)	(8)	(9)	(10)	(11)	(12)	(13)	(14)
SXDS0001	02:15:24.9	−04:55:43.3	2.40	19.9	5.1	1	1	1	1	0	0	02:15:24.9	−04:55:41.2
SXDS0002	02:15:24.9	−04:54:07.9	2.20	33.7	6.2	1	1	1	0	0	0	02:15:24.9	−04:54:07.8
SXDS0003	02:15:27.2	−05:02:00.7	2.90	0.0	7.5	0	1	0	0	0	0	02:15:26.9	−05:02:04.3
SXDS0004	02:15:29.0	−04:57:46.5	3.00	14.1	0.0	1	1	1	0	0	0	02:15:28.9	−04:57:47.1
SXDS0005	02:15:29.4	−04:53:27.5	1.90	11.8	8.6	1	0	1	1	0	1	02:15:29.3	−04:53:25.2
SXDS0008	02:15:37.1	−04:56:56.5	1.20	41.6	5.9	1	1	1	0	0	1	02:15:37.1	−04:56:57.2
SXDS0010	02:15:38.8	−05:00:52.2	1.30	72.1	11.0	1	1	1	1	0	0	02:15:38.7	−05:00:50.3
SXDS0012	02:15:41.6	−05:04:13.5	2.40	7.4	8.3	−1	0	−1	0	0	0	02:15:41.6	−05:04:11.0
SXDS0015	02:15:43.9	−05:07:15.8	0.30	830.0	150.0	1	1	0	0	0	0	02:15:43.9	−05:07:16.3
SXDS0016	02:15:44.0	−04:55:25.8	2.30	11.7	4.4	−1	0	−1	0	0	0	02:15:44.0	−04:55:22.2

Notes. Column (1) is the X-ray name. Columns (2) and (3) are the X-ray coordinates. Column (4) is  $\sigma_{X_i}$  from Ueda et al. (2008). Column (5) and (6) are the maximum likelihoods in the 0.5–2 keV and 2–10 keV bands. Column (7)–(10) show whether the primary counterpart is selected as the primary candidate in *R*-band (col.(7)), *GALEX* NUV band (col.(8)), *Spitzer* 3.6 $\mu$ m (col.(9)), and *Spitzer* 24 $\mu$ m (col.(10)) identifications. 1 means the object is selected as the primary candidate of the identification in the band. −1 means the object is selected as the primary candidate, but the likelihood is less than 1.0. Columns (11) and (12) indicate the primary counterpart is selected as counterpart of 1.4GHz radio source and variability AGN candidate, respectively. Columns (13) and (14) are coordinates of the primary counterpart. (This table is available in its entirety in a machine-readable form in the online journal. A portion is shown here for guidance regarding its form and content.)



**Table 4.** Candidate clusters of galaxies

ID (1)	HR2 (2)	$z_{\text{spec}}$ (3)	$z_{\text{phot}}$ (4)	NOTE (5)
SXDS0047	−0.79	9.99	1.00	
SXDS0280	−0.95	9.99	0.45	SXDF79XGG
SXDS0295	−0.53	9.99	0.60	
SXDS0434	−0.44	9.99	0.62	
SXDS0453	−1.00	0.20	0.20	SXDF16XGG
SXDS0514	−0.54	0.65	0.65	SXDF69XGG
SXDS0552	−0.82	0.52	0.52	SXDF34XGG, Radio
SXDS0621	−0.98	0.69	0.69	SXDF04XGG, SXDF85XGG, Radio
SXDS0647	−0.64	9.99	0.46	SXDF35XGG
SXDS0829	−0.82	0.87	0.88	SXDF46XGG
SXDS0876	−0.53	0.38	0.38	SXDF01XCG
SXDS0889	−0.70	0.20	0.38	SXDF01XCG
SXDS0913	−0.88	9.99	0.47	
SXDS1176	−0.74	0.33	0.33	SXDF36XGG

Notes. Column (1) is the X-ray source name. Column (2) is HR2. Sources only detected in the soft-band are indicated with HR2 of −1.00. Column (3) is spectroscopic redshift: 9.99 means no spectroscopic redshift is available. Column (4) is photometric redshift. Column (5) describes the corresponding name in Finoguenov et al. (2010).

**Table 5.** Journal of FOCAS/Subaru Observations

Mask Name	FoV Center		Period	Exptime	Grism	Filter	$\lambda$ Coverage	Note
	RA	Dec.		(s)			(Å)	
(1)	(2)	(3)	(4)	(5)	(6)	(7)	(8)	(9)
150A_20	02:17:57.60	−05:02:25.1	2001/01	5400	150	SY47	4700 9400	
150A_21	02:17:39.00	−05:01:35.4	2001/11	7200	150	SY47	4700 9400	
150A_22	02:18:28.80	−05:00:32.4	2001/11	5400	150	SY47	4700 9400	
150A_23	02:18:21.10	−05:05:27.0	2001/11	1800	150	SY47	4700 9400	
150A_01	02:17:09.67	−05:13:17.9	2003/10	7200	150	SY47	4700 9400	
150A_02	02:19:40.20	−04:50:54.5	2003/12	3600	150	SY47	4700 9400	
150A_03	02:17:16.41	−04:58:49.6	2003/10	7200	150	SY47	4700 9400	
150A_04	02:19:23.44	−05:05:26.8	2003/12	3600	150	SY47	4700 9400	
150A_05	02:16:54.54	−04:48:08.3	2003/12	3600	150	SY47	4700 9400	
150A_06	02:17:23.92	−05:28:55.2	2003/12	3600	150	SY47	4700 9400	
150A_07	02:19:31.70	−04:58:42.6	2003/12	3600	150	SY47	4700 9400	
150A_08	02:20:06.97	−04:56:13.6	2003/12	4800	150	SY47	4700 9400	
150A_09	02:19:23.09	−04:50:37.3	2003/12	3600	150	SY47	4700 9400	
150A_10	02:18:11.78	−05:02:23.2	2003/12	3600	150	SY47	4700 9400	
150A_11	02:17:34.52	−05:17:15.6	2003/12	3600	150	SY47	4700 9400	
150A_12	02:17:59.68	−04:54:43.2	2003/12	4800	150	SY47	4700 9400	
150A_13	02:20:22.53	−05:02:12.1	2003/12	3600	150	SY47	4700 9400	
150A_14	02:19:33.89	−05:14:18.7	2003/12	3600	150	SY47	4700 9400	
150A_15	02:16:18.00	−05:10:32.7	2003/10	5400	150	SY47	4700 9400	
150A_16	02:18:26.74	−04:46:35.3	2003/12	3600	150	SY47	4700 9400	
150A_17	02:17:07.19	−04:44:21.3	2003/12	4800	150	SY47	4700 9400	
150A_18	02:18:38.77	−05:05:14.4	2003/12	5400	150	SY47	4700 9400	
150A_19	02:17:35.15	−05:03:11.8	2003/12	3600	150	SY47	4700 9400	
150B_01	02:18:08.28	−05:01:32.3	2003/12	3600	150	SY47	4700 9400	
150C_01	02:19:40.70	−05:06:41.3	2003/10	3600	150	SY47	4700 9400	
150C_05	02:17:44.60	−04:51:05.9	2003/10	4800	150	SY47	4700 9400	
150C_07	02:17:20.50	−05:06:19.8	2003/10	6000	150	SY47	4700 9400	
150C_08	02:17:20.80	−05:12:07.8	2003/10	4800	150	SY47	4700 9400	
150C_10	02:16:53.50	−04:57:08.5	2003/10	3600	150	SY47	4700 9400	
300A_10	02:19:01.33	−04:31:07.2	2003/10	7200	300B	SY47	4700 9200	
300C_05	02:17:51.50	−05:29:30.0	2003/12	7200	300B	SY47	4700 9200	
300C_06	02:18:25.92	−05:32:47.3	2003/12	7200	300B	SY47	4700 9200	
300C_07	02:20:22.32	−04:50:23.9	2003/12	7200	300B	SY47	4700 9200	
300E_01	02:18:09.35	−05:03:03.2	2004/10	14400	300B	NONE	3800 9200	
			2004/12	7200	150	SY47	4700 9400	
300E_02	02:17:24.23	−04:53:28.5	2004/10	9000	300B	NONE	3800 9200	
300E_03	02:17:34.08	−05:11:11.7	2004/11	5400	150	SY47	4700 9400	
300E_04	02:17:43.84	−05:08:31.6	2004/11	10800	300B	NONE	3800 9200	
300E_05	02:17:17.19	−05:00:15.3	2004/11	10800	300B	NONE	3800 9200	
300E_06	02:18:12.63	−04:53:22.8	2004/11	10800	300B	NONE	3800 9200	
300E_07	02:18:44.59	−05:00:22.7	2004/11	10800	300B	NONE	3800 9200	
300E_08	02:17:42.10	−04:49:54.6	2004/11	18000	300B	NONE	3800 9200	
300E_09	02:17:57.53	−04:56:47.0	2004/11	9000	300B	NONE	3800 9200	
300G_01	02:17:18.07	−05:08:26.3	2005/11	9000	300B	NONE	3800 9200	
300G_02	02:18:33.27	−05:18:31.1	2005/11	7200	300B	NONE	3800 9200	
300G_04	02:16:28.60	−05:09:35.9	2005/11	10800	300B	NONE	3800 9200	
300G_05	02:16:11.08	−05:10:14.0	2005/11	7200	300B	NONE	3800 9200	
300G_06	02:16:51.87	−04:45:07.1	2005/11	12600	300B	NONE	3800 9200	
300G_08	02:16:51.21	−04:50:36.5	2005/11	16200	300B	NONE	3800 9200	
300G_10	02:19:10.45	−05:12:59.1	2005/11	7200	300B	NONE	3800 9200	
300G_12	02:17:47.25	−04:33:39.3	2005/11	7200	300B	NONE	3800 9200	

Notes. Column (1) is the name of the FoV, and columns (2) and (3) are coordinates of the FoV center. Column (4) is the observation period. Column (5) is the integration time. Column (6) and (7) indicate the name of grism and filter used in the observation. Column (8) shows the typical wavelength coverage.

**Table 6.** Journal of the FMOS/Subaru observations

FoV Name	FoV Center		Period	Exptime	MODE	Note
	RA	Dec.		(s)		
(1)	(2)	(3)	(4)	(5)	(6)	(7)
SXDS00	02:17:32.6	−05:00:34	2009/10	9000	LR	IRS1 only
SXDS01	02:17:18.0	−05:04:19	2009/12	5400	LR	IRS1 only
SXDS02	02:17:32.5	−05:10:50	2009/12	15300	LR	
SXDS03	02:17:45.4	−05:05:23	2010/09	11700	LR	
SXDS05	02:17:32.9	−04:39:00	2010/11	6300	LR	
SXDS06	02:17:43.3	−04:38:20	2010/11	3600	LR	
SXDS07	02:17:40.4	−05:18:17	2010/11	35100	LR	
SXDS08	02:19:26.8	−04:59:37	2010/11	16200	LR	
SXDS09	02:16:35.6	−05:01:44	2010/11	18900	LR	
SXDS10	02:17:39.2	−04:38:25	2010/11	11700	LR	
SXDS11	02:17:41.1	−05:02:24	2010/11	14400	LR	
SXDS12	02:17:59.2	−04:51:00	2010/12	13500	LR	IRS1 only
SXDS13	02:18:26.9	−05:18:03	2010/12	1800	LR	
			2011/02	2700	LR	
			2011/02	1800	LR	
SXDS16	02:16:59.7	−05:00:19	2011/10	10800	LR	
SXDS17	02:17:48.7	−05:15:38	2011/10	19800	LR	
SXDS18	02:18:42.2	−04:38:29	2011/10	18000	LR	
SXDS19	02:17:19.4	−05:21:00	2011/10	18000	LR	
SXDS20	02:19:11.8	−05:07:26	2011/10	18900	LR	
SXDS21	02:17:40.7	−05:01:30	2011/10	17100	LR	
			2011/10	9000	LR	
			2011/11	3600	LR	IRS1 only
			2011/11	5400	LR	
SXDS22	02:16:19.3	−04:58:58	2011/12	9000	LR	
			2011/12	14400	LR	IRS1 only
SXDS23	02:18:52.5	−05:02:11	2011/12	3600	LR	
			2011/12	14400	LR	IRS1 only
SXDS24	02:17:34.0	−05:18:25	2011/12	11700	LR	IRS1 only

Notes. Column (1) Name of the FoV, columns (2) and (3) central coordinates of the FoV, column (4) observation period, column (5) total integration time, column (6) observation mode, and column (7) notes.

**Table 7.** Candidate galactic stars

ID	HR2
(1)	(2)
SXDS0020	−1.00
SXDS0039	−1.00
SXDS0120	−0.98
SXDS0125	−0.93
SXDS0191	−1.00
SXDS0245	−0.90
SXDS0248	−0.82
SXDS0297	−0.99
SXDS0302	−1.00
SXDS0365	+0.32
SXDS0448	−0.67
SXDS0469	−0.74
SXDS0532	−0.94
SXDS0545	−0.90
SXDS0601	−0.93
SXDS0633	−1.00
SXDS0686	−0.63
SXDS0692	−1.00
SXDS0693	−0.96
SXDS0731	−1.00
SXDS0783	−1.00
SXDS0816	−0.92
SXDS0822	−0.98
SXDS0832	−0.80
SXDS0844	−0.97
SXDS0923	−0.92
SXDS0974	−0.91
SXDS0985	−1.00
SXDS0995	−0.99
SXDS1062	−1.00
SXDS1181	−0.98

Notes. Column (1) is the X-ray source name. Column (2) shows HR2. Sources only detected in the soft-band are indicated with HR2 of −1.00.



**Table 8.** Multiwavelength properties of the X-ray AGN candidates I

ID	FUV		NUV		$U$		$B$		$V$		$R$		$i'$		$z'$	
(1)	(mag)	(2)	(mag)	(3)	(mag)	(4)	(mag)	(5)	(mag)	(6)	(mag)	(7)	(mag)	(8)	(mag)	(9)
SXDS0001	23.40	0.07	21.66	0.05	21.13	0.05	20.62	0.01	19.99	0.01	19.30	0.01	19.00	0.01	18.72	0.01
SXDS0002	25.34	99.99	23.36	0.09	22.99	0.06	22.61	0.01	22.17	0.01	21.55	0.01	21.07	0.01	20.83	0.01
SXDS0003	24.39	0.10	23.73	0.10	23.84	0.10	23.39	0.01	22.82	0.01	22.60	0.02	22.66	0.01	22.51	0.02
SXDS0004	23.04	0.05	22.18	0.05	18.98	0.05	20.93	0.01	99.99	99.99	19.21	0.00	17.94	0.00	17.55	0.00
SXDS0005	25.34	99.99	24.98	99.99	25.36	0.26	24.76	0.02	23.91	0.02	22.86	0.02	22.00	0.01	21.20	0.01
SXDS0008	23.09	0.06	22.13	0.06	22.28	0.05	22.43	0.01	21.96	0.01	22.02	0.01	22.04	0.01	21.97	0.01
SXDS0010	22.13	0.05	21.16	0.05	20.94	0.05	20.85	0.01	20.64	0.01	20.56	0.01	20.60	0.01	20.61	0.01
SXDS0012	25.34	99.99	24.98	99.99	24.42	0.12	24.12	0.01	24.01	0.02	23.70	0.02	23.54	0.01	23.11	0.02
SXDS0015	21.10	0.05	20.67	0.05	18.33	0.05	20.95	0.01	99.99	99.99	19.48	0.00	18.31	0.00	17.86	0.00
SXDS0016	25.34	99.99	24.98	99.99	23.52	0.07	22.01	0.01	21.01	0.01	20.87	0.01	20.87	0.01	20.82	0.01

Notes. Column (1) is the X-ray source name. Columns (2)–(9) show the measured total magnitude and associated error in from FUV to  $z'$ -band. 99.99 in the error column means the corresponding magnitude is an upper limit. 99.99 in the total magnitude means the object is not covered in that band. (This table is available in its entirety in a machine-readable form in the online journal. A portion is shown here for guidance regarding its form and content.)

**Table 9.** Multiwavelength properties of the X-ray AGN candidates II

	<i>J</i>		<i>H</i>		<i>K</i>		3.6 $\mu$ m		4.5 $\mu$ m		5.8 $\mu$ m		8.0 $\mu$ m		24 $\mu$ m	
	(mag)		(mag)		(mag)		(mag)		(mag)		(mag)		(mag)		(mag)	
(10)	(11)		(12)		(13)		(14)		(15)		(16)		(17)		(18)	
XDS0001	99.99	99.99	99.99	99.99	99.99	99.99	99.99	99.99	99.99	99.99	99.99	99.99	99.99	99.99	15.91	0.05
XDS0002	99.99	99.99	99.99	99.99	99.99	99.99	99.99	99.99	99.99	99.99	99.99	99.99	99.99	99.99	17.32	0.05
XDS0003	99.99	99.99	99.99	99.99	99.99	99.99	99.99	99.99	99.99	99.99	99.99	99.99	99.99	99.99	99.99	99.99
XDS0004	99.99	99.99	99.99	99.99	99.99	99.99	99.99	99.99	17.25	0.01	99.99	99.99	18.13	0.01	18.22	99.99
XDS0005	99.99	99.99	99.99	99.99	99.99	99.99	19.34	0.02	19.63	0.04	20.39	0.36	19.96	0.31	17.92	0.05
XDS0008	99.99	99.99	99.99	99.99	99.99	99.99	20.47	0.04	20.18	0.06	19.97	99.99	19.47	0.19	18.22	99.99
XDS0010	99.99	99.99	99.99	99.99	99.99	99.99	18.91	0.01	18.64	0.01	18.47	0.02	18.13	0.01	17.43	0.05
XDS0012	99.99	99.99	99.99	99.99	99.99	99.99	21.34	0.03	21.09	0.03	21.69	99.99	21.77	99.99	18.22	99.99
XDS0015	99.99	99.99	99.99	99.99	99.99	99.99	99.99	99.99	99.99	99.99	99.99	99.99	99.99	99.99	15.56	0.05
XDS0016	99.99	99.99	99.99	99.99	99.99	99.99	20.40	0.01	20.04	0.01	19.55	0.04	18.70	0.02	17.41	0.05

Notes. Column (10) is the X-ray source name. Columns (11)–(18) show measured total magnitude and associated error in from *J*- to  $\mu$ m-band. 99.99 in the error column means the corresponding magnitude is upper limit. 99.99 in the total magnitude column means the object is not covered in that band. (This table is available in its entirety in a machine-readable form in the online journal. A portion is shown here for guidance regarding its form and content.)

**Table 10.** Multiwavelength properties of the X-ray AGN candidates III

ID (19)	VLA ( $\mu$ Jy) (20)		<i>Si</i> (21)	Spec. <i>z</i> <i>z</i> <sub>spec</sub> flag (22)    (23)		Phot. <i>z</i> <i>z</i> <sub>phot</sub> type    flag (24)    (25)    (26)		
SXDS0001	0.0	0	0	0.505	NLA	0.480	GAL	0
SXDS0002	0.0	0	0	0.700	NLA	0.644	GAL	0
SXDS0003	0.0	0	0	9.999	NSP	0.622	GAL	0
SXDS0004	0.0	0	0	9.999	NSP	0.496	GAL	2
SXDS0005	0.0	0	0	1.050	NLA	0.782	GAL	0
SXDS0008	0.0	0	1	1.033	NLA	1.010	QSO	0
SXDS0010	0.0	0	1	1.224	BLA	0.800	QSO	0
SXDS0012	0.0	0	0	9.999	NSP	1.344	GAL	0
SXDS0015	0.0	0	0	0.098	NLA	0.598	GAL	2
SXDS0016	0.0	0	1	3.512	BLA	3.298	QSO	0

Notes. Column (19) is the X-ray name. Column (20) is 1.4 GHz flux measured with VLA observation from Simpson et al (2012); 0 in the first column means the object is outside of the VLA coverage. 1(0) in the second column indicates the object is (not) detected. Column (21) is stellarity index determined in the  $i'$ -band image; 1 means stellar object, and 0 means extended object. Columns (22) and (23) are the spectroscopic redshift and spectroscopic type; BLA and NLA represent broad-line and narrow-line AGNs, respectively. NID indicates the object is observed in the optical but can not be identified with the optical spectrum. NSP indicates the object is not observed in the optical. Columns (24) – (26) are photometric redshift, photometric type, and flag for photometric redshift. GAL (QSO) is the photometric type showing whether the SED of the object is fitted better with the galaxy (QSO) templates. (This table is available in its entirety in a machine-readable form in the online journal. A portion is shown here for guidance regarding its form and content.)

We warmly thank the staff members of the Subaru telescope for their support during the observations. We would like to thank the anonymous referee for valuable comments that improved this paper. MA is supported by JSPS Grant-in-Aid for Young Scientist (B) (18740118), and MA and HH are supported by Grant-in-Aid for Scientific Research (B) (21340042). HH thanks the Grant-in-Aids for Challenging Exploratory Research (24650145) from JSPS, which partially supported this research.

This publication makes use of data products from the Two Micron All Sky Survey, which is a joint project of the University of Massachusetts and the Infrared Processing and Analysis Center/California Institute of Technology, funded by the National Aeronautics and Space Administration and the National Science Foundation.

Based on observations obtained with MegaPrime/MegaCam, a joint project of CFHT and CEA/IRFU, at the Canada-France-Hawaii Telescope (CFHT) which is operated by the National Research Council (NRC) of Canada, the Institut National des Sciences de l'Univers of the Centre National de la Recherche Scientifique (CNRS) of France, and the University of Hawaii. This work is based in part on data products produced at Terapix available at the Canadian Astronomy Data Centre as part of the Canada-France-Hawaii Telescope Legacy Survey, a collaborative project of NRC and CNRS.

## References

- Aird, J., Nandra, K., Georgakakis, A., Laird, E.S., Steidel, C.C., Sharon, C. 2008, *MNRAS*, 387, 883
- Aird, J., et al. 2010, *MNRAS*, 401, 2531
- Akiyama, M. 2005, *ApJ*, 629, 72
- Alexander, D.M., et al. 2011, *ApJ*, 738, 44
- Alonso-Herrero, A., Pérez-González, P.G., Rieke, G.H., Alexander, D.M., Rigby, J.R., Papovich, C., Donley, J.L., & Rigopoulou, D. 2008, *ApJ*, 677, 127
- Barger, A.J., Cowie, L.L., Mushotzky, R.F., Yang, Y., Wang, W.-H., Steffen, A.T., Capak, P. 2005, *AJ*, 129, 578
- Bennert, V.N., Auger, M.W., Treu, T., Woo, J.-H., & Malkan, M.A. 2011, *ApJ*, 742, 107
- Bertin, E. & Arnouts, S. 1996, *A&AS*, 117, 393
- Bolzonella, M., Miralles, J.-M., & Pello, R., 2000, *A&A*, 363, 476
- Bongiorno, A., et al. 2014, *MNRAS*, 443, 2077
- Bradshaw, E.J., Almaini, O., Hartley, W.G., et al. 2013, *MNRAS*, 433, 194
- Brammer, G.B., van Dokkum, P.G., & Coppi, P. 2008, *ApJ*, 686, 1503
- Brusa, M., et al. 2009, *A&A*, 507, 1277
- Brusa, M., et al. 2010, *ApJ*, 716, 348
- Bruzual, A.G., & Charlot, S., 1993, *ApJ*, 405, 538
- Calzetti, D., Armus, L., Bohlin, R.C., Kinney, A.L., Koornneef, J., Storchi-Bergmann, T. 2000, *ApJ*, 533, 682
- Cappelluti, N., et al. 2009, *A&A*, 497, 635
- Cardamone, C.N., Urry, C.M., Damen, M., van Dokkum, P., Treister, E., Labbe, I., Virani, S., Lira, P., & Gawiser, E. 2008, *ApJ*, 680, 130
- Cardamone, C.N., et al. 2010, *ApJS*, 189, 270
- Chabrier, G. 2002, *ApJ*, 567, 304
- Chiappetti, L., et al. 2005, *A&A*, in press, astro-ph/0505117
- Civano, F., et al. 2012, *ApJS*, 201:30(21pp)
- Cowie, L.L., Garmire, G.P., Bautz, M.W., Barger, A.J., Brandt, W.N., Hornschemeier, A.E. 2002, *ApJL*, 566, 5
- Daddi, E., et al. 2007, *ApJ*, 670, 173
- de Ruiter, H.R., Arp, H.C., Willis, A.G. 1977, *A&AS*, 28, 211
- Decarli, R., Falomo, R., Treves, A., Labita, A., Kotilainen, J.K., & Scarpa, R. 2010, *MNRAS*, 402, 2453
- Diaz Tello, J., et al. 2013, *ApJ*, 771:7
- Donley, J.L., Rieke, G.H., Rigby, J.R., & Pérez-González, P.G. 2005, *ApJ*, 634, 169
- Donley, J.L., et al. 2012, *ApJ*, 748, 142
- Ebrero, J., Carrera, F.J., Page, M.J., Silverman, J.D., Barcons, X., Ceballos, M.T., Corral, A., Della Cecca, R., Watson, M.G. 2009, *A&A*, 493, 55
- Elbaz, D., et al. 2011, *A&A*, 533, 119
- Elvis, M., et al. 2009, *ApJ*, 184, 158
- Elvis, M., et al. 2012, *ApJ*, 759:6(20pp)
- Feruglio, C., et al. 2008, *A&A*, 488, 417
- Finoguenov, A., et al. 2010, *MNRAS*, 403, 2063
- Fioc, M., & Rocca-Volmerange, B. 1997, *A&A*, 326, 950
- Fiore, F., et al. 2003, *A&A*, 409, 79
- Fiore, F., et al. 2008, *ApJ*, 672, 94
- Furusawa, H. et al. 2008, *ApJS*, 176, 1
- Georgakakis, A., Rowan-Robinson, M., Nandra, K., Digby-North, J., Pérez-González, P.G., & Barro, G. 2010, *MNRAS*, 406, 420
- Gunn, J.E., Stryker, L.L. 1983, *ApJS*, 52, 121
- Hanami, H., et al. 2012, *PASJ*, 64, 70
- Hao, L., et al. 2005, *AJ*, 129, 1783
- Hao, H., et al. 2014, *MNRAS*, 438, 1288
- Häring, N., & Rix, H.-W. 2004, *ApJ*, 604, L89
- Hasinger, G., Miyaji, T., Schmidt, M., *A&A*
- Hiroi, K., Ueda, Y., Akiyama, M., Watson, M.G. 2012, *ApJ*, 758, 49
- Iverson, R., et al. 2004, *ApJS*, 154, 124
- Iwamuro, F., Moritani, Y., Yabe, K., et al., 2012, *PASJ*, 64, 59
- Jahnke, K., Bongiorno, A., Brusa, M., et al. 2009, *ApJL*, 706, 215
- Kim, D.W., et al. 2004, *ApJ*, 600, 59
- Kimura, M., Maihara, T., Iwamuro, F., et al., 2010, *PASJ*, 62, 1135
- Kiuchi, G., Ohta, K., Akiyama, M. 2009, *ApJ*, 696, 1051
- Koekemoer, A.M., et al. 2004, *ApJL*, 600, 123
- Kormendy, J., & Richstone, D. 1995, *ARA&A*, 33, 581
- Lacy, M., et al. 2004, *ApJS*, 154, 166
- Lacy, M., et al. 2005, *ApJS*, 161, 41
- La Franca, F., et al. 2005, *ApJ*, 635, 864
- Laird, E.S., et al. 2009, *ApJS*, 180, 102
- Lawrence, A., et al. 2007, *MNRAS*, 379, 1599
- Leipski, C., et al. 2005, *A&A*, 440, L5
- Loaring, N.S., et al. 2005, astro-ph/0507408
- Lonsdale, C. J., et al. 2003, *PASP*, 115, 897
- Lonsdale, C.J., et al. 2004, *ApJS*, 154, 54
- Luo, B., et al. 2010, *ApJS*, 187, 560
- Lusso, E., Hennawi, J.F., Comastri, A., Zamorani, G., Richards, G.T., Vignali, C., Treister, E., Schawinski, K., Salvato, M., & Gilli, R. 2013, *ApJ*, 777:86(28pp)
- Magdziarz, P., & Zdziarski, A. A. 1995, *MNRAS*, 273, 837
- Mainieri, V., et al. 2011, *A&A*, 535, A80
- Marconi, A., & Hunt, L.K. 2003, *ApJ*, 589, L21



**Table 11.** X-ray properties of AGN candidates

ID	$z$	HR2	$\log N_{\mathrm{H}}$ ( $\mathrm{erg\ s^{-1}}$ )	Photon Index	$\log L_{2-10\mathrm{keV}}$ ( $\mathrm{cm^{-2}}$ )
(1)	(2)	(3)	(4)	(5)	(6)
SXDS0001	0.505	-0.42	21.9	1.9	43.2
SXDS0002	0.700	-0.64	20.8	1.9	43.5
SXDS0003	0.622	-0.34	22.1	1.9	43.6
SXDS0004	0.496	-1.00	—	1.9	42.7
SXDS0005	1.050	-0.24	22.5	1.9	44.1
SXDS0008	1.033	-0.62	21.3	1.9	43.7
SXDS0010	1.221	-0.72	—	2.1	44.1
SXDS0012	1.344	-0.36	22.5	1.9	44.0
SXDS0015	0.098	-0.62	20.8	1.9	42.3
SXDS0016	3.512	-0.60	21.9	1.9	44.5

Notes. Column (1) is the X-ray name. Columns (2) and (3) are redshift and HR2 used to calculate the best-estimated X-ray properties. HR2 of -1.00 (1.00) means the source is only detected in the soft-(hard-)band. Column (4) is  $\log N_{\mathrm{H}}$ , column (5) is  $\Gamma$ , and column (6) is  $\log L_{2-10\mathrm{keV}}$ . — in the column (4) means  $\log N_{\mathrm{H}}$  is not given because HR2 is smaller than expected for a power-law of  $\Gamma = 1.9$ .  $\Gamma$  of 1.9 means the value is fixed. Details of determination of the X-ray properties are described in Section 7.1. (This table is available in its entirety in a machine-readable form in the online journal. A portion is shown here for guidance regarding its form and content.)

- Marconi, A., Risaliti, G., Gilli, R., Hunt, L.K., Maiolino, R., & Salvati, M. 2004, MNRAS, 351, 169
- Mateos, S., et al. 2012, MNRAS, 426, 3271
- McLure, R.J., Jarvis, M.J., Targett, T.A., Dunlop, J.S., Best, P.M. 2006, MNRAS, 368, 1395
- McLure, R.J., Pearce, H.J., Dunlop, J.S., et al. 2013, MNRAS, 428, 1088
- Merloni, A., et al. 2010, ApJ, 708, 137
- Mignoli, M., et al. 2004, A&A, 418, 827
- Miller, G.E., & Scalo, J.M. 1979, ApJS, 41, 513
- Morokuma, T., et al. 2008, ApJ, 676, 121
- Morokuma, T., et al. 2008, ApJ, 676, 163
- Morrissey, P., Conrow, T., Barlow, T.A., et al. 2007, ApJS, 173, 682
- Murray, S.S., et al. 2005, astro-ph/0504084
- Nandra, K., Georgakakis, A., Willmer, C.N.A., Cooper, M.C., Croton, D.J., Davis, M., Faber, S.M., Koo, D.C., Laird, E.S., & Newman, J.A. 2007, ApJ, 660, L11
- Nobuta, K., et al. 2012, ApJ, 761, 143
- Oke, J.B. 1974, ApJS, 27, 210
- Ouchi, M., Shimasaku, K., Akiyama, M., et al. 2005, ApJ, 620, 1
- Ouchi, M., Shimasaku, K., Akiyama, M., et al. 2008, ApJS, 176, 301
- Ouchi, M., et al. 2009, ApJ, 696, 1164
- Pannella, M., et al. 2014, ApJ, in press, arXiv:1497.5972
- Peng, C.Y., Impey, C.D., Rix, H.-W., Kochanek, C.S., Keeton, C.R., Falco, E.E., Lehár, J., McLeod, B.A. 2006, ApJ, 649, 616
- Richards, G.T., et al. 2003, AJ, 126, 1131
- Rosario, D.J., et al. 2013, ApJ, 763, 59
- Sani, E., Marconi, A., Hunt, L.K., & Risaliti, G. 2011, MNRAS, 413, 1479
- Saito, T., Shimasaku, K., Okamura, S., Ouchi, M., Akiyama, M., Yoshida, M., Ueda, Y. 2008, ApJ, 675, 1076
- Salpeter, E. 1955, ApJ, 121, 161
- Salvato, M., et al. 2009, ApJ, 690, 1250
- Schramm, M., & Silverman, J.D. 2013, ApJ, 767, 13
- Schulze, A., & Wisotzki, L. 2014, MNRAS, 438, 3422
- Sekiguchi, K., et al. 2005, Multiwavelength mapping of galaxy formation and evolution, p.82
- Silverman, J.D., et al. 2008, ApJ, 679, 118
- Silverman, J.D., et al. 2009, ApJ, 696, 396
- Simpson, C., Martinez-Sansigre, A., Rawlings, S., Ivison, R., Akiyama, M., Sekiguchi, K., Takata, T., Ueda, Y., Watson, M. 2006, MNRAS, 372, 741
- Simpson, C., Rawlings, S., Ivison, R., et al. 2012, MNRAS, 421, 3060
- Skrutskie, M.F., Cutri, R.M., Stiening, R., et al. 2006, AJ, 131, 1163
- Smail, I., Sharp, R., Swinbank, A.M., Akiyama, M., Ueda, Y., Foucaud, S., Almaini, O., Croom, S. 2008, MNRAS, 389, 407
- Stern, J., & Laor, A. 2012, MNRAS, 423, 600
- Stern, D., et al. 2005, ApJ, 631, 163
- Surace, J.A., et al. 2005, "The SWIRE Data Release 2: Image Atlases and Source Catalogs for ELAIS-N1, ELAIS-N2, XMM-LSS, and the Lockman Hole"
- Sutherland, W., & Saunders, W. 1992, MNRAS, 259, 413
- Takagi, T., et al. 2010, A&A, 514, 5
- Ueda, Y., Akiyama, M., Ohta, K., Miyaji, T. 2003, ApJ, 598, 886
- Ueda, Y., Watson, M.G., Stewart, I.M., Akiyama, M., & Schwobe, A.D. 2008, ApJS, 179, 124
- Ueda, Y., Akiyama, M., Hasinger, G., Miyaji, T., Watson, M.G. 2014, ApJ, 786, 104
- Watson, M., Roberts, T.P., Akiyama, M., Ueda, Y. 2005, A&A, 437, 899
- Wolstencroft, R.D., Savage, A., Clowes, R.G., MacGillivray, H.T., Leggett, S.K., Kalafi, M. 1986, MNRAS, 223, 279
- Xue, Y.Q., Brandt, W.N., Luo, B., Rafferty, D.A., Alexander, D.M., Bauer, F.E., Lehmer, B.D., Schneider, D.P., & Silverman, J.D. 2010, ApJ, 720, 368
- Yamada, T., et al. 2005, ApJ, 634, 861
- Yamada, T., et al. 2009, ApJ, 699, 1354
- Yang, Y., Mushotzky, R.F., Steffen, A.T., Barger, A.J., Cowie, L.L. 2004, AJ, 128, 1501
- Yan, H., Windhorst, R.A., Rottgering, H.J.A., Cohen, S.H., Odewahn, S.C., Chapman, S.C., & Keel, W.C., 2003, ApJ,

585, 67  
Yencho, B., Barger, A.J., Trouille, L., Winter, L.M. 2009, ApJ, 698, 380  
Yoshida, M., Shimasaku, K., Ouchi, M., Sekiguchi, K., Furusawa, H., Okamura, S. 2008, ApJ, 679, 269  
Zheng, W., et al. 2004, ApJS, 155, 73